JOINT EUROPEAN TORUS JET

JET–P(95)72

Many Authors

JET Posters Presented to 37th Annual Meeting, APS Division of Plasma Physics. (Louisville, USA, 6th-10th November 1995)

JET-P(95)72

JET Posters presented to the 37th Annual Meeting, APS Division of Plasma Physics (Louisville, USA, 6–10 November 1995)

Many Authors

JET Joint Undertaking, Abingdon, Oxfordshire, OX14 3EA, UK.

December 1995

JET Posters presented to the 37th Annual Meeting,
APS Division of Plasma Physics
(Louisville, USA, 6–10 November 1995)

Contents

The ρ_* Scaling Experiments for ELMy H-modes in JET

J P Christiansen, J G Cordey, B Balet, D Campbell, C D Challis, J Ehrenberg, R Gianella, C Gormezano, C Gowers, J de Haas, P Harbour, C Lowry, P Nielsen, L Porte, E Righi, G R Saibene, D F H Start, M Stamp, P M Stubberfield, K Thomsen, M von Hellermann.
JET Joint Undertaking, Abingdon, Oxfordshire, OX14 3EA, UK.

In Collaboration with T Luce, C Petty and J DeBoo of G.A.

- The similarity approach. Dimensionless parameters.
- ELMy H-modes from JET scans of ρ^*.
- Global similarity of scaled discharges.
- Local Transport analysis by TRANSP.
- Power scaling of confinement and L$\rightarrow$ H mode threshold.
- Implications for next step: Operation close to or far from threshold.
- Summary.

SIMILARITY APPROACH IN CONFINEMENT SCALING

- General form of thermal diffusivity (Kadomtsev, Connor and Taylor)

$$\chi = \chi_{BOHM}\, F\,(\rho_*,\ \nu_*,\ \beta,\ q,\ \varepsilon,\ \kappa\ .....)$$

- Dimensionally similar discharges (TFTR, DIIID, JET) vary F by varying only one argument.

  Example: a variation of ρ_* at const. ν_*, β, q, ε, κ can determine

$$x_\rho = \frac{\partial \log F}{\partial \log \rho_*} = -1 \text{ (MHD-stochastic), } 0 \text{ (Bohm), } +1 \text{ (gyroBohm).}$$

- **PROBLEM:** on a single machine varying B by a factor 2 varies ρ_* by a factor 1.6 and the difference between T_e predicted by Bohm and gyroBohm then varies by only a factor 1.2!

- **SOLUTION:** Multi-machine experiments required. Select parameter values for ν_*, β, q which permit sensible extrapolation in ρ_* for next step (ITER).

- **HISTORY:** L-mode ρ_* scaling experiments on TFTR, DIIID and JET (1991-92) show $x_\rho=0$ in agreement with ITER89P. (DIIID show gyro Bohm scaling for electron channel).

- **STUDY:** ρ_* scaling experiments on JET and DIIID.

- **QUESTION:** Will these experiments show $x_\rho \approx 1$ (gyro Bohm) as predicted by ITER93H.

ELMY H-MODE SCALING EXPERIMENTS ON JET
PULSE GEOMETRY AND PARAMETERS

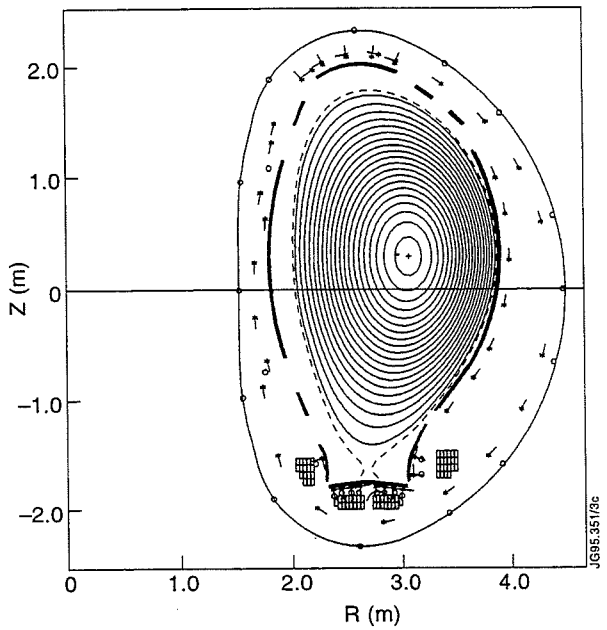

	SET 1		SET 2	
	#33131	#33140	#35156	#35171
I_ϕ (MA)	2.8	1.6	2	1
B_α (T)	3	1.7	2	1
P_{NBI} (MW)	19.6	6.3	9.2	4.8
$\rho*$	$1.8\ 10^{-4}$	$2.8\ 10^{-4}$	2.10^{-4}	$3.3\ 10^{-4}$
$\nu*$	10^{-2}	10^{-2}	$3\ 10^{-2}$	$3\ 10^{-2}$
β_{Ith}	0.6	0.6	0.7	0.7
q_{95}	3.7	3.7	3.4	3.4
κ	1.8	1.8	1.7	1.7
δ	0.25	0.25	0.2	0.2
τ_{th}	0.37	0.36	0.35	0.17

PULSE CHARACTERISTICS

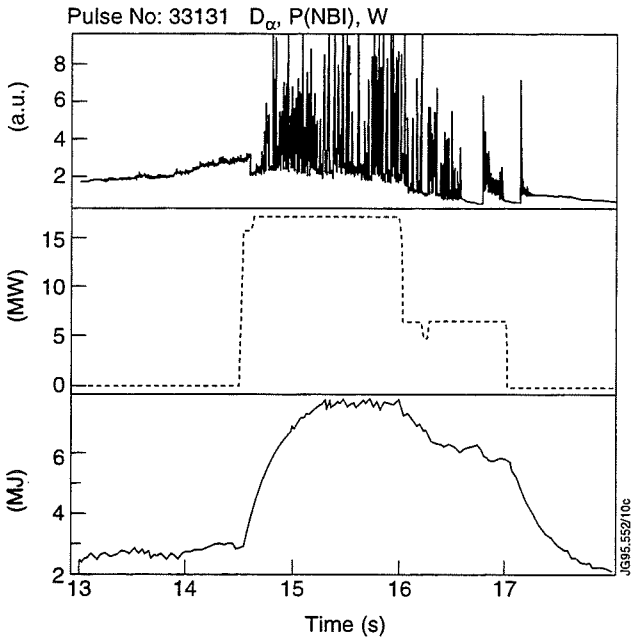

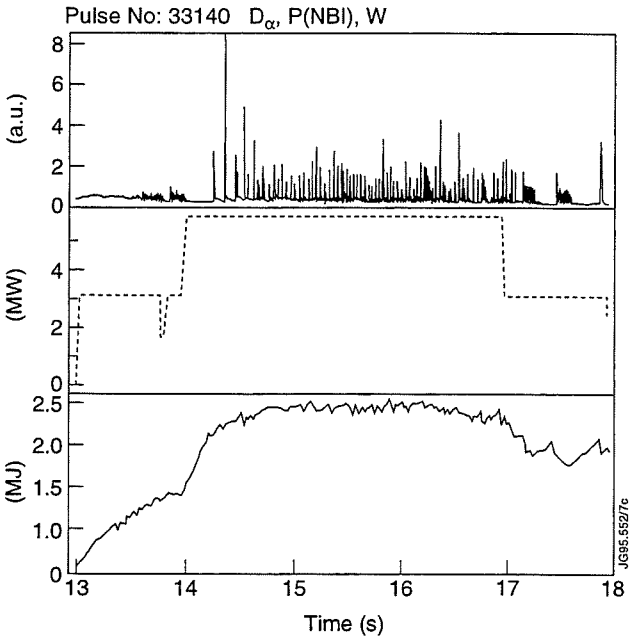

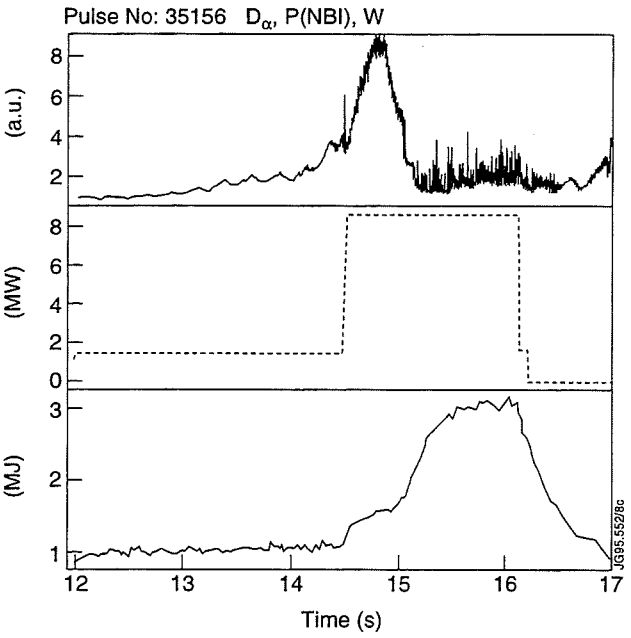

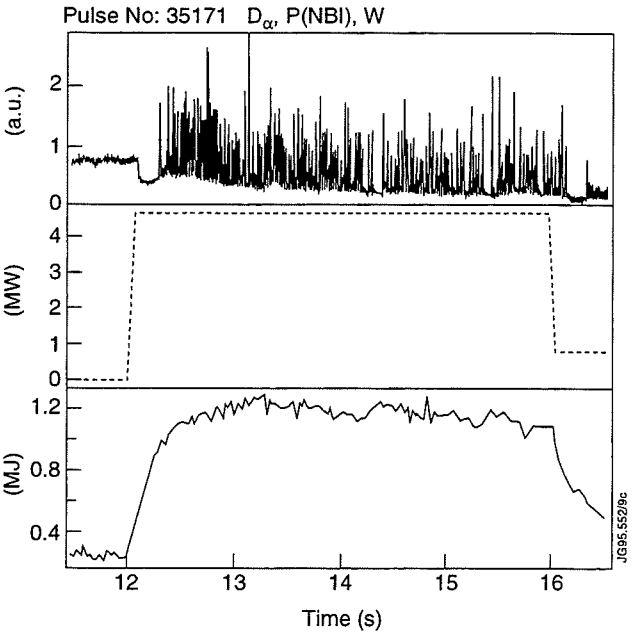

GLOBAL CONFINEMENT

- Scaling of thermal confinement time τ_{Eth} with ρ_*:

  Gyro Bohm $\tau_{Eth} \sim B$

  Bohm $\tau_{Eth} \sim B^{1/3}$

  Stochastic (MHD) $\tau_{Eth} \sim B^{-1/3}$

- First set exhibit $\tau_{Eth} \sim B^0$, worse than Bohm, i.e. Goldston scaling.

- Second set shows gyro Bohm $\tau_{Eth} \sim B$ scaling.

$\therefore$ Difference in scaling between these two sets of pulses is due to differences in ELM amplitude - frequency. For pulse #33131 the ELMs are of "compound type", i.e. following each ELM the plasma returns to L-mode state for some period.

$\therefore$ Proximity to the L→H power threshold is different for each pulse.

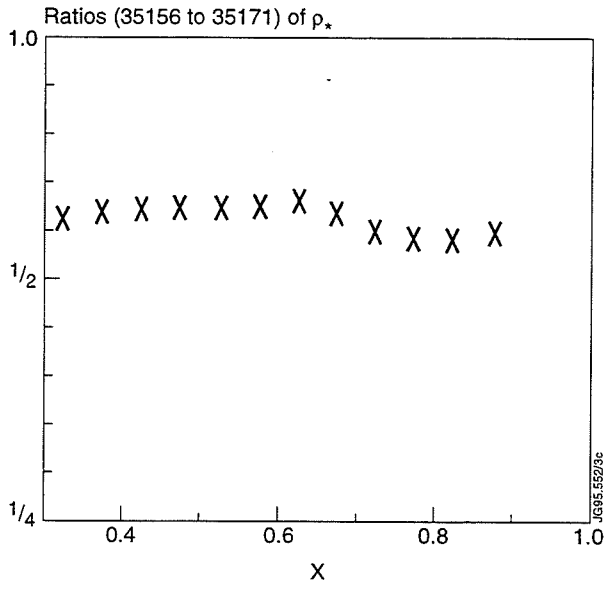

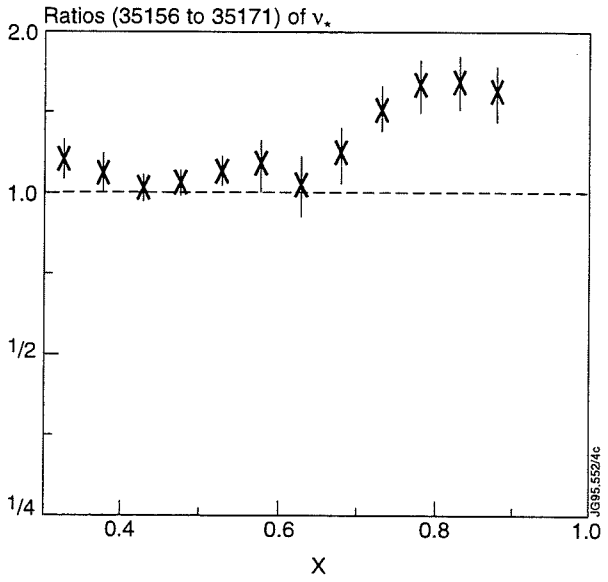

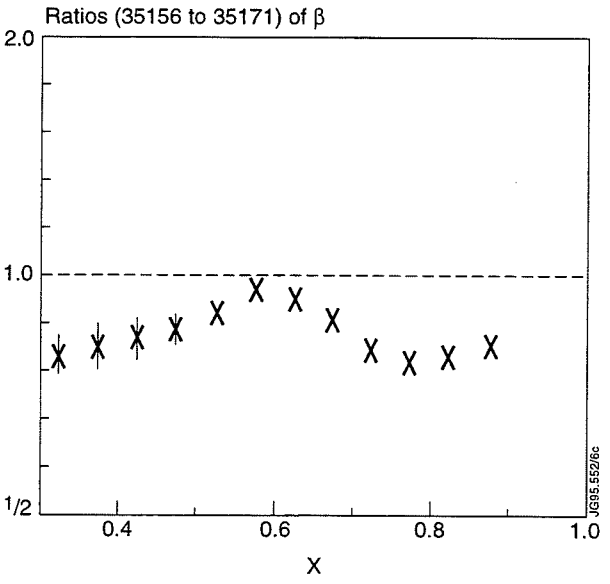

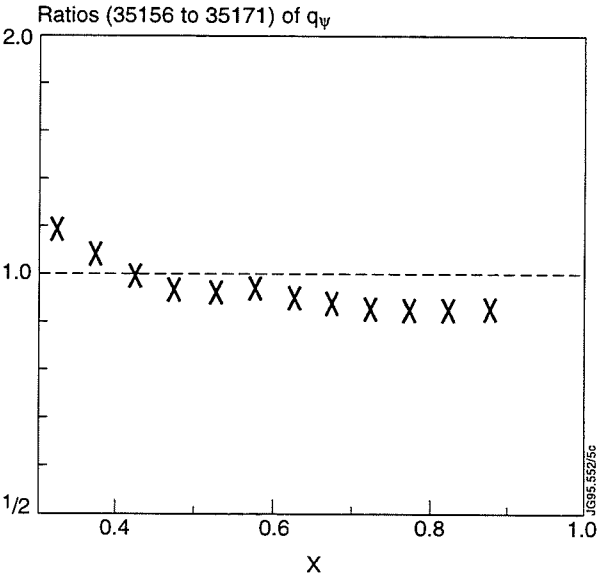

Dimensionless parameters are reasonably matched for the 2nd set of pulses (ratio → 1).

Data points denote average values during ELMing phase and vertical bars show 1 st.d. from average.

SCALING OF LOCAL HEAT FLUX

- The output from TRANSP has been smoothed (running average over 10 points) to suppress fluctuations and sawteeth.

- Normalise heat fluxes to the "Bohm heat flux"

$$q_B = \chi_B \, en_e \, \nabla T_e \quad , \chi_B = T_e/B$$

- Replace ∇T_e by T_e/a to eliminate "spatial features" in LIDAR T_e measuring system.

- Examine ratio $$\frac{(q/q_B)_{\#35156}}{(q/q_B)_{\#35171}} = \frac{F_{\#35156}}{F_{\#35171}}$$

"HYBRID' ρ_* SCALING OF HEAT FLUX

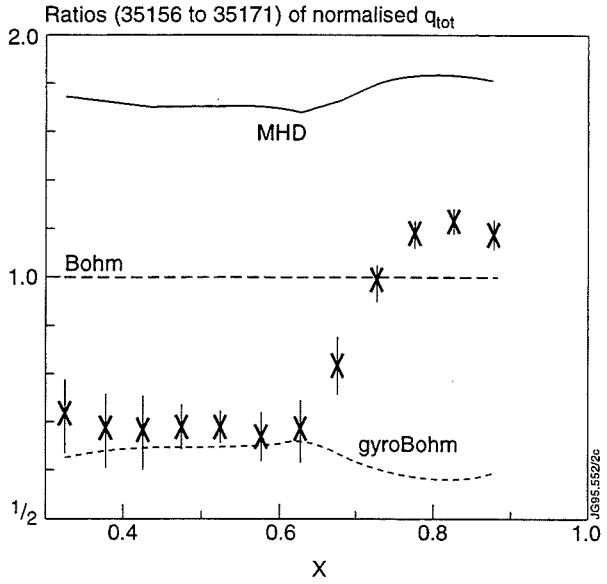

∴ The total heat flux, qe and qi exhibit gyro Bohm scaling in the central plasma, Bohm scaling in the outer part. At the edge x = 1 gyro Bohm scaling must be restored as $q(x = 1) = P_{tot}$/surface.

∴ The result, the shape of the graph, whether ELM's cause this is not yet understood.

POWER SCALING OF CONFINEMENT AND L→H THRESHOLD

- Confinement scaling laws such as ITER89P and ITER93H and the power threshold scaling laws established by the ITER data base group can be expressed in terms of the dimensionless parameters ρ_*, ν_*, β etc. and one dimensional parameter.

- For all cases we express the "normalised" power to reach a given ρ_*, ν_*, β etc.

ITER89P:	$P_a^{3/4}$	$= C_{89}$	$\rho_*^{-5/2}\ \nu_*^{-1/2}\ \beta^{9/4}$	f_{89}
ITER93H:	$P_a^{3/4}$	$= C_{93}$	$\rho_*^{-3/2}\ \nu_*^{-1/2}\ \beta^{3}$	f_{93}
THRESHOLD 1:	$P_a^{3/4}$	$= C_{TH1}$	$\rho_*^{-3}\ \nu_*^{-1/4}\ \beta$	f_{TH1}
THRESHOLD 2:	$P_a^{3/4}$	$= C_{TH2}$	$\rho_*^{-7/2}\ \nu_*^{-1/4}\ \beta^{5/4}$	f_{TH1}

- The C's are constants and f_{89} etc. denote residual functions of parameters like ε, κ, q, etc.

NOTE

1. Threshold power has much stronger ρ_* dependence than "confinement power".

2. "Confinement", especially ITER93H shows much stronger dependence on β than threshold power.

3. Power depends weakly on collisionality.

THE ITER H-MODE DATA BASE

- Select ELMy data from the 1995 version of the ITER H-mode data base.
- Study β vs ρ_* values: actual data and predictions.
- Predictions from e.g. ITER93H

$$\beta_{ITER93H} = (P_a^{3/4}/C_{93}\ \nu_*^{-1/2}\ f_{93})^{1/3}\ \rho_*^{1/2}$$

$$\beta_{THR1} = (P_a^{3/4}/C_{TH1}\ \nu_*^{-1/4}\ f_{TH1})\rho_*^{3}$$

$\therefore$ Thus β at the threshold strongly depends on ρ_*

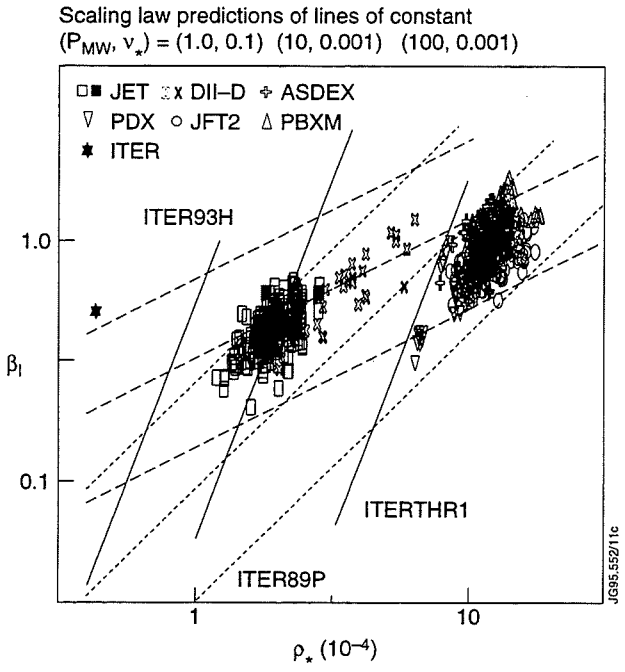

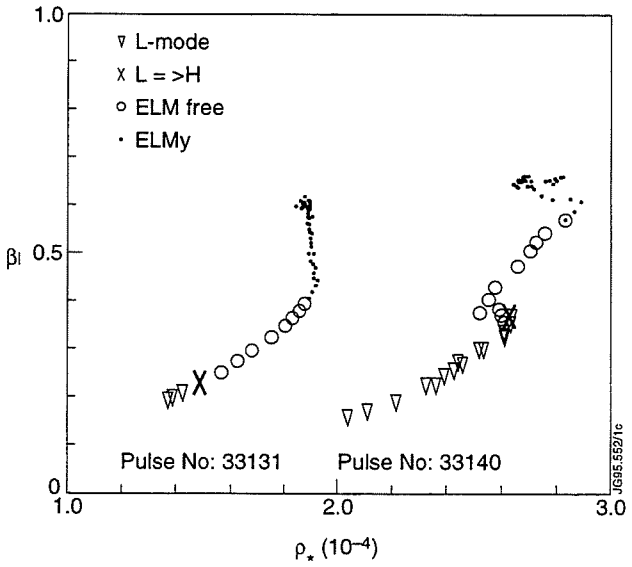

INFLUENCE OF POWER THRESHOLD ON ELMY H-MODE CONFINEMENT

- The different dependencies on ρ_* of confinement and power threshold have implications for the chosen operating regime of e.g. ITER.

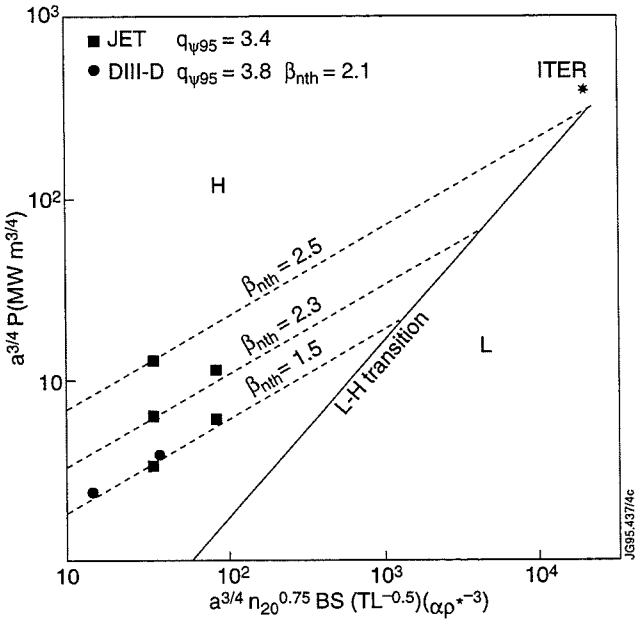

Normalised power vs ρ_*^{-3}

[DIIID data from Petty, Luce et al, Physics of Plasmas, 2 (1995) 2342]

- If $P >> P_{THR1}$ (or P_{THR2}) JET and DIIID results show appr. gyro Bohm scaling of ELMy H-mode confinement with ρ_*.

- When $P \geq P_{THR}$ this scaling is lost.

- Therefore the proximity of P (ITER EDA) to $P_{THRESHOLD}$ is a critical issue.

SUMMARY

- A Similarity approach has been used in JET experiments which aim at establishing the confinement scaling with ρ_* in steady ELMy H-mode plasmas.

- Global and local analysis have demonstrated that two sets of experiments show different confinement scalings.

- At power levels well above the threshold gyro Bohm scaling applies (as predicted by ITER93H).

- Close to threshold the scaling worsens with ρ_* and may become Bohm-Goldston like. The effects from ELMs in this case have not been fully assessed.

- Scalings of "confinement" power and threshold power show different variations with ρ_* and β.

- The threshold scaling law for the transition from L-mode to ELMy H-mode needs to be firmly established to ensure that the chosen power level for ITER is well above any predicted threshold.

Alfvén Eigenmode Studies in JET

A Fasoli[1], J B Lister[1], S Sharapov, S Ali-Arshad, G Bosia, D Borba, D J Campbell, N Deliyanakis, J A Dobbing, C Gormezano, H Holties[2], G Huysmans, J Jacquinot, A Jaun[1], W Kerner, P Lavanchy[1], J-M Moret[1], L Porte, A Santagiustina, L Villard[1]

JET Joint Undertaking, Abingdon, Oxfordshire, OX14 3EA, UK.

[1] CRPP-EPFL, Ass. Euratom-Suisse Confederation, 21 av. des Bains, CH-1007 Lausanne.

[2] FOM Institute for Plasma Physics, Rijnhuizen, Nieuwegein, The Netherlands.

1. ABSTRACT

Multiple weakly damped Alfven Eigenmodes (AE) have been excited and detected by means of a dedicated active diagnostic in JET plasmas heated by ICRH, NBI, lower hybrid heating and high current ohmic heating. An interpretation of this phenomena is found in terms of a new class of AE, the Kinetic AE, predicted in theory which include finite Larmor radius and toroidicity effects. Numerical tools have been developed to model spectra of the KTAE-modes in the shaped tokamak plasmas. The resonant excitation of AE by ICRH beat waves has been also attempted experimentally on JET plasmas. AE of relatively large amplitude are excited when the difference frequency between ICRH antennas is of the order of $V_A/(2qR)$.

2. INTRODUCTION AND MOTIVATION

- Weakly damped AE are important for confinement of alpha-particles created by fusion
- reactions in D-T magnetically confined plasmas.
- Resonant wave-particle processes between AE and fast ions can both drive the modes unstable and produce modifications to the particle orbits.
- Above a certain threshold amplitude, AE can induce stochasticity of the particle orbits and consequently anomalous radial particle transport. By coupling to the magnetic ripple effects, wall damage can be also caused.
- In ignited plasmas, large amounts of energy and steep pressure gradients characterise the slowing down alphas, a significant fraction of which will be resonant, with $V \sim V_A$.
- The damping, the frequency spectra and the spatial distributions of AE are investigated by means of a new active diagnostic system.
- Goal: to assess the AE stability and to predict the effects of AE on particle orbits for cases in which the modes cannot be stabilised.

3. EXPERIMENTAL METHOD: EXTERNAL EXCITATION + SYNCHRONOUS DETECTION

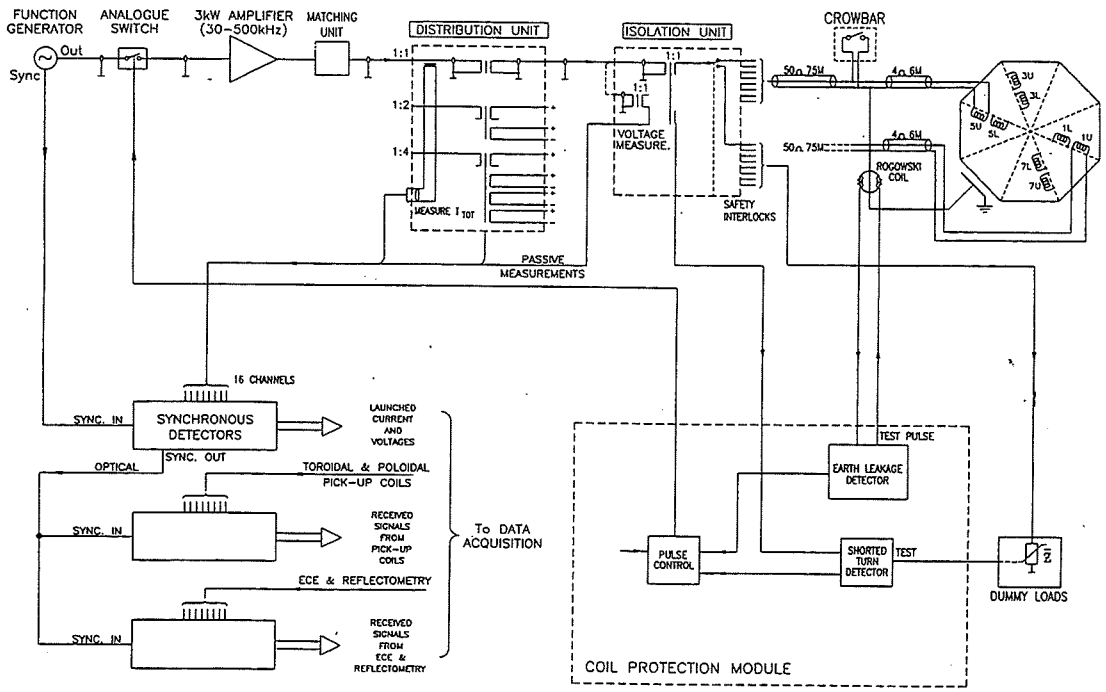

Fig.1: The saddle coil system at JET: AE exciter and detector experimental lay out $f_{exciter}$ *= 30 - 500 kHz.* $I_{saddle\ coil}$*<30 A;* $V_{saddle\ coil}$ *< 500 V (*$\rightarrow \delta B/B_{core}<10^{-5}$ *)*

Synchronous detection: **-driven response** (Re, Im)

-band width in 20-500 kHz; band width out=500 Hz;

sampling rate. =1 kHz.

Diagnostic channels: -active **saddle coils V, I** (antenna impedance).

-passive saddle coils and fast magnetic coils: $\delta \mathbf{B_{pol}}$, $\delta \mathbf{B_r}$ **(**$\rightarrow$ **n, m)**

-Heterodyne ECE + microwave reflectometry $\rightarrow$ δ**B(r)** , δ**n(r)**

Data analysis: diagnostic signal/driving current $\rightarrow$ transfer function H.

AE = resonance in H, with complex poles, p_k , and residues, r_k

$$H(\omega,x)=\sum_{k=1}^{N}\frac{1}{2}\left(\frac{r_k(x)}{i\omega-p_k}+\frac{r_k^{*}(x)}{i\omega-p_k^{*}}\right)+D(\omega,x)=\frac{B(\omega,x)}{A(i\omega)}$$

N = n. of resonances in the meas. range, $\omega=2\pi f_{exciter}$, x = meas. position. $p_k=i\omega_{0k}+\gamma_k$:common pole.

D accounts for direct coupling with the antenna.

Fit of data with H, with a single denominator A and separate numerators B.

Im(p) $\rightarrow$ $\mathbf{f_{obs}=\omega_{0k}/2p}$**. Real(p) (stable modes)** $\rightarrow$ $\gamma=\gamma_{damping}-\gamma_{drive}$ **Residues** $\rightarrow$ **Eigenfunction**

4.TAE/EAE EXCITATION AND DETECTION

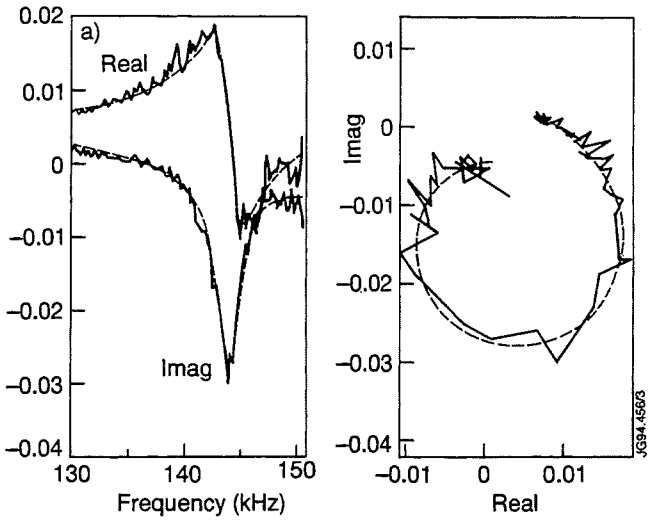

Fig. 2 TAE resonance. Real and imag. (left) and complex plane representation (right) of a magnetic probe signal, normalised to the current driven in the antenna.

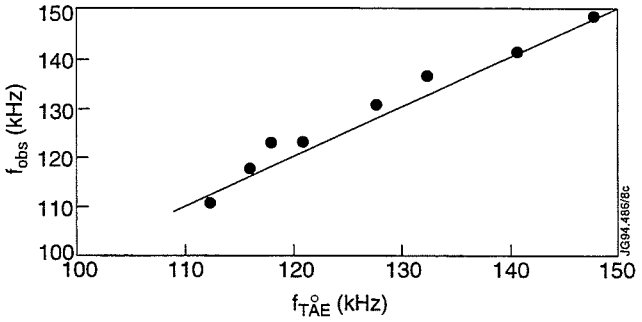

Fig. 3 AE frequency vs. B_{tor} (#31591). B_{tor} varied linearly with t from 2.2 to 3 T; density, I_p~const.. $f^0_{TAE} \cong v_A/(4\pi qR_0)$ (q=1.5)

$\delta B_{pol,edge}/B_{tor}<10^{-7}$ for $I_{saddle\ coil}<10$ A. With numerator/denom. of order 5/2, the fit gives f_{obs}=144.2+-0.1 kHz, $\gamma/2\pi$=1400+-100 s^{-1} → Q = ω/γ ~ 125, γ/ω ~ 0.8%.

Ohmic phase of JET shot #31638. $B_{tor} \cong 2.8$ T, $I_p \cong 2.2$ MA, $\bar{n}_e \cong 3x10^{19}$ m^{-3}; upper saddle coils, in phase and 180^0 apart.

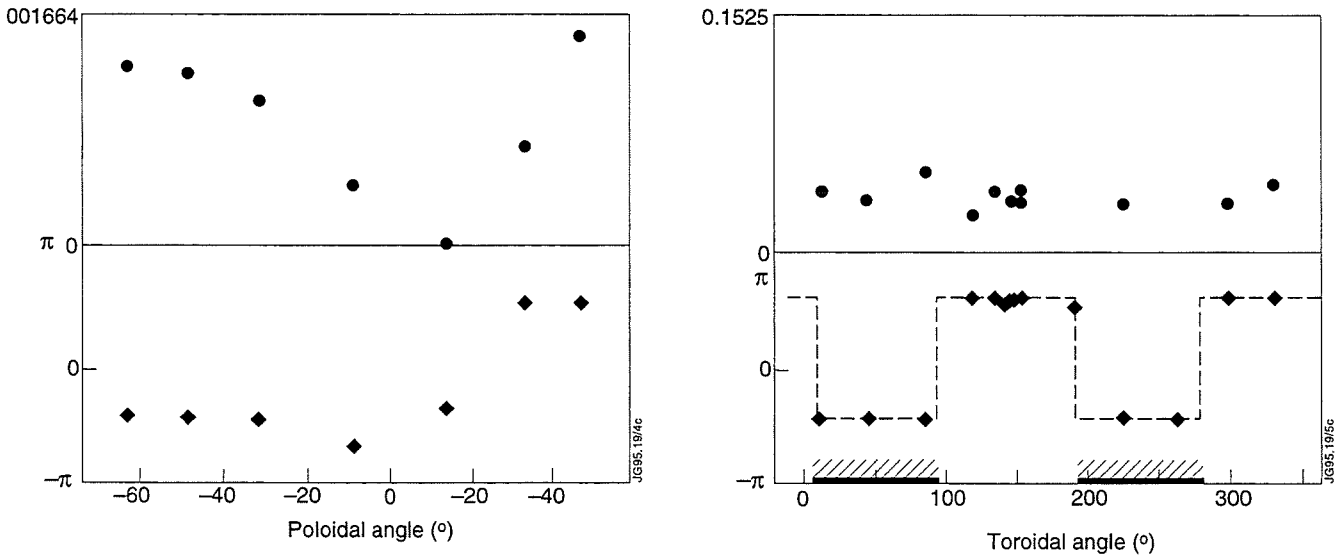

Fig. 4 TAE toroidal and poloidal structure: magn. (+), phase (x) of AE residues, In|=2.

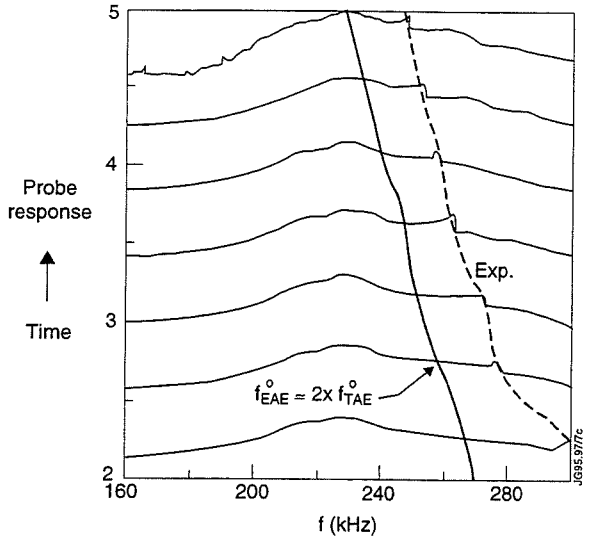

Fig. 5 Global modes with spatial distributions and damping rates similar to the TAE case were driven and detected for $f>f_{TAE}$. As in the example shown here, the mode frequencies followed $2f^{0}_{TAE}$. These modes were thereby identified as Ellipticity Induced AE (EAE).
$n_e \cong 4\text{-}8\ x10^{19}\ m^{-3}$; $B_{tor} \cong 2.85$ T, $I_p \cong 2$ MA; $|n|=2$.

5. DAMPING OF TAE

γ/ω was measured in ohmic plasmas, with 1 MA$<I_p<$3 MA; $1x10^{19}\ m^{-3} < \bar{n}_e < 5x10^{19}\ m^{-3}$; 1 T$<B_{tor}<$3.5 T; odd and even low-n excitation.: $\mathbf{10^{-3}} \leq \gamma/\omega \leq \mathbf{10^{-1}}$ ($\rightarrow$ extreme sensitivity to plasma equilibrium).

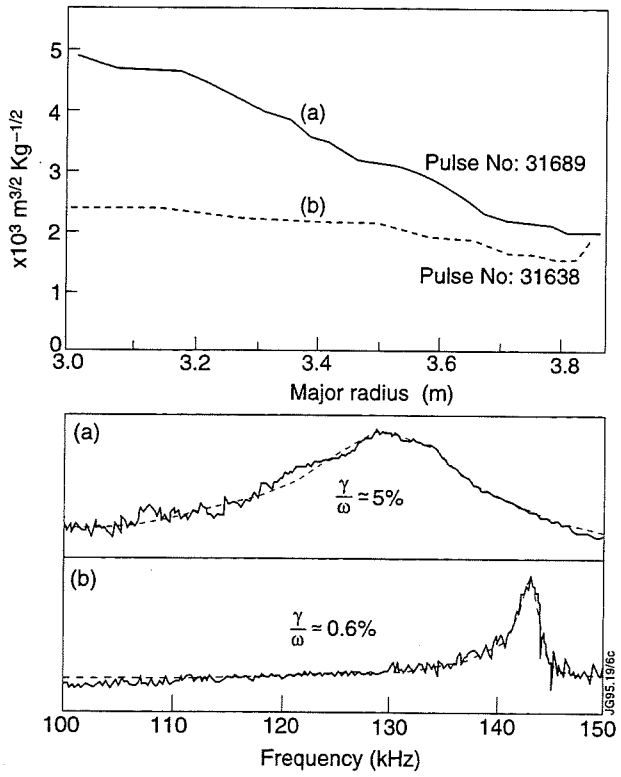

Fig. 6 Continuum damping: relationship between the profile of $g(r)=1/(q(r)\rho(r)^{1/2})$ and the TAE damping, in two similar ohmic discharges, with $|n|=2$; $\bar{n}_e \cong 4x10^{19}\ m^{-3}$; (a) $B_{tor} \cong 1.8$ T, $I_p \cong 2$ MA. (b) $B_{tor} \cong 2.8$ T, $I_p \cong 2.3$ MA.
Strong radial dependence of g(r), curve (a): gaps not aligned $\rightarrow$ strong damping, $\gamma/\omega \sim 5\%$.
Flatter g(r), (b): gaps aligned $\rightarrow$ less damping.

6. OBSERVATION OF MULTIPLE KINETIC ALFVÉN EIGENMODES

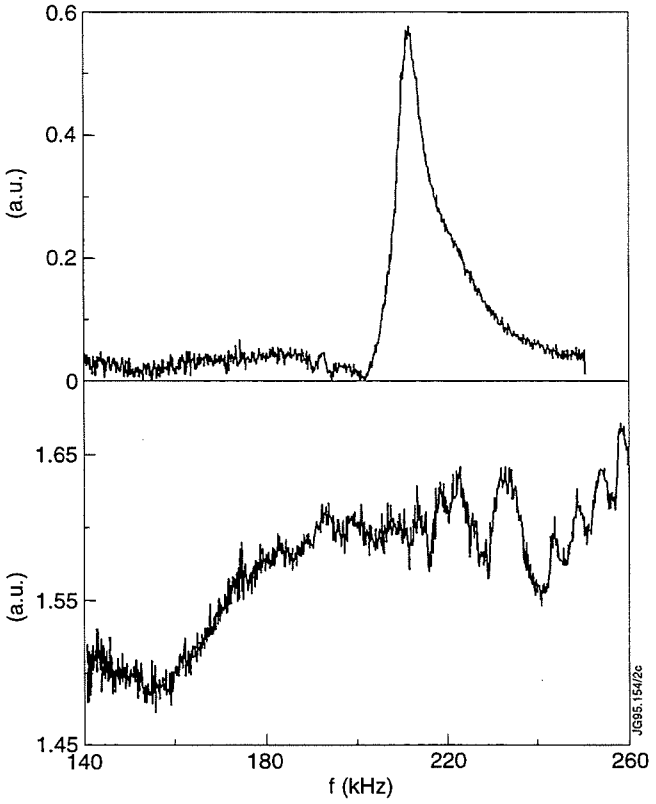

Fig. 7 B_{pol} probe signals for moderate (top) and high plasma current (bottom) in the same ohmic discharge #34073. The single TAE observed for low values of I_p is transformed into multiple peaks at higher I_p, corresponding to a hotter plasma. As these modes are externally driven with |n|=2 and the plasma rotation is negligible, they cannot correspond to Doppler shifted peaks of different n. (a): t = 3.5 s; I_p ~ 2 MA; B_{tor} ~ 2.5 T; $\bar{n}_e$ ~ 1.9 10^{19} m^{-3}; T_e ~ 2.2 keV. The single TAE has f ≃ 210.5 kHz, $\gamma/\omega \simeq$ 1.4 %; f_{TAE}^0 ~ 200 kHz. (b): t=9.5 s; I_p~4.1 MA; B_{tor}~ 2.9 T; $\bar{n}_e$ ~ 3 10^{19} m^{-3}; T_e~3.2 keV; f_{TAE}^0 ~ 180 kHz.

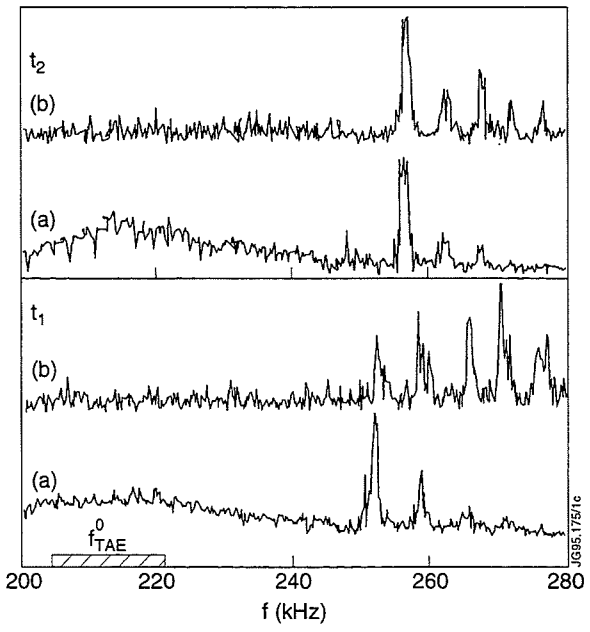

Fig. 8 Spectrum of magnetic (a) and density (b) perturbations in the AE range for LHH (2.5 MW) and ICRH (6 MW) in minority heating, raising T_e, T_i and T_e/T_i and reducing kinetic damping without significant resonant particle populations. Multiple resonances characterised by the same |n|=2 appear at $f>f_{TAE}^0$. The reflectometer frequency corresponds to r/a~0.5. These driven density perturbations in the plasma core, linked to $\delta E_{||}10$, emphasise the non-ideal MHD character of the modes. Two successive scans, at t_1 = 19 s and t_2 = 20 s are shown. I_p ~ 3 MA; B_{tor} ~ 3.2 T; n_e ~ 2.5 10^{19} m^{-3}; T_e ~ 6.3 keV; T_i ~ 2.9 keV. $\Delta f/f$~2.5 % and $\gamma/\omega < 10^{-3}$.

Interpretation of multiple peak AE spectra:
Non-ideal MHD effects: finite Larmor radius and finite $E_{||}$.

Analytical models for hot plasmas: several weakly damped modes with regularly spaced frequencies form inside a potential well above the gap, as in a quantum harmonic oscillator. Non-ideal parameter: $\lambda = 4\ m\ s\ /(r_m\ \varepsilon^{3/2})\ \rho_i\ (3/4 + T_e/T_i)^{1/2}$, with $\varepsilon \simeq 2.5\ r_m/R$. λ is calculated at r_m, where $q(r_m)=(m+1/2)/n$. When $\lambda > \gamma/(\omega\ \varepsilon)$ a transition from a 'cold' TAE (ideal MHD) to multiple KTAE occurs.

Multiple AE spectra in the TAE/EAE frequency range, with similar peak frequency spacing, resonance width and mode numbers, have been observed with LHH only, NBI and ICRH only. Very weakly damped ($\gamma/\omega < 10^{-4}$) multiple modes were also seen, mainly on the reflectometer, during I_p ramp-down experiments, corresponding to sudden variations in l_i and presumably in magnetic shear.

The damping rates observed for the driven multiple KTAE/KEAE were in most cases significantly lower than for the 'cold' TAE: γ/ω **< 10^{-3} - 10^{-4}**,
Wave-particle destabilisation should be easier than for TAE/EAE. Multiple peaks at $f>f_{TAE}^0$ have indeed been observed, for ex. with ICRH (P>6 MW) and NBI (P(140 kV)> 1.5 MW).

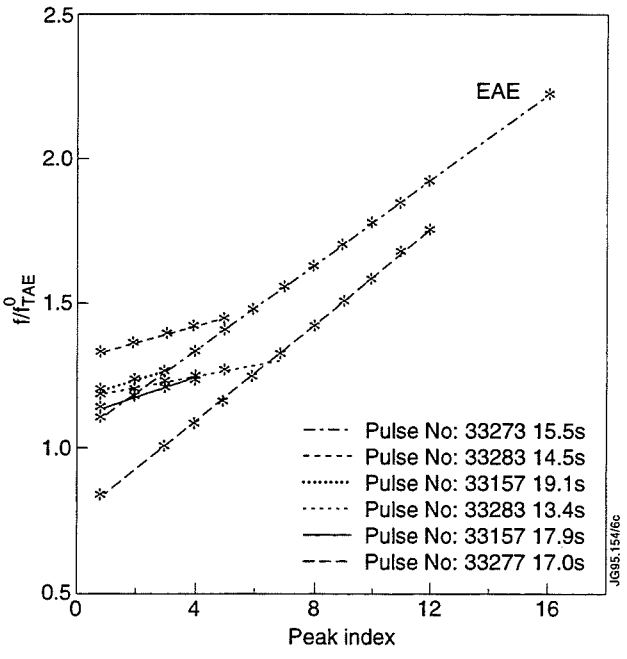

Fig. 9 Example of peak frequency distribution of the multiple kinetic AE driven by an external antenna for a number of additionally heated JET discharges. The peak spacing remained similar for consecutive sweeps when the plasma conditions were maintained approximately stationary.

7. AE EXCITATION BY ICRH BEAT WAVES

Motivation: possibly higher n and larger amplitudes —>study AE effects on particle orbits. Wave-wave: f_1-f_2 = Δf = f_{TAE}; $\underline{k}_1$-$\underline{k}_2$ = $\underline{k}_{TAE}$ ~1/2qR (non-linearity: fluid velocity, current or ponderomotive?)

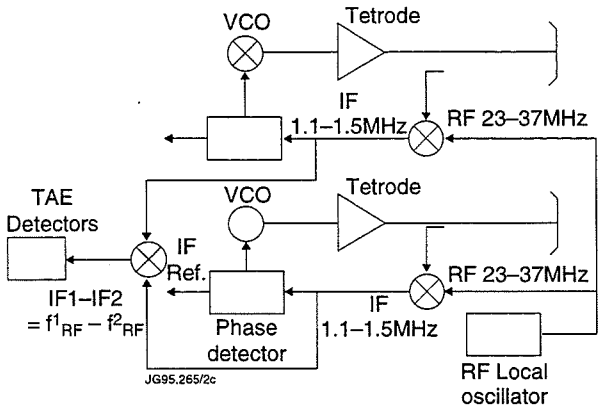

Fig.10 Passive scheme: simply measure at Δf

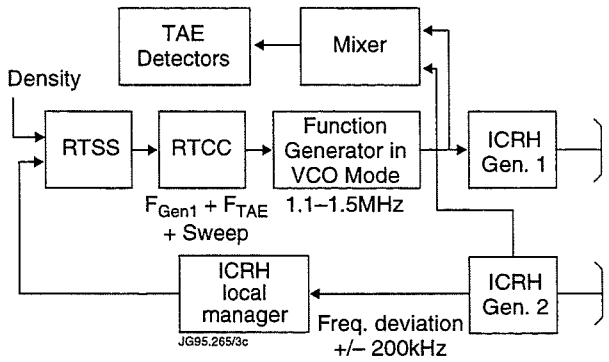

Fig. 11 Active mode: impose $\Delta f = f_{TAE}^{0}$ + sweep

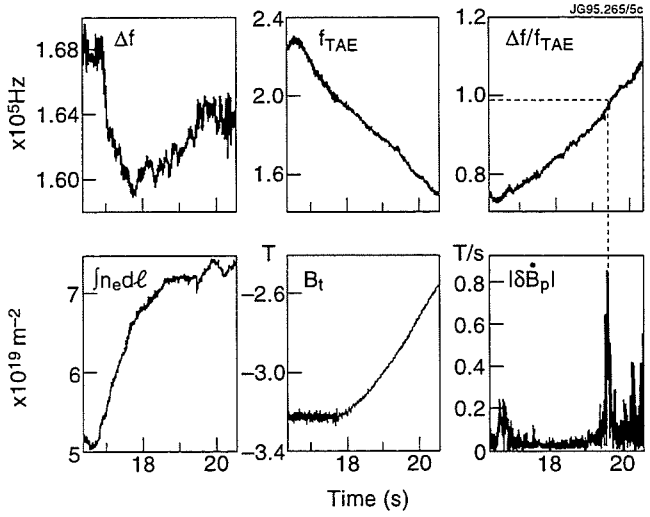

Fig.12 ICRH beat wave: passive scheme

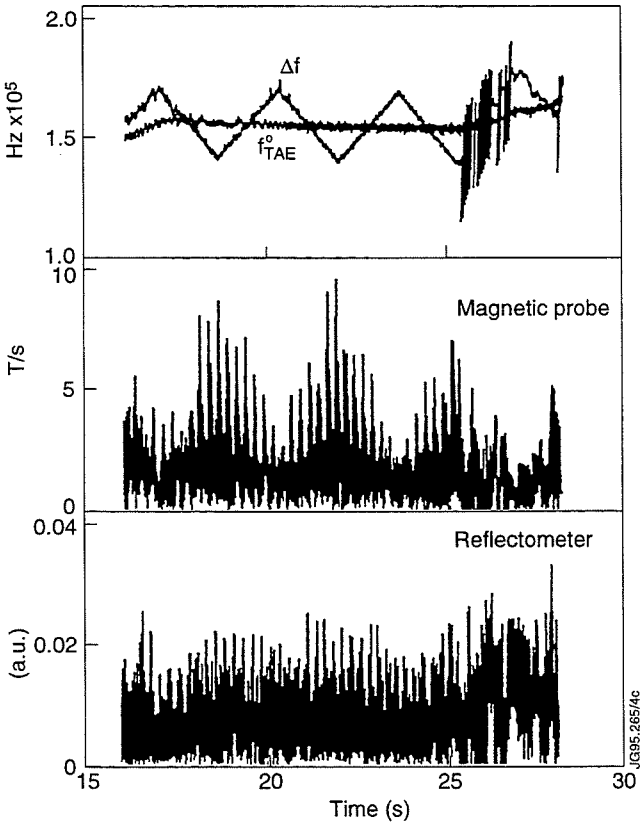

Fig.13 ICRH beat wave results: active mode

8. CONCLUSIONS

- A new active diagnostic for AE has been developed at JET. It is based on external antenna excitation and synchronous detection of the plasma response.
- Linearly stable TAE and EAE have been driven and identified by their frequency dependence on the density and the magnetic field. Driven mode structures ($|n| < 4$) have been selected and identified.
- TAE damping rates have been measured for the first time. Different absorption mechanisms and specifically continuum damping in the core and at the edge cause a large range of γ/ω in ohmic discharges, with an extreme sensitivity to the details of the plasma equilibrium.
- Under plasma conditions which correspond to the predicted departure from ideal MHD due to kinetic effects, multiple driven AE have been detected in the TAE/EAE range. Contrary to the 'cold' TAE, these modes have been observed on the reflectometer, i.e. as density oscillations in the plasma core, as well as on the magnetic probes. The observed modes belong to the general class of kinetic AE.
- AE excitation via non-linear beating of two ICRH waves has also been demonstrated experimentally.
- These studies will be continued during the JET D-T experimental phase in order to investigate the linear stability of AE as well as the effects of large amplitude AE on particle orbits in the presence of resonant alpha particles produced by fusion reactions.

The Authors would like to thank the JET Team for experimental support. This work was partly supported by the 'Fonds national suisse pour la recherche scientifique' within a JET/CRPP Task Agreement.

REFERENCES

TAE Theory: C.Z. Cheng et al., *Ann. Phys.* (New York) **161**, 21 (1985); L.Villard, G.Fu, *Nucl. Fusion* **32**, 1695 (1992).; G.T.A.Huysmans et al., *Phys. Fluids B* **5**, 1545 (1993).

AE previous observations: K.L.Wong et al., *Phys. Rev. Lett.* **66**, 1874 (1991); W.W.Heidbrink et al., *Nucl. Fusion* **31**, 1635 (1991); W.W.Heidbrink et al., *Phys. Rev. Lett.* **71**, 855 (1993).

AE Damping: R.Betti, J.P.Freidberg, *Phys. Fluids B* **4**, 1465 (1992); N.N.Gorelenkov. S.Sharapov, *Physica Scripta* **45**, 163 (1992); J.Candy, M.N.Rosenbluth, *Plasma Phys. Contr. Fusion* **35**, 957 (1993); S.Poedts et al., *Plasma Phys. Contr. Fusion* **34**, 1397 (1992).

Kinetic AE: R.R.Mett, S.M.Mahajan, *Phys. Fluids B* **4**, 2885 (1992); J.Candy, M.N.Rosenbluth, *Phys. of Plasmas* **1**, 356 (1994); H.L.Berk et al., *Phys. Fluids B* **5**, 3969 (1993); S.Sharapov et al., JET-P(94) **61**, p.105 (1994); A.Jaun, Ph.D Thesis, *CRPP/EPFL* LRP **513/95** (1995).

Investigation of Performance Limiting MHD Effects using the New JET Diagnostic Fast Data Acquisition System

R D Gill, B Alper, A D Cheetham, A W Edwards, E Lyadina, S Dillon.
JET Joint Undertaking, Abingdon, Oxfordshire, OX14 3EA, UK.

DETECTION SYSTEM

A new soft X-ray diagnostic system with a sophisticated data collection and storage system has been developed at JET. The soft X-ray system is based on the use of a large number of compact pinhole cameras which use 35 element silicon photodetectors. Each element is about 4 x 1mm and the detectors are used in the photovoltaic mode.

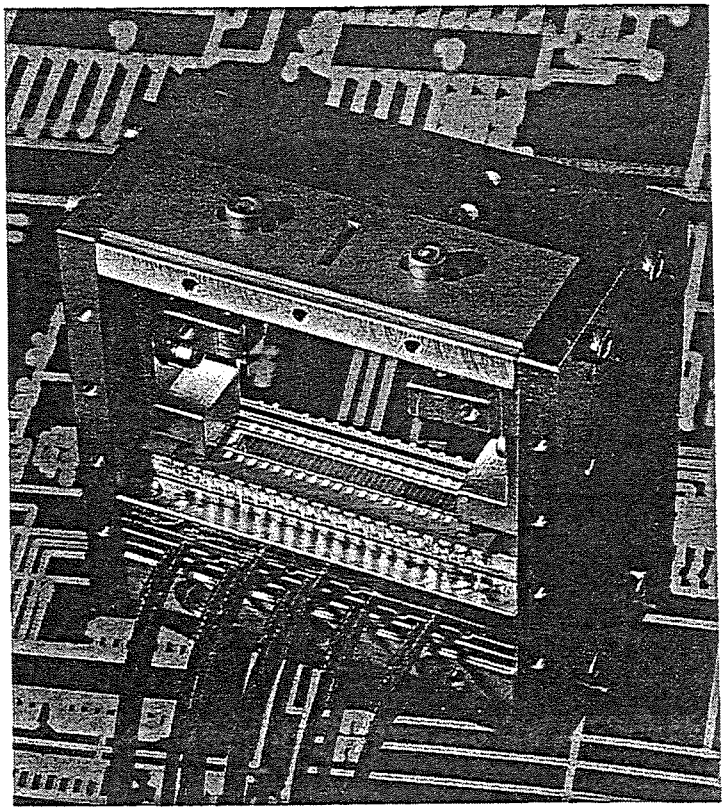

Fig. 1 Photograph of soft X-ray camera (enlarged x 1.7)

In order to obtain many different views of the plasma the cameras are placed within the vacuum vessel, but separated from it in a secondary vacuum by a Be viewing window. As the JET vacuum vessel is hot (≤350°C) the detectors are water cooled to room temperature to reduce noise. Eleven cameras view the plasma in one poloidal plane and a twelfth is mounted displaced in toroidal angle by 3/8 x 2π in order to determine toroidal mode numbers.

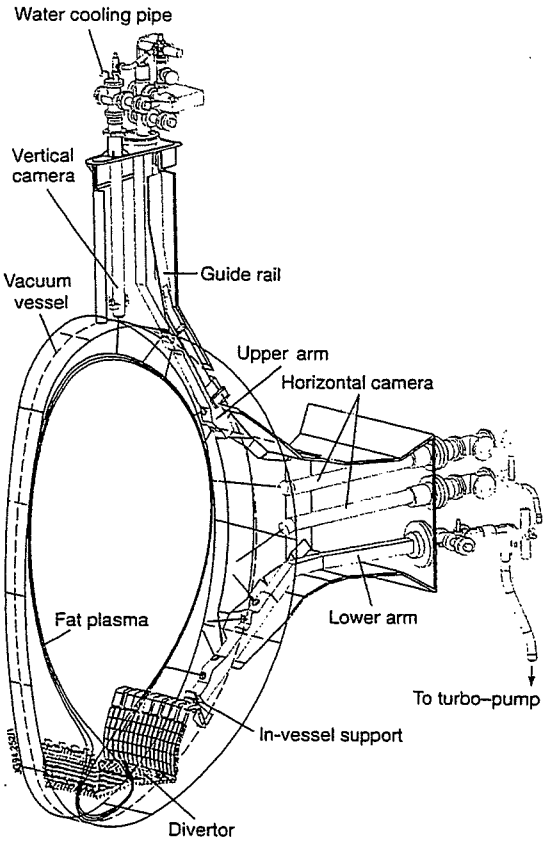

Fig.2: Engineering drawing showing the mounting of the soft X-ray cameras.

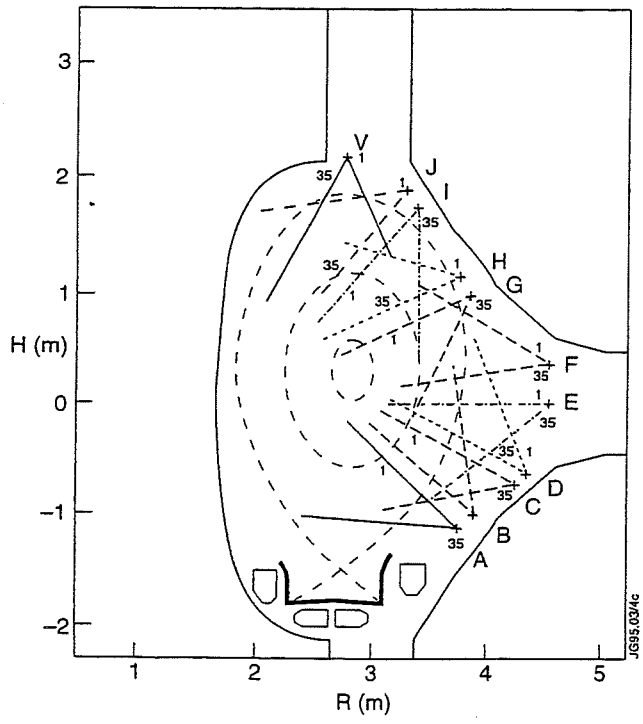

Fig.3: Lines of sight of the first and last element of each camera showing the good coverage of the plasma

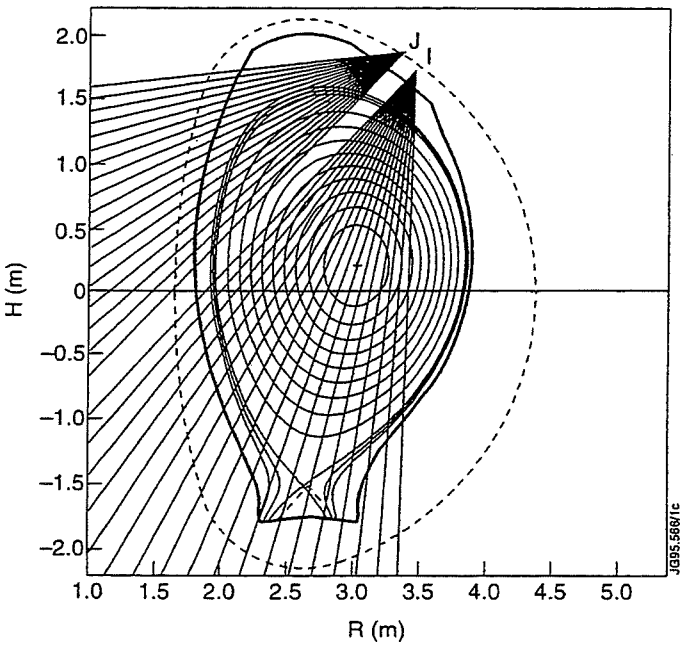

Fig.4: Individual lines of sight of two cameras superimposed on a reconstruction of the magnetic flux surfaces from magnetic measurements.

The system has been installed in JET throughout the operational campaign which finished this year and it will continue to operate up to the D-T campaign in 1996. A few full power D-T shots will unfortunately cause serious damage to the detectors and for this reason a radiation hardened system of considerably different design is being developed. A single camera with no Be window will be installed shortly to investigate fast events in the divertor which are visible only in the VUV.

DATA COLLECTION

A new data acquisition system (CATS) has been built for the soft X-ray cameras and other systems on JET. It will handle large volumes of data at very high rates. The soft X-ray system is based on placing the signal processing electronics and ADC as close as possible to the detectors and transmitting the digital data via optical fibres to the diagnostic hall (~200m away) where processing and storage take place.

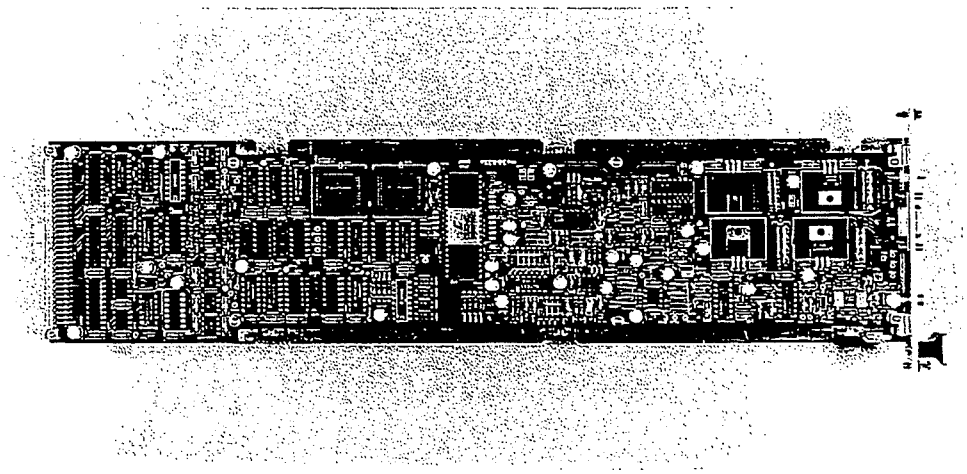

Fig. 5 Photograph of ADC card

The electronics near the machine has been designed to reduce electrical interference and noise and therefore each ADC card is electrically isolated from its neighbours and separately powered. A switchable variable gain amplifier is incorporated in the design to accommodate different levels of emission from the plasma. An eight-pole linear phase analogue filter is included to prevent aliasing. The signals are digitized at 1MHz and digitally filtered to provide data at a rate of 250kHz with a frequency cut off at 125kHz. The cards are assembled in racks of 19 and connected to a common backplane. A control card takes the data from each ADC card and sends it via a TAXI transmitter to the diagnostic hall for storage. Each ADC is clocked simultaneously.

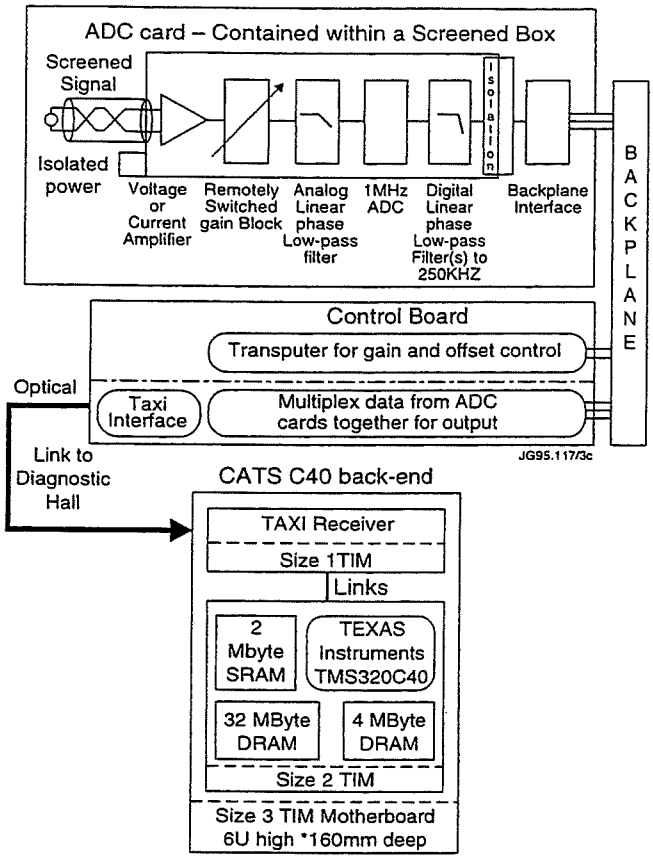

Fig. 6 Schematic of ADC card, control board and data storage electronics

The data storage system is based on microprocessors which make the system modular and easy to extend. An intelligent trigger system has been developed which allows the physicist to select events of particular interest. In addition to the fast data acquisition, a large number of the channels can be digitally filtered down to very much lower frequencies in order to provide selected data for the entire discharge. This system has also been used to collect fast data from other diagnostics: the magnetics, ECE temperature measurements, reflectometry and Hα measurements. All this data is collected in time synchronization.

TOMOGRAPHY

Tomography techniques are used to invert the line integral experimental measurements $f(p, \psi, t)$ into the local spatially resolved X-ray emissivities $g(r, \theta, t)$ i.e. to invert the set of equations:

$$f_i(p_i, \psi_i, t) = \int g(r, \theta, t) d\ell_i$$

where the index i denotes the different detectors.

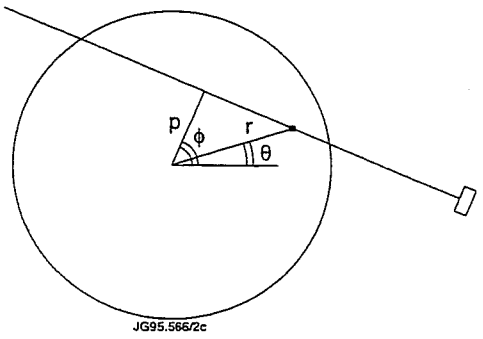

Fig. 7 Co-ordinates used for tomography

The technique previously used on JET was the well known Cormack inversion method using the Fourier-Zernicke expansion. However, the noise on the inverted values of g may be reduced by a space-time processing technique which uses statistical information from all of the experimental taken at a sequence of times to regularise the procedure. The coefficients $a_{m\ell}(t)$ given by the Cormack method have stochastic perturbations imposed on them by noisy experimental data. The effects of these perturbations on the reconstructions have been reduced by use of the stabilizing factor method proposed by Tichonov. This method uses a statistical analysis of the time behaviour essentially to smooth the coefficients of $a_{m\ell}$ and to reduce their values to the lowest level compatible with their statistical behaviour. The method is most valuable when high m number perturbation contribute prominently to the observed data.

FAST SAWTOOTH CRASH

Fast sawtooth crashes were first discovered in JET about a decade ago. Early tomographic reconstructions of data from a two camera system showed that first the original hot plasma centre was displaced off axis to the q = 1 surface and then a crescent pattern of emission was observed as the energy became redistributed uniformly over the region of the plasma within the q = 1 radius. Both the speed of the crash and the redistribution mechanism has lead to several new theoretical ideas on the mechanisms of the sawtooth. The data did not correspond to the Kadomtsev model.

One of the limitations of a two camera system is that only a limited number of poloidal harmonics may be reconstructed and, although various simulation tests suggested that the tomography had correctly reproduced the plasma emission, it was realised that some doubt could be cast on our interpretation, which could only be entirely removed by making observations on

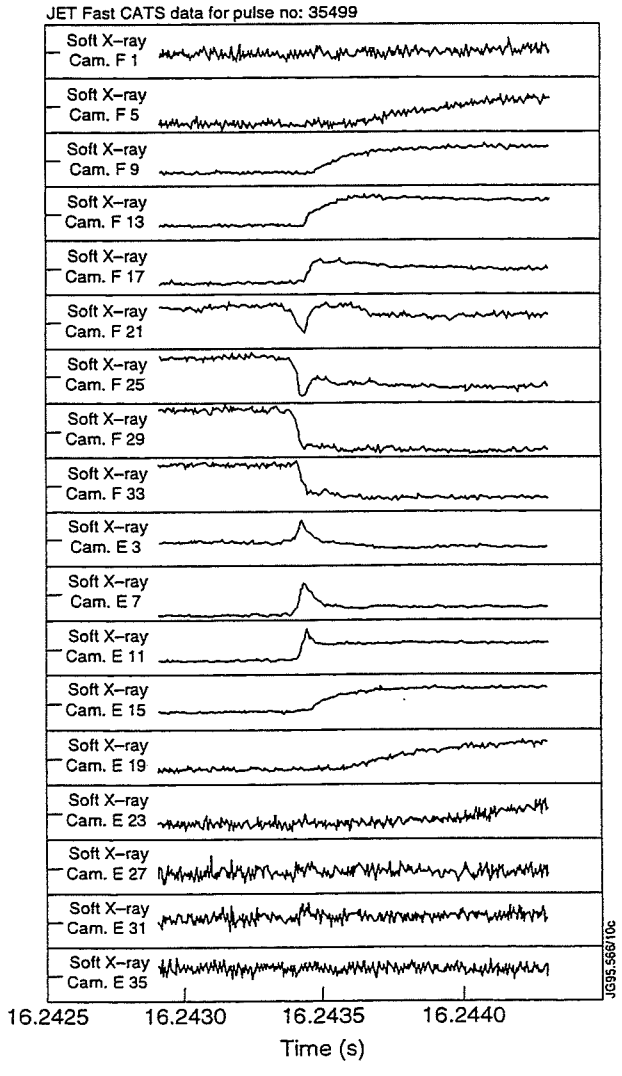

Fig. 8 Time variation of the soft X-rays during a sawtooth

a sawtooth with a larger number of cameras. The new system fulfils this requirement as there are essentially six independent views of the plasma enabling the construction of modes up to at least m = 5.

The sawtooth analysed here occurred, without precursors, during a 2.6MA, 3.3T shot with T_{eo} = 8.0keV, n_{eo} = 4.5 x $10^{19}m^{-3}$. Additional heating of 11MW of ICRH was applied. The line integrated signals for the sawtooth are shown together with the tomographic inversions taken at the times indicated. The three stages of the collapse are clearly seen: initial movement of the core; formation of crescent shape; collapse to a symmetric state with a region of approximately constant emission within the q = 1 surface. This particular sawtooth is also extremely fast with the whole process over in ~100μsec. This data gives a very close confirmation of previous JET work on fast sawteeth.

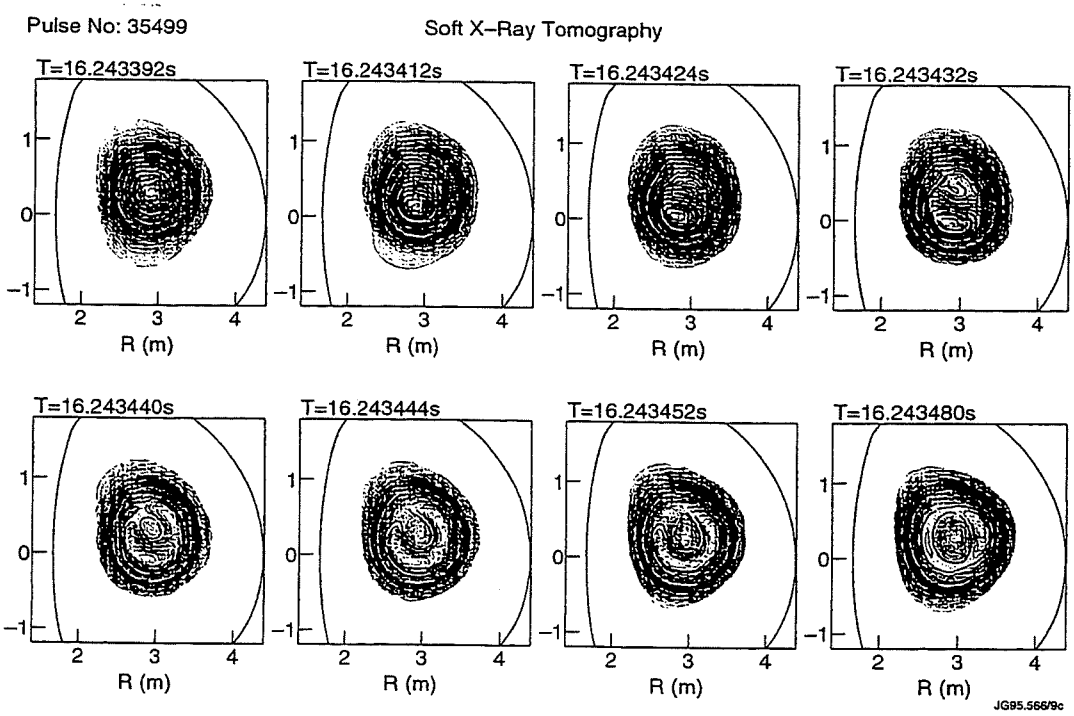

Fig. 9 Reconstructed soft X-ray emission during the rapid collapse of the sawtooth

DISRUPTIONS

Many tokamak discharges are terminated by a disruption which is sometimes preceded by a series of minor disruptions. It is generally accepted that disruptions have a variety of causes such as too low a q value, too high a density or impurity density, influx of pellets or UFO etc. Although each disruption proceeds in an individual way the final events leading to the negative voltage spike and current decay are generally the same. On the soft X-rays and ECE temperature measurement the final event is seen as a rapid cooling of the central region of the plasma followed by a characteristic T_e and X-ray spike coincident with the negative voltage spike. The rapid cooling phase has been identified theoretically as due to the growth and interaction of a number of different mhd modes leading to the loss of confinement. Experimentally this phase has always been observed in JET as a plasma

erosion, which in the older tomographically reconstructed profiles have always exhibited an m = 1 characteristic only. However, with the new multi-camera system which can resolve much higher m-numbers it could be hoped that the higher m-number modes might now be observed as predicted.

The reconstructions clearly show the m = 1 erosion and cold bubble formation at the plasma centre as before, but, in addition, show a clear m = 2 structure for the first time. It is possible that even higher m-numbers appear at larger radii and have not yet been detected due to the lower emission towards the plasma edge.

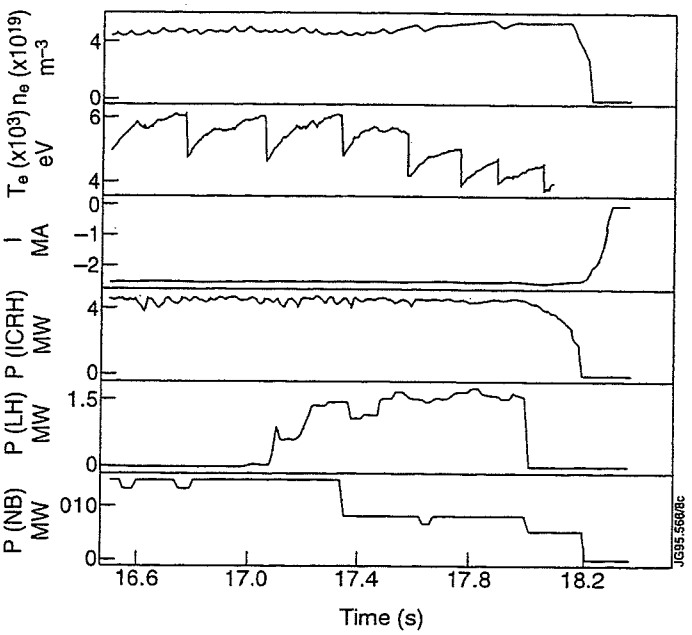

Fig. 10 General development of disruption

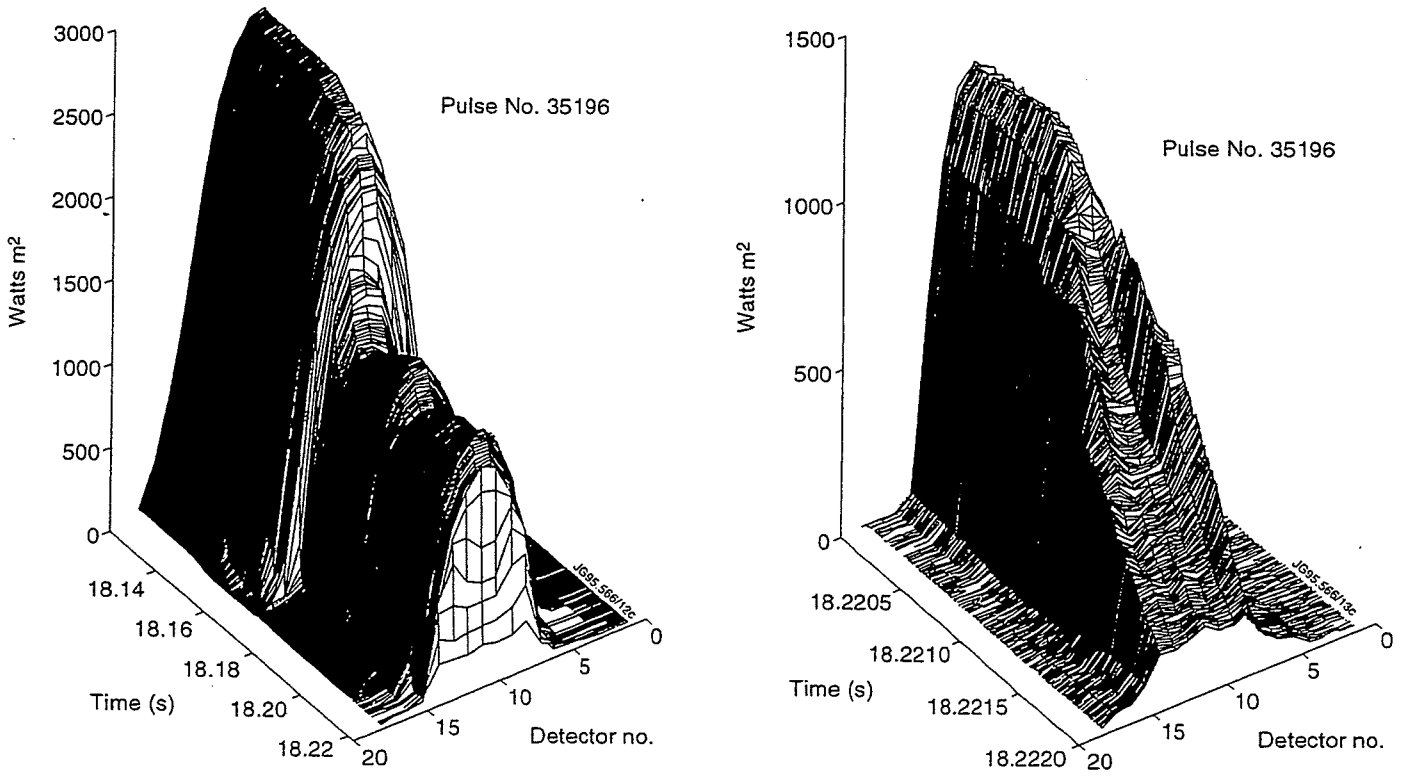

Fig. 11 Line integrated soft X-ray data from one camera

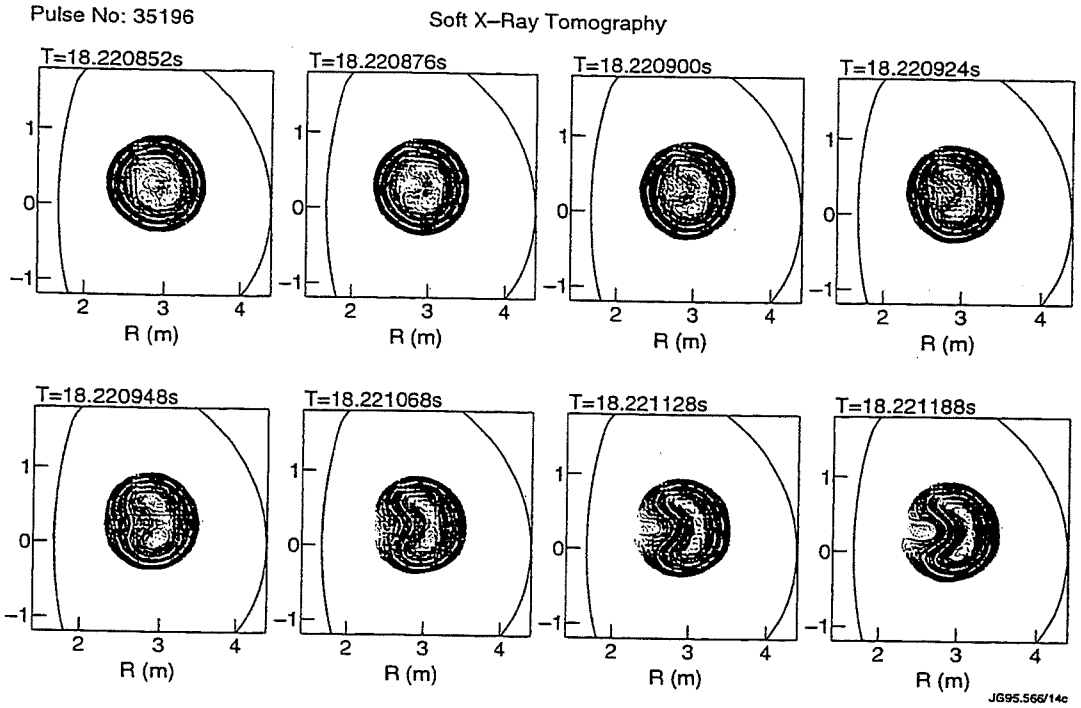

Fig. 12 Reconstructions of the disruption at the times indicated

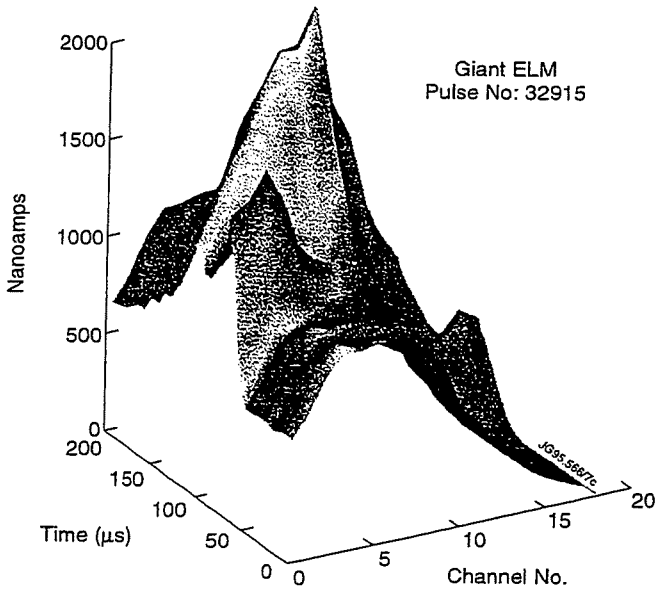

Fig. 13 Time development of an elm seen by a single soft X-ray camera

ELMS

Elms are present in most JET discharges with an X-point. They limit impurity build up within the plasma and sometimes terminate extended periods of high plasma performance. In H-mode discharges the plasma has a high temperature close to the separatrix and therefore the effects and structure of the elms can be studied with the soft X-ray cameras.

As seen by a single camera the elms often consist of a series of sharp spikes of emission quite limited in space and time. Some of these spikes are clearly related to increased emission from the divertor strike zones or from the X-point. However, by

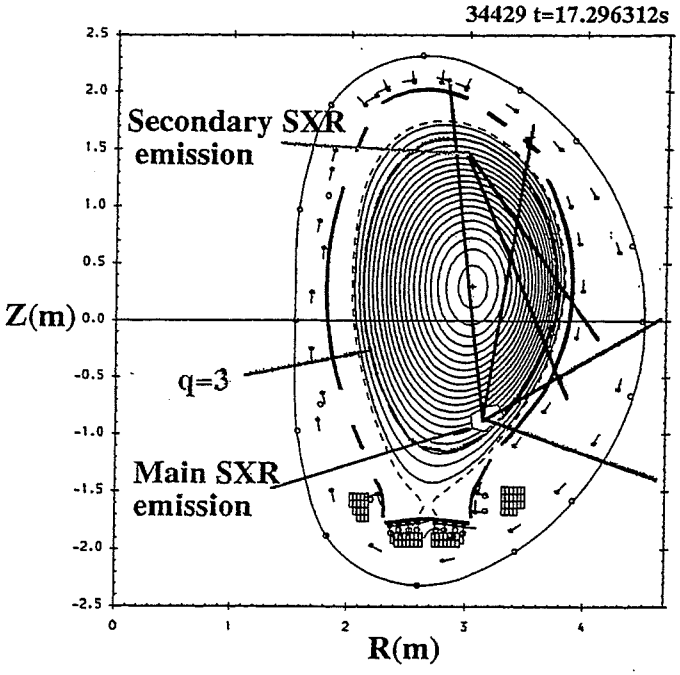

Fig. 14 Determination of the location of two sharpemission spikes

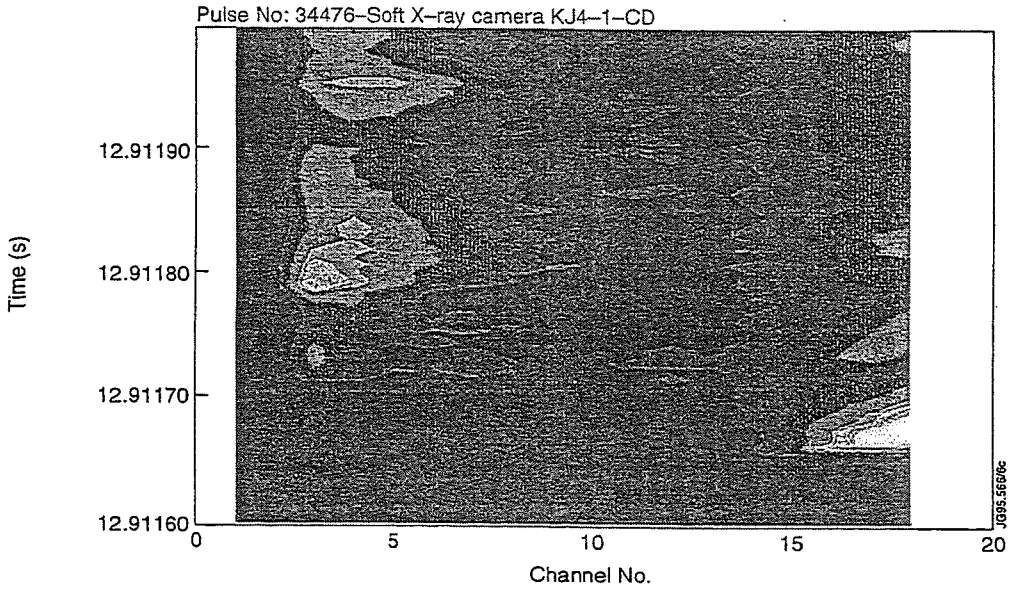

Fig. 15 Contour plot showing time development of an elm

looking at correlations from the lines of sight of the different cameras it is clear that some of the emission spikes originate well within the plasma. The origin of these is not understood, nor is it understood how the X-ray emission can increase so rapidly even if non thermal effects are present, as suggested by the ECE observations. It is expected that more detailed analysis of these data will provide a clearer picture of the sequence of events in giant elms. Correlations with other diagnostics such as the Hα emission, the magnetics and ECE will play an important role in this.

PERFORMANCE LIMITS

JET discharges with high levels of neutron emission often suffer degradation which may be triggered either by elms, mhd instabilities at the plasma edge or sawteeth . The role of each of these varies in different discharges and with the plasma pressure. The degradation in performance is a rather slow affair as the changes which occur to the plasma energy and neutron yield are slow compared at least with the sawteeth or elms.

It is thought that the degradation may be associated with the mhd effects at the plasma edge and these can be clearly observed with the soft X-ray cameras, magnetics and ECE. From the X-rays it can be seen that the mode, which probably has an m = 5, n = 1 structure is limited to the outer region of the plasma just outside the q = 3 radius.

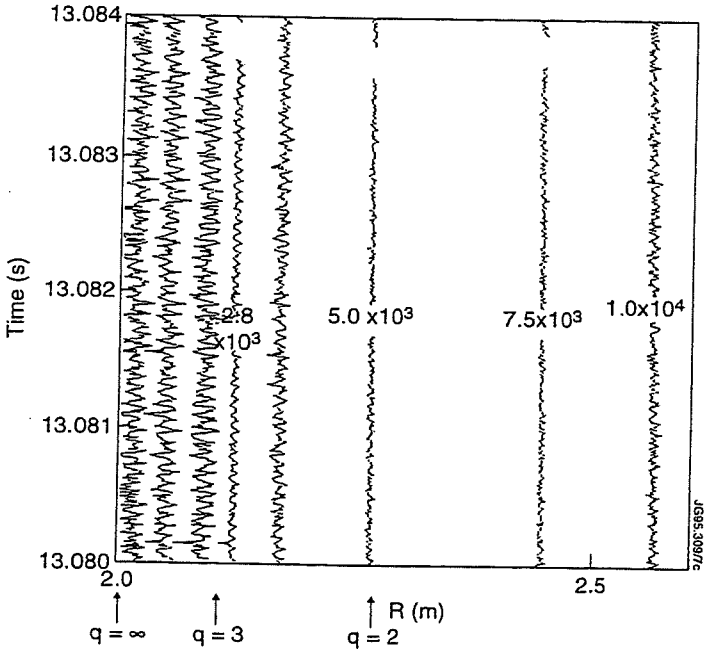

Fig. 16 Mhd mode observed in outer channels

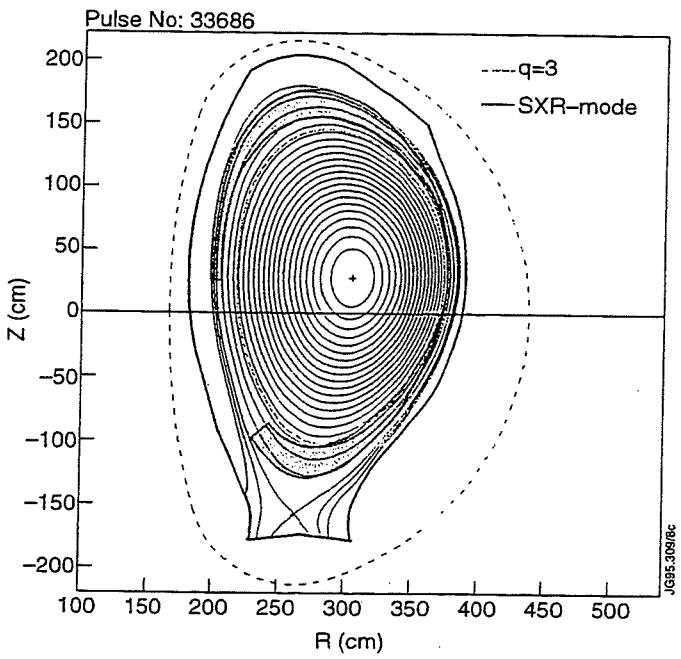

Fig. 17 Radial location of regions of observation of outer mode

CENTRIFUGAL EFFECTS ON IMPURITIES

In some JET discharges with very high rotation velocities it has been observed that the X-ray profiles as seen with the vertical camera are very peaked towards the plasma edge at a large major radius. Tomographic inversion of this data has confirmed this and shows a large degree of asymmetry. In these shots the rotation (22kHz) is caused by high levels of neutral beam power of up to 20MW. The most probable explanation for these observations is that the high Z impurity ions within the plasma are located mainly at large major radii due to the centrifugal forces acting upon them. There is conclusive evidence from pulse height analysis spectra that these JET discharges do indeed contain significant quantities of Cr, Fe and Ni. Calculations show that the observed asymmetries are in reasonable agreement with experiment.

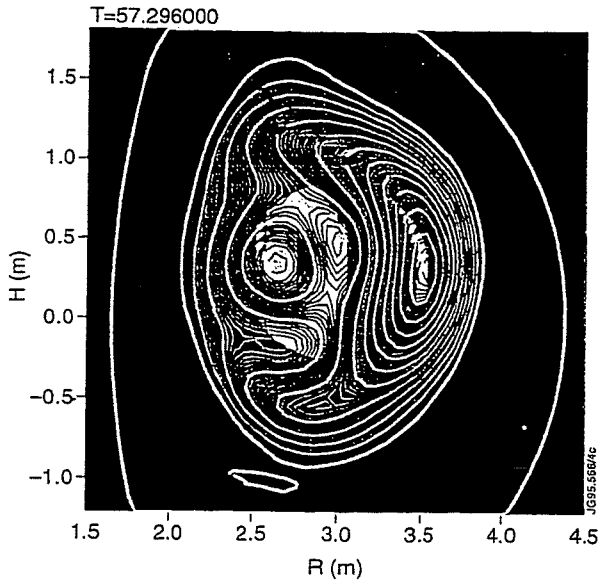

Fig. 18 Reconstructed X-ray emission showing strong asymmetries

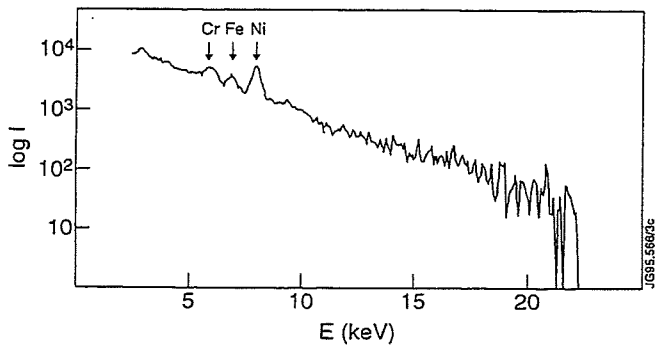

Fig. 19 Pulse height analysis spectrum showing various strong metal lines

NEW SYSTEMS

VUV Camera. Si diode detectors similar to those used for X-rays may be used to detect VUV radiation if they view the plasma without a Be window. A compact camera of this sort is presently being installed at position F, orientated to view the divertor region. It will have high time resolution. The focal length of the camera has been increased to improve the spatial resolution. It is intended to use this system to provide increased information on fast instabilities in the divertor region.

D-T Cameras. Unshielded Si detectors cannot be used for X-ray detection in the high neutron fluxes expected in the D-T phase of JET operation in 1996. Because of the need to study mhd effects in this phase of the JET programme a new set of shielded detectors is being built to view the plasma from the median plane. The new cameras consist of 19 individual detectors assemblies embedded in a very large concrete and steel shield. The detectors are shielded from the plasma by ~1m of concrete and view the plasma down accurately machined pipes and through a Be window. The dimensions and solid angles of the detectors have been chosen to ensure reasonable values of the X-ray signal to neutron signal noise ratio. Installation is planned for early 1996.

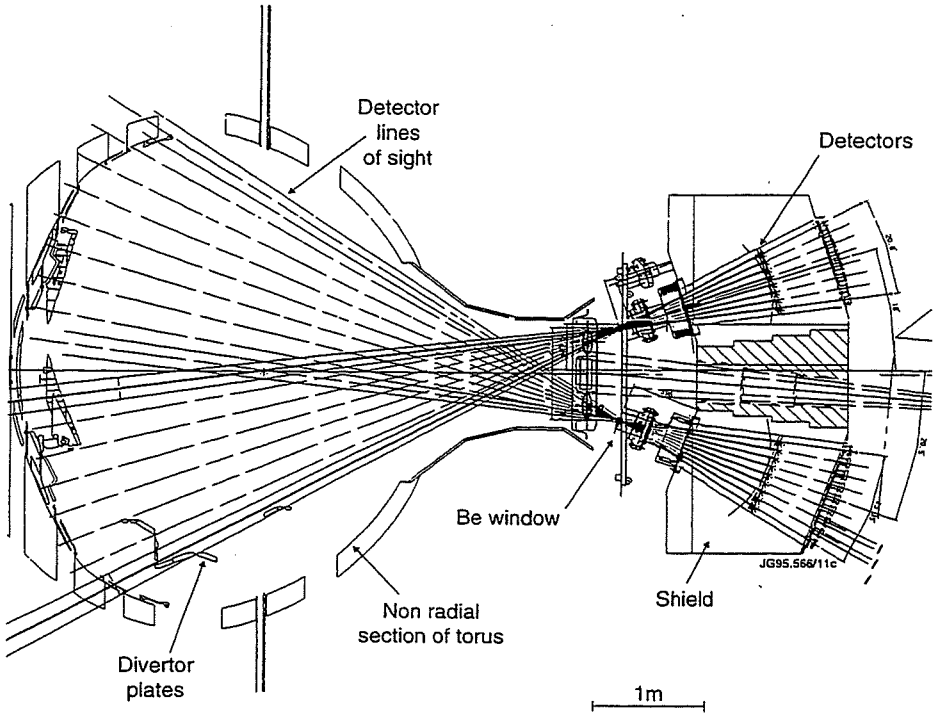

Fig. 20 D-T compatible soft X-ray camera

Measurements of Edge Electric Field, Electron and Impurity Ion Profiles during H-modes in the new JET Divertor Configuration

N C Hawkes[1], D V Bartlett, D J Campbell, N Deliyanakis, S K Erents[1], R M Giannella, P J Lomas, M G O'Mullane, N J Peacock[1], L Porte, A Rookes[2], P R Thomas, G Vayakis[3].

JET Joint Undertaking, Abingdon, Oxfordshire, OX14 3EA, UK.

[1] UKAEA/EURATOM Fusion Association, Culham Laboratory, Abingdon, Oxfordshire, OX14 3DB, UK.

[2] Imperial College of Science, Technology and Medicine, London, UK.

[3] Present address: ITER JWS, San Diego, La Jolla, CA 92037, USA.

INTRODUCTION

- In several of the present theories of the H-mode [1,2], it is argued that the H-mode occurs when edge turbulence is supressed through the action of a sheared perpendicular flow. The critical flow velocity involved is the ExB velocity, and thus the experimental parameter of interest to these theories is that of the gradient of radial electric field, E_r'.

- The results from measurements in JET H-modes contradict such theories. In general it is found that there is:

  1. no change in E_r at the transition
  2. no large E_r' prior to the transition

- It is found that the gradient in E_r develops at the separatrix coincident with the confinement improvement, and develops later (over 1-2 s) just inside the plasma due to the build-up of large pressure gradients (again as a result of confinement changes).

DIAGNOSTICS

- The radial electric field on JET is measured using charge exchange spectroscopy (CXRS) using the heating beams. The diagnostic has a space resolution of 0.8 cm and a time resolution of 3 ms, at the edge of the plasma, under optimum conditions.

- Views are available from the top and the bottom of the machine close to the poloidal plane, allowing Doppler measurements of poloidal velocity, v_θ, impurity ion temperature, T_I and density, n_I.

- The toroidal component to the views gives a measurement of toroidal velocity, v_ϕ

- This complete set of measurements enables us to compute the radial electric field from the force balance equation,

$$E_r = \frac{\nabla p}{Zen_I} - \left(v_\varphi B_\vartheta - v_\vartheta B_\varphi\right)$$

- Measurements of the edge profiles of n_e and T_e are obtained from a multichannel microwave reflectometer and an ECE hetrodyne radiometer. A two channel correlation reflectometer also provides information on the level of density fluctuations.

RESULTS

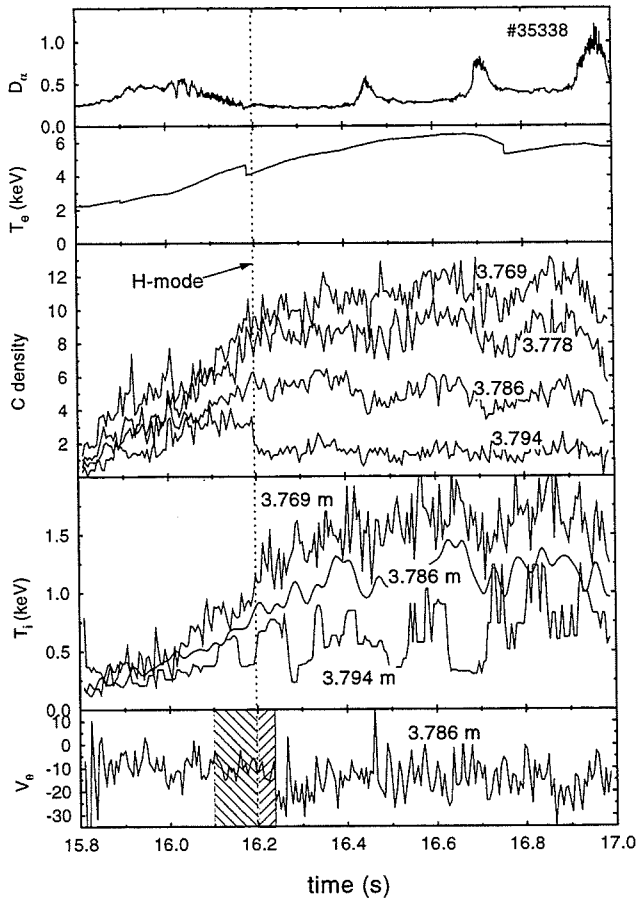

- The transition is indistinct in D_α, but drop in n_Z is clear. It coincides with a drop in reflectometer fluctation amplitude at 1.5×10^{19} m^{-3}. Also, a reduction in cross amplitude (from the correlation reflectometer) indicates a drop in the correlation time, τ_c, of the turbulence

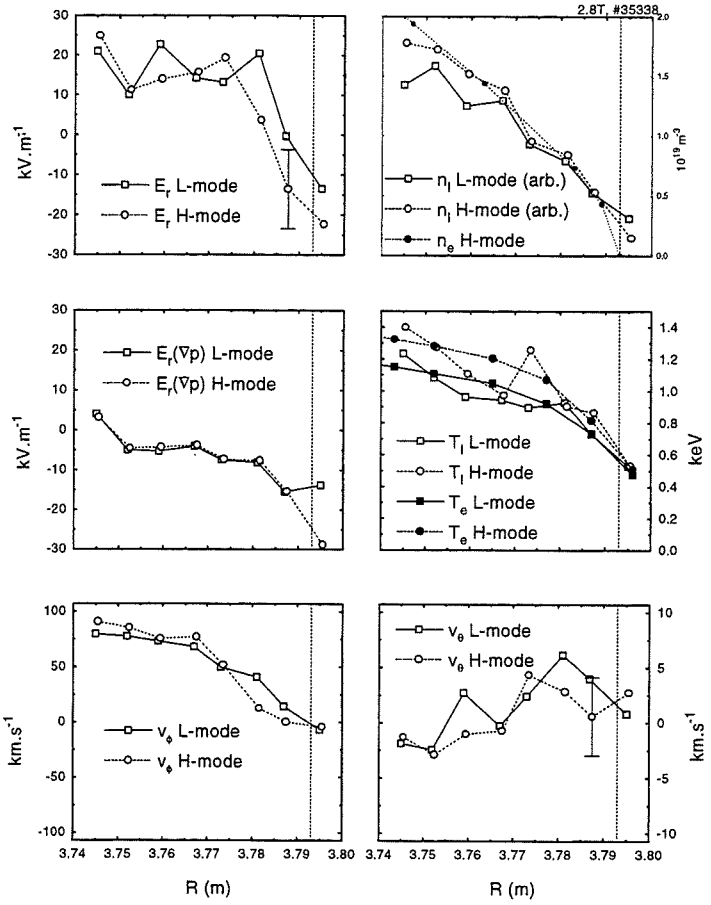

- Relative positions of n_Z, n_e and T_e are uncertain to within the accuracy of the EFIT reconstructions (inadequate for this work).
- T_e linked to v_ϕ of the CXRS using an MHD mode with a rotation frequency corresponding to v_ϕ at 3.786 m.
- T_e linked to n_e throught the radius where optical transparency sets in for the ECE emission
- The position of the separatrix within the n_e profile is established from the divertor target probe peak density (3.7×10^{18} m^{-3}) and DIVIMP modelling.
- Midplane separatrix n_e is calculated to be $3.1 \times 10^{18} m^{-3}$, position shown as vertical dashed line in figure.
- Error bars on E_r are those from v_θ only (tend to be dominant)
- (Vertical scales of P, v_ϕ and v_θ are the same in terms of the E_r contribution from these terms)
- Drop in n_Z occurs on the open flux surface (due to the setting-up of a transport barrier inside the plasma, preventing the efflux of C^{6+} ions)
- In this shot E_r is already present before the transition, due to the early build up of the pressure gradient (so here one could regard transition as triggered by a critical E_r, even if not of a catastrophic nature)

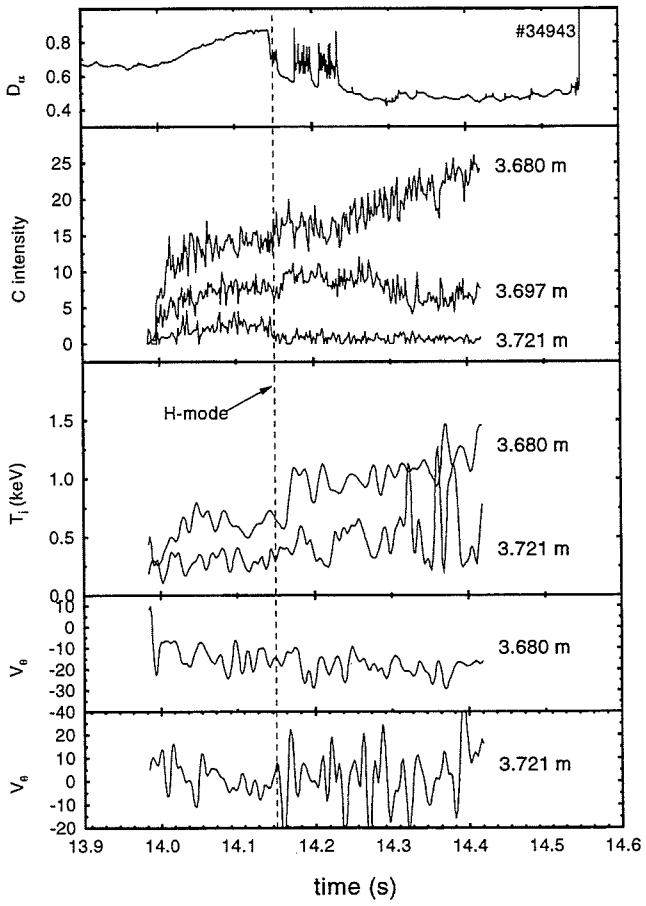

- Clear drop in D_α identifies time of L- to H-mode transition

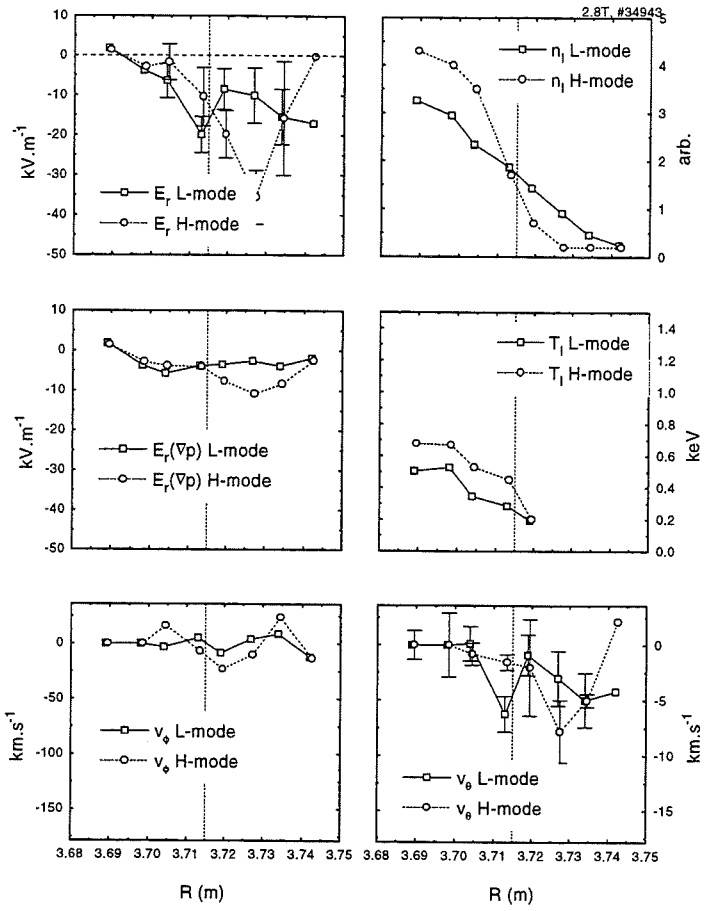

- In this example the separatrix is assumed to lie at a radius within that where there is a sudden drop in n_Z, as in the previous example (here there is no independent information on separatrix position).

- Here E_r is found to be low before and after transition.

- No significant change in E_r or V_θ is seen across the transition

- L-mode is 14.112—14.136 s, H-mode 14.158—14.178 s

PROFILE CHANGES DURING ELM ACTIVITY

- In general changes in v_θ are below the limit of measurement (~5km.s-1), although there is some evidence for changes at transition at or below this level).

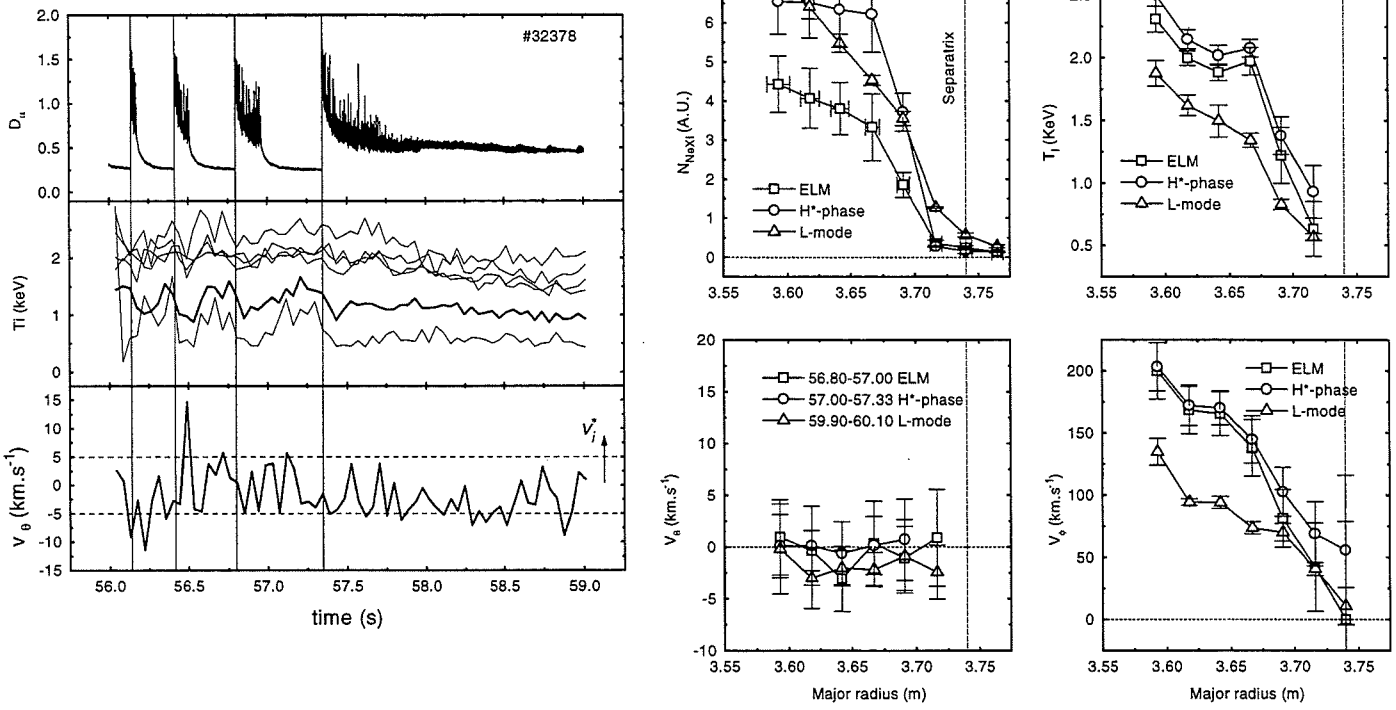

- Measurements made of neon impurity. ELMy periods induced by the strong gas feed.

- The highlighted chord is located in the steep part of the T_i gradient, therefore in the middle of the transport barrier. This chord is picked out to show that there is no detectable change in poloidal velocity (within the 5 km/s accuracy) during the ELMy periods.

- Radial profiles of quantities during the quiescent and ELMy H-phases show that other profiles are significantly affected by the ELM activity. The final phase, after 57.3 s is tentatively identified as a return to L-mode. The space resolution of these measurements (indicated by the radial error bars) is finer than channel spacing used.

PRESSURE PROFILES AT LONG TIMES

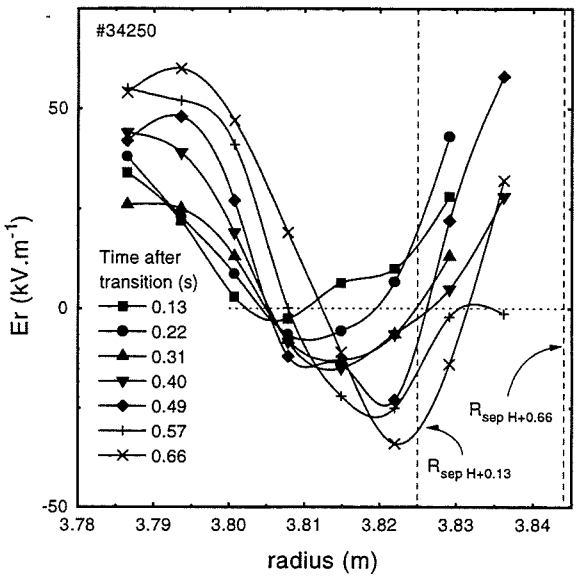

- Profiles of E_r calculated from the pressure gradient and v_ϕ terms during a high power H-mode (the measurement of v_θ is somewhat noisy in the early phase and is hence assumed to be small)

- The value of E_r minimum reaches -30 $kV.m^{-1}$ at 0.66 s after the transition.

- The width of the region of negative E_r is spread over 3 measurement channels (2.5 cm).

- No evidence that such a feature appears promptly at the moment of transition in the other examples shown

TRANSPORT SIMULATION

A time dependent simulation of C^{6+} ions demonstrates the reduction in density on open field lines as a consequence of the change in transport in the confined plasma, and the steady ramp up of density in the bulk plasma.

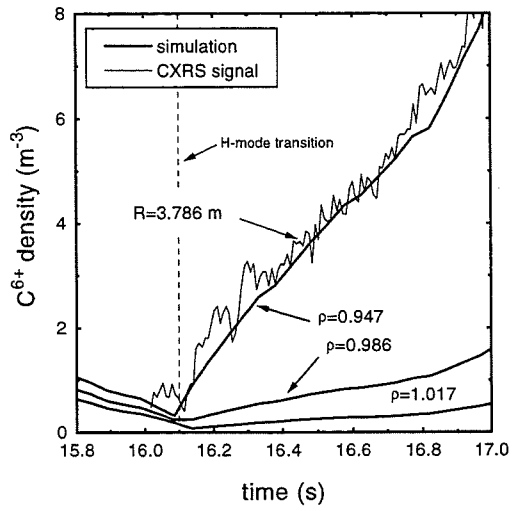

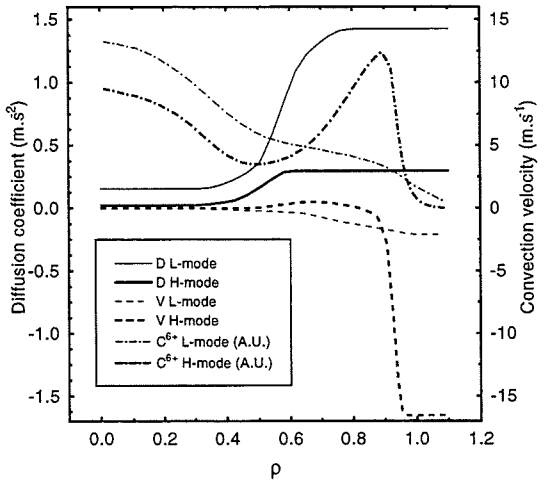

INTERPRETATION

- Many features of the H-mode transition in JET are similar to those seen in DIII using CXRS[3], except for the absence of a well in E_r formed at the transition. Even in the case of a fast transition in JET there is no large change to the pressure and velocity profiles.

- In the late H-mode phase a negative well develops in E_r. This is consistent with the existence of a barrier to transport of particles, heat and angular momentum. The toroidal velocity profile that results produces a radially increasing positive E_r contribution, while the pressure gradient profile contributes a negative E_r term, but only where the gradient is steep. These factors naturally lead to a negative well near the plasma edge

- It is possible that the level of turbulence is lower in JET L-mode than DIII, and thus requires a lower level of E_r shear to achieve turbulence supression[4]. However, this argument fails to account for the low level of E_r shear obtained shortly after the transition in JET.

- A fast drop in signal at the separatrix at the transition is consistent with measurements of Doppler shifts seen in emission lines[5]. At this radius a fast change in v_θ is required to maintain force balance with the E_r that develops from the background ion pressure change. We would expect to see evidence of this in VUV emission lines from the edge region of JET. There are some indications of this in particular ion stages of carbon (CV but not CIV or CVI), although instrumental abberations are likely to be important in this awkward spectral region.

CONCLUSIONS

- In several of the present theories[1,2], it is argued that the H-mode occurs when edge turbulence is supressed through the action of a sheared perpendicular flow. The critical flow velocity involved is the ExB velocity, and thus the experimental parameter of interest to these theories is that of the gradient of the radial electric field, E_r'.

- The results from measurements in JET H-modes contradict such theories. In general it is found that there is:

  1. no change in E_r at the transition
  2. no large E_r' prior to the transition

- It is found that a gradient in E_r develops at the separatrix coincident with the confinement improvement, and develops later (over 1-2 s) just inside the plasma due to the build-up of large pressure gradients (again as a result of confinement changes).

- These results may be compared to those of COMPASS where the development of E_r may be inferred from changes in the impurity poloidal flow speed, although the radial location of this field can only be estimated from transport simulations.

- The absence of a large E_r gradient inside the separatrix at the moment of the L- to H-mode transition can only be reconciled with results from DIII-D if it is assumed that the level of turbulence in the JET L-mode is significantly lower than in smaller tokamaks

REFERENCES

[1] K. C. Shaing, E. C. Crume Jr. and W. A. Houlberg, Physics of Fluids B, **2** (1990) 1492

[2] H. Biglari, P. H. Diamond and P. W. Terry, Phys. Fluids B **2** (1) (1990) 1

[3] P. Gohil *et al.*, Nuclear Fusion, **34** (1994) 1057

[4] H. Biglari *et al.* IAEA Washington 1990, Plasma Phys. and Cont. Nucl. Fus. Research, Supplement **II** (1991) 191

[5] P. G Carolan *et al.* This Meeting, also EPS 1995, Bournemouth, Europhys. Conf. Abstracts, **19C** (1995) II-133

ACKNOWLEDGEMENT

This work was jointly funded by EURATOM and the UK Department of Trade and Industry.

MHD Stability Analysis of the Plasma Edge in JET Discharges

G T A Huysmans, C D Challis, T Hender[1], W Kerner, V V Parail.
JET Joint Undertaking, Abingdon, Oxfordshire, OX14 3EA, UK.
[1] UKAEA/EURATOM Fusion Association, Culham Laboratory, Abingdon, Oxfordshire, OX14 3DB.

ABSTRACT

- The stability of low-n external kink and ballooning modes has been analysed, using the CASTOR code, for both hot ion H-mode discharges and high β_p JET discharges. In particular, the influence of the edge pressure gradient and the edge current density, as reconstructed by the JETTO and TRANSP transport code, has been studied.

- For plasmas with a low triangularity access to the ballooning second stability region requires a large edge current. These edge currents however drive the external kink mode unstable and therefore no stable route exists into second stability. For high triangularity a lower edge current is required and a stable window into second stability can exist. In hot-ion H-mode discharges, the temporal evolution of edge current and edge pressure gradient shows a correlation of the onset of the slow roll-over in R_{dd} with a violation of the computed kink stability limit.

- For high poloidal beta discharges, a current ramp is found to induce an additional edge current and to bring the plasma into second stability. This yields an improved confinement regime with large edge pressure gradients. MHD Stability calculations for these discharges show that a stable route into the second stable regime is accessed.

INTRODUCTION

In H-mode discharges, a large pressure gradient develops at the plasma edge. In JET Hot-ion H-mode discharges the pressure gradient, locally at the plasma boundary, appears

to be limited by the ballooning mode stability limit [1] (see **Fig.10**). On a resistive diffusion time scale a bootstrap current develops as a result of the edge pressure gradient, leading to a finite current density at the plasma boundary. This edge current density can destabilise localised external kink modes.

For typical JET plasma shapes, a finite current density is needed at the edge to provide access to the second stable regime for ballooning modes. If the required current density is too large, an external kink mode will become unstable before the second stable regime is reached and no stable route to this regime exists.

This poster described the MHD stability properties of JET high performance hot-ion H-mode discharges and high beta poloidal discharges as a function of the edge pressure gradient and the current density at the edge and the possible access to the second stable regime.

The CASTOR [2] code is used for the MHD stability calculation in toroidal geometry. The HELENA [3] equilibrium code linked to the JETTO [4] and TRANSP [5] transport codes is used for the equilibrium data.

KINK AND BALLOONING STABILITY LIMITS IN A CIRCULAR PLASMA

The growth rate of the low-n external kink mode mainly depends on the current density profile locally at the edge of the plasma. The calculated growth rate of the external kink mode in a circular plasma with toroidal mode numbers, n = 1, 2 and 3 as a function of the edge current density is shown in **Fig.1**. However, the pressure gradient in the region of the localisation of the kink mode has a strong influence on the stability of the kink mode.

Fig.2 shows the dependence of the growth rate of the external kink mode on the edge pressure gradient for n = 1 to 4. A small edge pressure gradient is actually stabilising the kink mode. This is most pronounced for the lowest toroidal mode numbers. Edge pressure gradients close to and beyond the ballooning stability limit are destabilising for the n>1 kink modes. The higher n modes can be more localised in the region of bad curvature on the outside of the plasma.

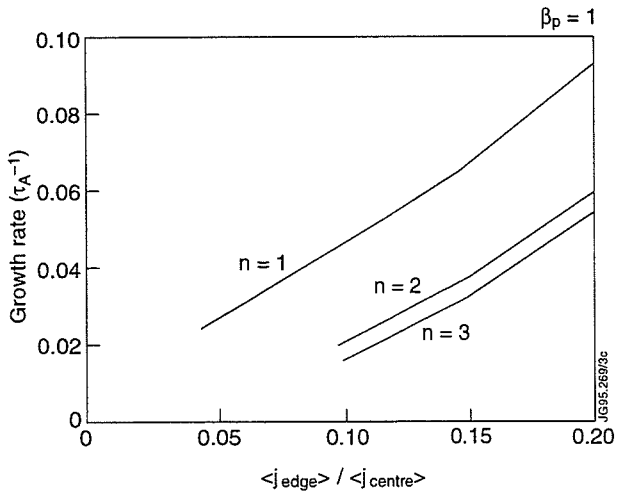

Fig.1 The growth rate of the n=1, 2, and 3 external kink mode as a function of the edge current density for a circular plasma, (a/R=0.3, β_p = 1.).

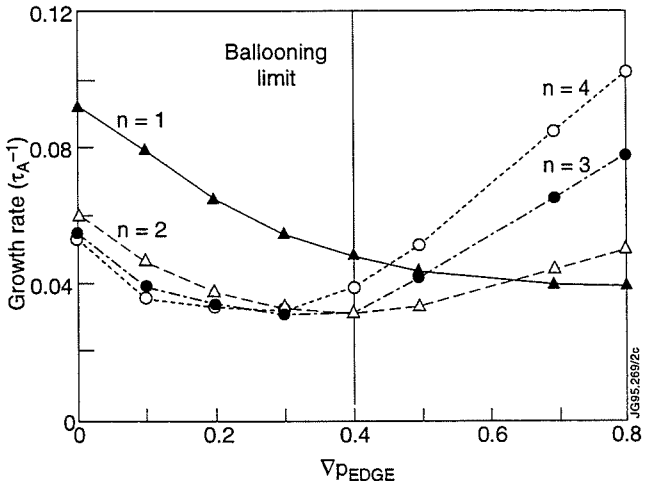

Fig.2 The growth rate of the n=1..4 external kink mode as a function of the edge pressure gradient. The ballooning limit at the plasma edge is indicated.

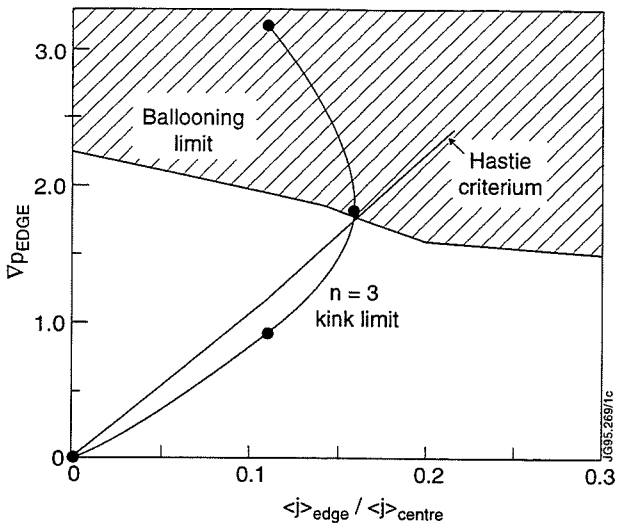

Fig.3 *Calculated stability diagram for ballooning and external kink modes for a circular plasma (a/R=0.3, β_p = 1.).*

MHD STABILITY OF JET HOT-ION H-MODE DISCHARGES

In many of the JET High performance discharges the maximum neutron rate is limited by a so-called slow roll-over. Other causes for a limitation of the neutron rate are giant ELMs and sawteeth and combinations of these modes. The occurrence of this slow roll-over is well correlated with the appearance of low frequency low amplitude MHD activity (8 - 10 kHz). The magnetics show a toroidal mode number *n = 1* and poloidal mode numbers *m = 4 - 6*. **Fig.4** shows the traces of a high performance discharge which is limited by a slow roll-over.

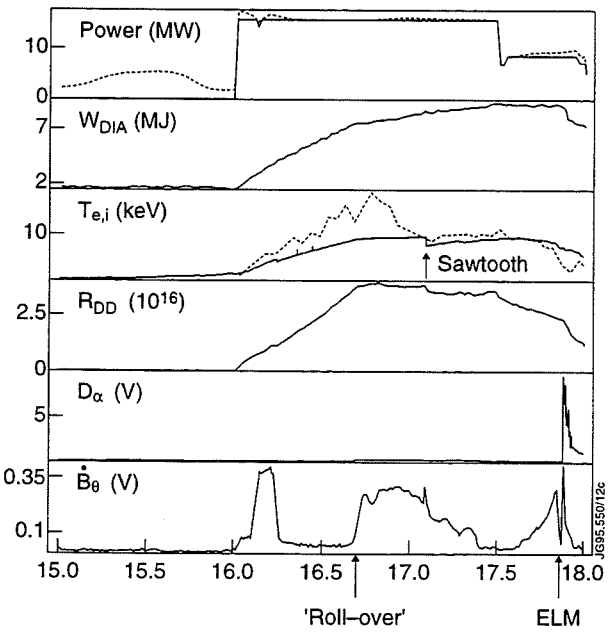

Fig. 4 *Time traces of JET Hot ion H-mode discharge #33558, and the poloidal cross section of the equilibrium.*

The current profile evolution of this discharge is modelled with the JETTO [4] transport code. The experimental density and temperature profiles are used in the calculation. The resulting current profiles for several times are shown in **Fig. 5**.

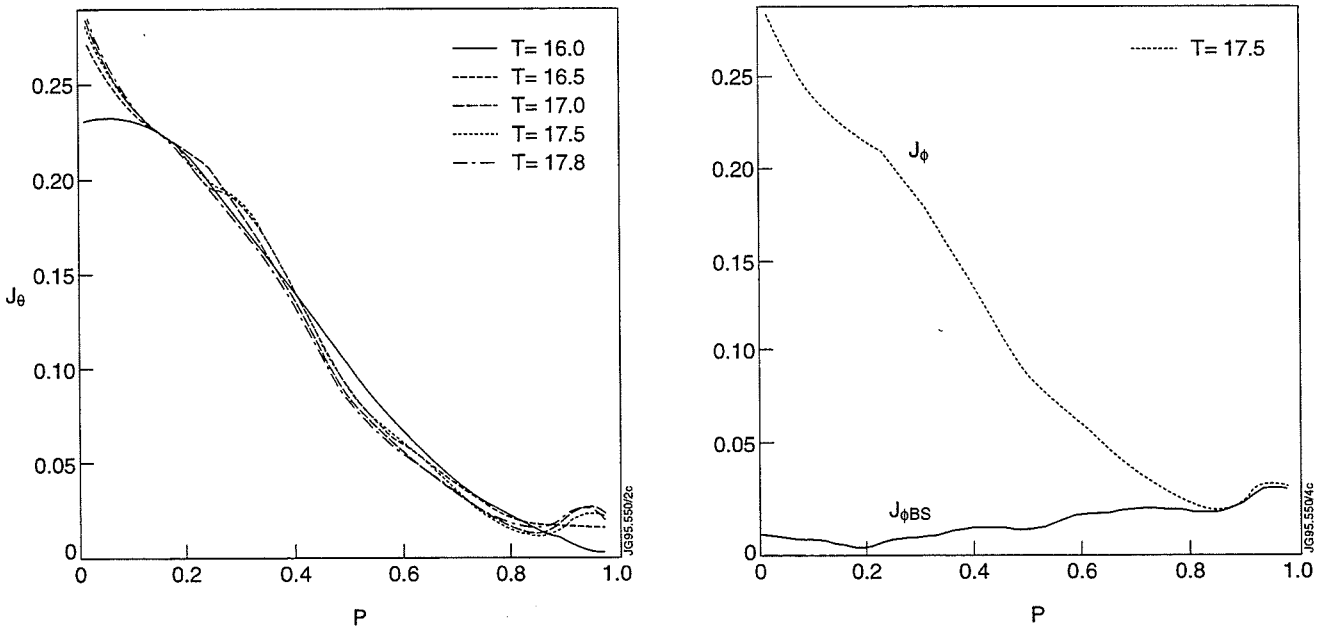

Fig.5 *The current density profile for several times (from the JETTO code) for discharge #33558.*

The MHD stability boundaries to kink and ballooning modes are calculated at t=17.5s by varying the edge pressure gradient and the edge current around the values of the equilibrium at t=17.5s. The results (see **Fig.6**) show that the violation of the kink limit is well correlated with the onset of the observed MHD activity (slow roll-over).

Notice that there is no access to a second stable regime to ballooning modes for this discharge. This is due to the low triangularity and the moderate value of the poloidal beta. The edge current required for access to this regime is too large. An external kink will be unstable at this value of the edge current.

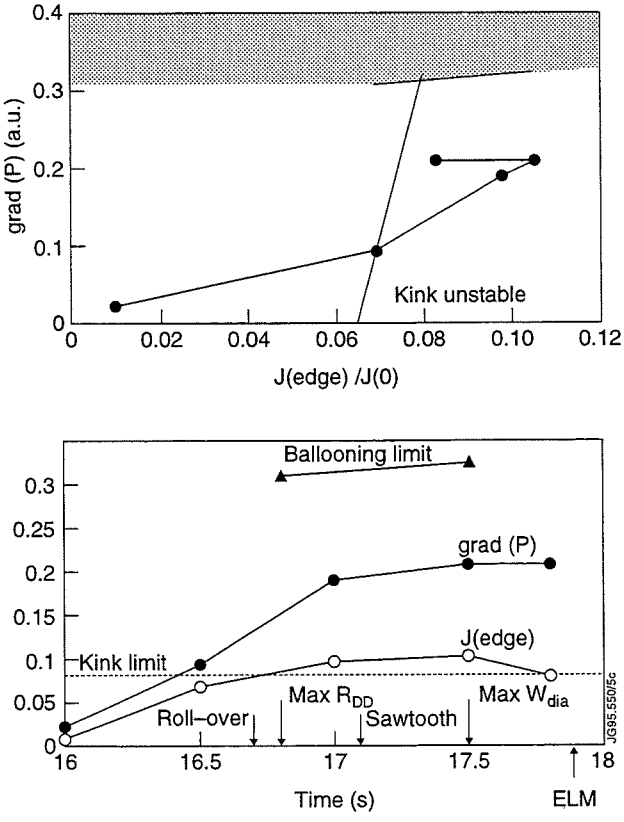

Fig.6 *The MHD stability boundaries of discharge #33558 including the time trace of the experimental values of the edge pressure gradient and edge current.*

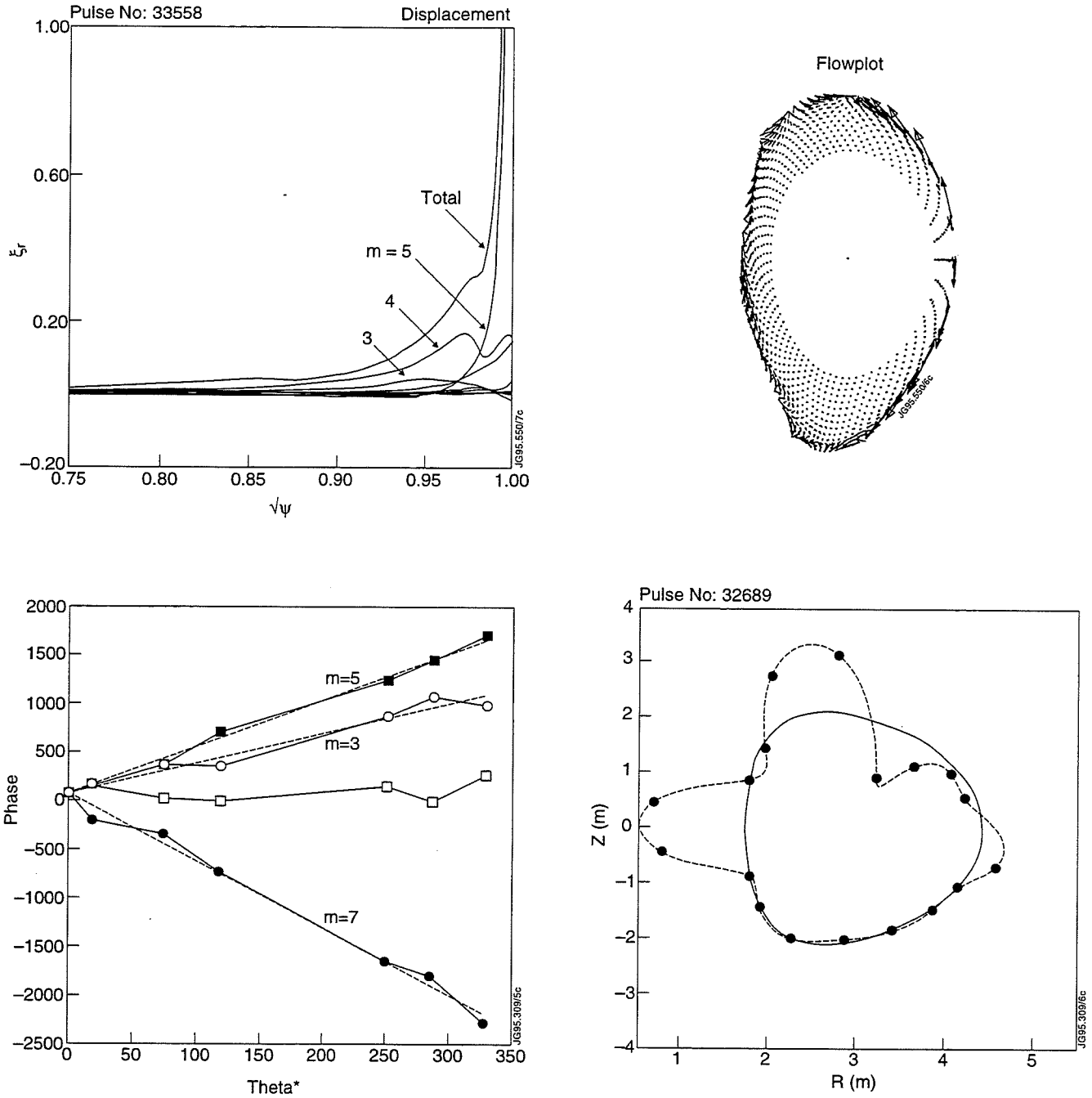

Fig.7 *The mode structure of the n=1 external kink mode as calculated and from observations from SXR data and magnetics.*

The experimental pressure gradient at the plasma edge in these Hot-Ion H-modes is typically close to the ballooning limit. The central pressure gradient is however well below the ballooning limit. Fig. 8 shows the correlation of the experimental edge pressure gradient and the calculated pressure gradient which is marginally stable to ballooning modes.

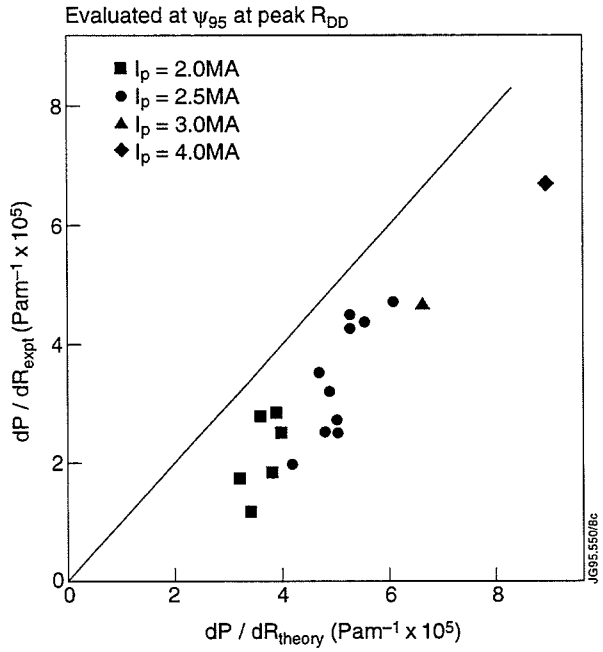

Fig.8a *Comparison of the experimental pressure gradient and the calculated pressure gradient which marginally stable to ballooning modes.*

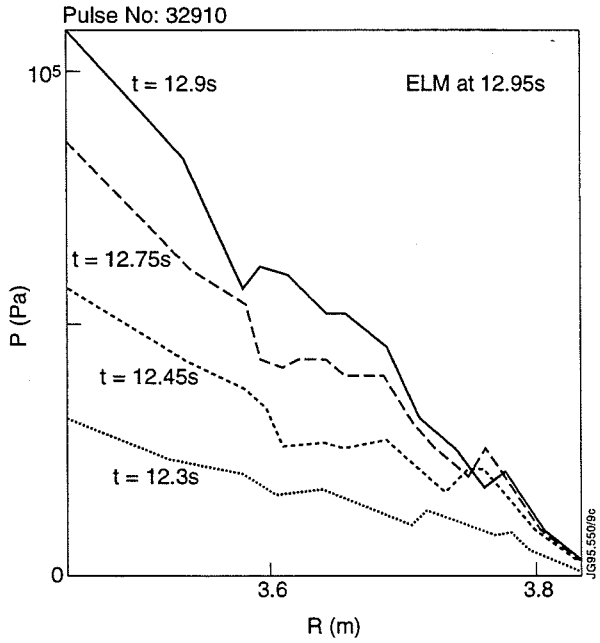

Fig 8b *The time evolution of the pressure profile. The edge pressure gradient appears to be limited at the ballooning limit well before the occurrence of the ELM*

At full toroidal field (3.4 T) and I_p~3MA, the hot ion H-mode discharges reach a normalised beta, $\beta_N = <\beta> / (I / a B)$ of around 2. This limit is set by local edge instabilities and sawteeth. At lower current much higher values of β_N can be reached in which the ballooning limit is reached over most of the plasma volume and the plasma is marginally stable to an n=1 external kink. **(See Fig. 9)**

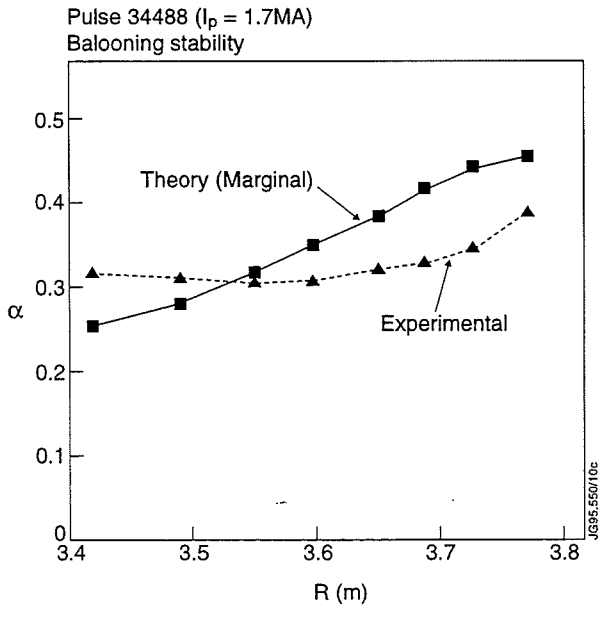

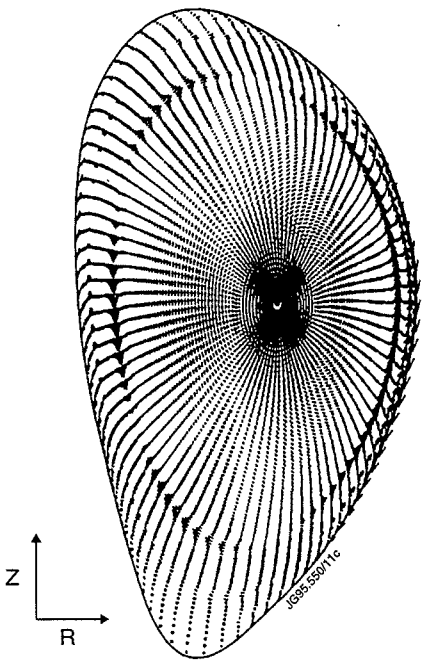

Fig. 9 *The stability analysis of ballooning and kink modes for Hot-ion H-mode discharge #34488 (I_p = 1.7 MA).*

MHD STABILITY OF JET HIGH BETA POLOIDAL DISCHARGES

Transiently improved confinement has been observed in some JET high β_{pol} discharges [6]. This has been correlated with current ramps or oscillations in the total current.

The time evolution of two high beta poloidal discharges is shown in **Fig. 10**. The two discharges are identical except for a small current ramp in one of them. This ramp leads to a significant increase in the total stored energy at constant input power. At the same time the edge electron temperature gradient is increasing. The improved confinement regime is lost at the end of the ramp up when the total current is decreasing. Notice that small ELMs are still present in the phase of improved confinement.

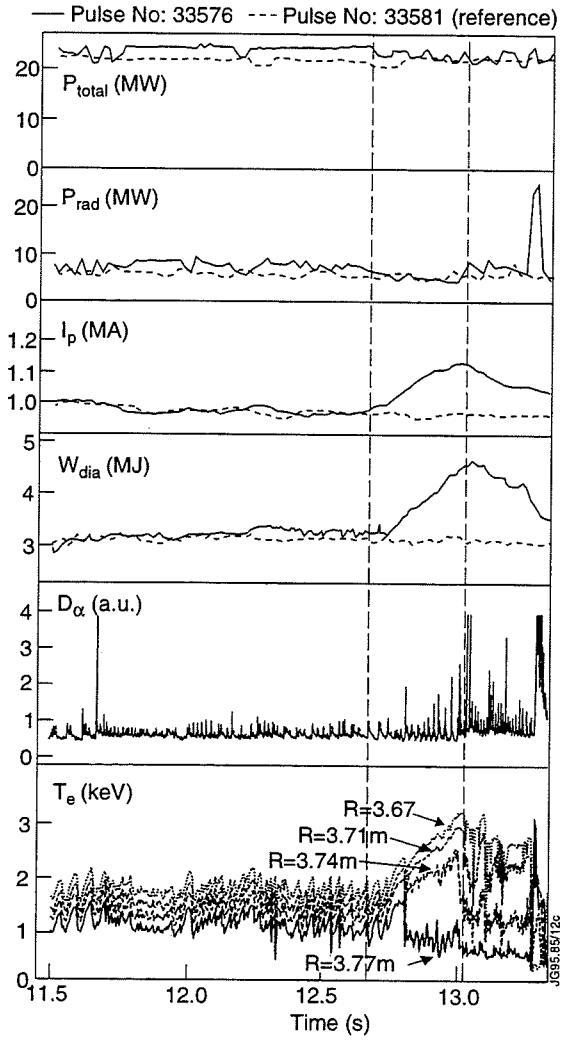

Fig.10 *Improved confinement regime in high beta poloidal plasmas with a current ramp.*

Discharge #32344 is another example of this improved confinement (see **Fig. 11**). The current profile evolution of this discharge was analysed with the TRANSP [5] code. The time evolution of the current profile is plotted in **Fig.12.**

Due to the high value of β_{pol} (>2.5) and the inherent high value of the triangularity only a small edge current is required to bring the plasma edge from ψ = 0.95 to 1.0 into the second stable region with respect to ballooning modes. The value of the current density at which ψ=0.95 becomes stable is indicated in **Fig. 11a**. The time at which the experimental edge current exceeds this value correlates well with the observed improved confinement and increasing edge gradients.

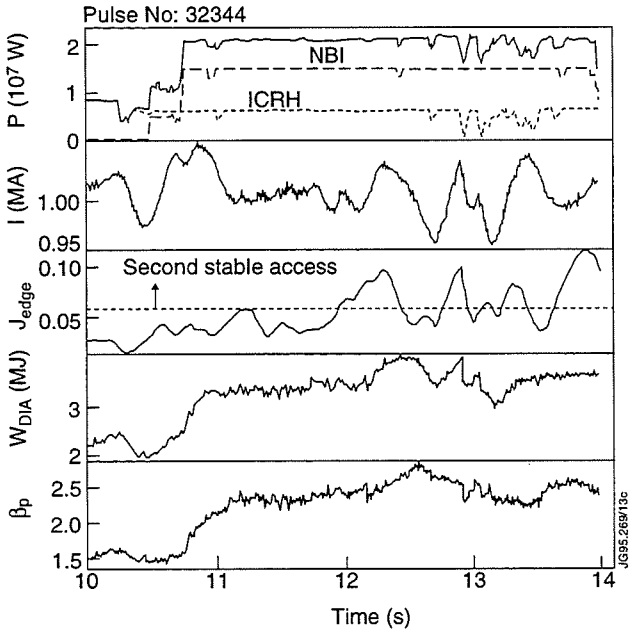

Fig.11a Traces of the total heating power, total current, edge current density (from TRANSP), the total stored energy and poloidal beta for discharge #32344.

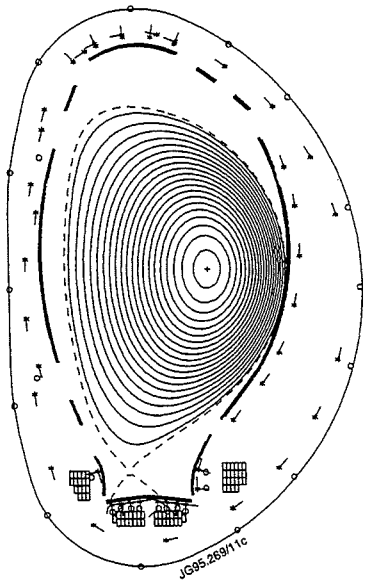

Fig. 11b The plasma shape at high poloidal beta.

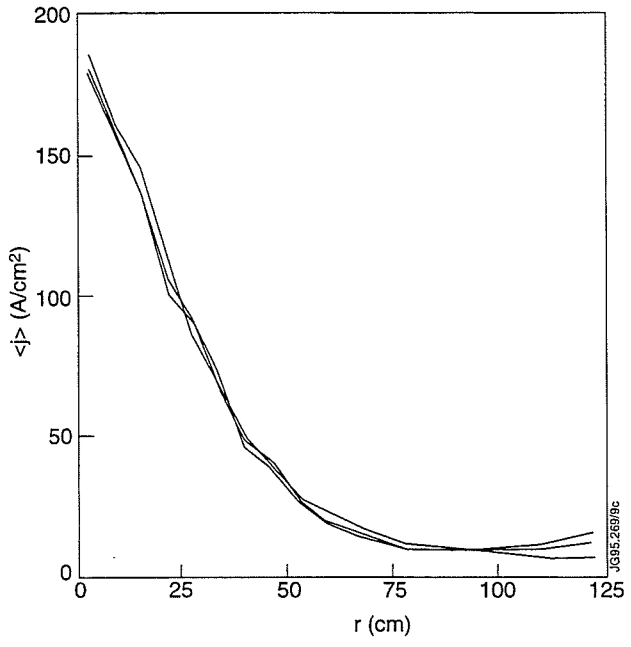

Fig.12 The evolution of the current profile during the oscillation in the total current (from TRANSP) at t=11.75 s, t=12.0s and t=12.25s.

Results of the *n = 1* external kink stability calculation are shown in **Fig.13** together with the ballooning stability curve. The *n = 1* and *n = 2* kinks are very stable in this configuration. An open gap does exist between the ballooning and the kink stability curves giving access to a region where large pressure gradients and the associated edge currents are stable.

The experimental path the discharge follows in the grad(P)- J_{edge} plane is indicated in **Fig.13**. Before the ramp of the current the pressure gradients at the edge are calculated to be marginally stable to ballooning modes.

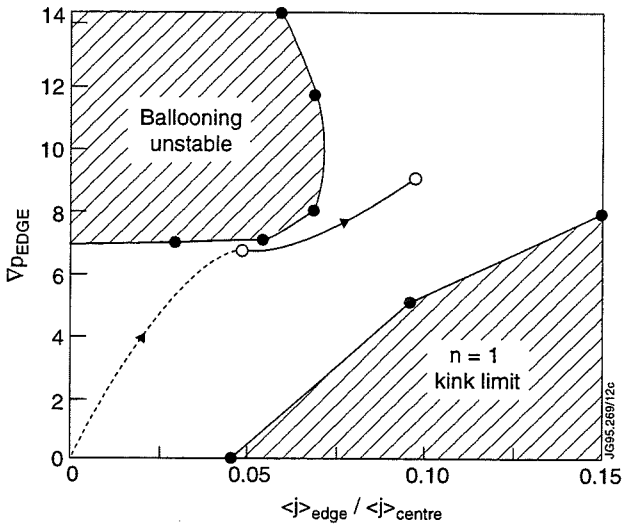

Fig. 13 *Stability diagram for high beta poloidal discharge #32344 at t=12.25s.*

CONCLUSIONS

- The local MHD stability properties at the plasma edge can be described by the ballooning and low-n external kink stability limits in the plane of the edge pressure gradient and the edge current density.

- The low-n external kink mode are destabilised by the edge current density. A small edge pressure gradient is stabilising the external kink especially the n=1 mode. For values of the pressure gradient close to the ballooning limit the pressure gradient is destabilising mostly for n>1 modes.

- The values of the edge current density in Hot ion H-mode discharges due to bootstrap current (and Ohmic current through the high edge temperature) are large enough to drive low-n external kink modes unstable. This suggest that the MHD activity observed during the slow roll-over is due to external kink modes saturated at small amplitude. Even at this small amplitude, the modes have a large effect on the confinement properties.

- At the relatively low values of triangularity and moderate values of beta poloidal in the JET hot-ion H-mode discharges, there is no stable route to access the second stable regime to ballooning modes. The amount of edge current required for access to this regime would drive an external kink mode unstable.

- The observed improved confinement phases in JET high beta poloidal discharges induced by small current ramps agree well with the stability calculations of ballooning and kink modes and the predicted access to the second stable regime for ballooning modes.

REFERENCES

[1] P. Smeulders et al., Proceedings 22nd EPS Conference on Controlled Fusion and Plasma Physics, Bournemouth 1995.

[2] W. Kerner et al., Proc. 18th Eur. Conf. on Contr. Fusion and Plasma Physics, Berlin (1991), IV, p.89.

Highly Radiative Discharges with Seeded and Intrinsic Impurities in JET

H J Jäckel, D Campbell, S Clement, M von Hellermann, L D Horton, A Loarte, G F Matthews, R Reichle, M Stamp, G Vlases.
JET Joint Undertaking, Abingdon, Oxfordshire, OX14 3EA, UK.

INTRODUCTION

The conductive power into the divertor in high performance X-point discharges can quickly lead to overheating of the divertor target, with the effect of excessive release of target material. For a standard JET X-point configuration, a target load of 10 MW for 10 seconds on a graphite target would result in a temperature increase of about 2000 °C. In future bigger machines, like ITER, measures have to be developed, to efficiently reduce the target load.

JET has been operated with two different target materials, CFC (= fibre reinforced graphite) and Beryllium. Excessive target load is particularly detrimental in the case of Beryllium with its relatively low melting point [1].

Several methods have been employed at JET to limit or mitigate the temperature rise, aiming at either increasing the wetted area on the target or reducing the total target load [2]:

- **Increase of the wetted area:** Horizontal sweeping of the strike points across the target has been used in JET [3], as well as widening the scrape-off layer (SOL) footprint on the target ('flux expansion'). Sweeping, in particular, is very effective, however, it requires a more open divertor design with the probably adverse effect of higher neutral particle leakage.

- **Reduction of the target power load:** This can be achieved by increasing the isotropic power losses, radiation or CX-loss. Deuterium puffing as well as seeding of recycling impurities (nitrogen, neon and argon) has been used in JET, resulting in strong reduction

and eventually in extinction ('detachment') of the conductive power to the target, while the peak divertor radiation moves towards the X-point [4,5].

In the following, the effect of impurity seeding and deuterium puffing on the plasma performance in discharges with high power additional heating will be discussed. The obvious objective of these experiments is to increasing the isotropic losses in the divertor and the SOL, without affecting the bulk plasma too much. If impurity seeding is to be a viable option for ITER to reduce effectively the target load, the dilution and contamination of the main plasma must be kept at a low level ($Z_{eff} \leq 1.6$).

EXPERIMENTAL ARRANGEMENT

The three gases, nitrogen, neon and argon have been used in the 1994/95 experimental campaign to increase radiation losses. The gases were seeded via the gas introduction modules on top, at the mid plane and in the divertor region of the machine and in most cases in conjunction with deuterium fuelling. The input power typically ranged from 8-16 MW for pure NBI-heating and up to 27 MW for combined RF/NBI. The high power heating phase lasted typically 4-7 s, but could be stretched to over 10 s at strong puffing, which virtually meant steady state conditions. The maximum puff rates (in atoms/s) for the individual species were; N_2 : $5 \cdot 10^{21}$ s^{-1}, Ne: $2.5 \cdot 10^{21}$ s^{-1}, Ar: $3 \cdot 10^{20}$ s^{-1} and D_2 : $4.5 \cdot 10^{22}$ s^{-1}. The experiments were carried out in a standard single null (SN) configuration with the X-point at the bottom of the cross section. The achieved H-mode confinement in this configuration, expressed in the improvement over the ITER89-P L-mode scaling, is about 2 with no impurity seeding or fuelling.

EXPERIMENTAL FINDINGS

With impurity seeding as well as with deuterium fuelling, a deterioration of energy and particle confinement with increasing puff rate is observed. However, while impurity seeding resulted in radiation loss of up to 80% of the input power, only about 50% could be achieved with pure deuterium puffing.

I. IMPURITY SEEDING

Comparison N_2-puffing versus N_2 + D_2-puffing

The unavoidable contamination of the bulk plasma with increasing seeding rate lead to a loss of energy confinement as well as of particle confinement. Figure 1 shows some global plasma parameters of 3 discharges with nearly identical heating power, with combined D_2 + N_2 - puffing, with N_2 - puffing only (D_2 : $\approx 1.5 \cdot 10^{22}$ s^{-1}, N_2 : $2-2.5 \cdot 10^{22}$ s^{-1}) and the unseeded target discharge. There is an obvious loss of energy confinement of the seeded discharges, as seen in the decay of the H-factor and, likewise, a drop in the particle confinement, indicated by the drop of the electron density for the purely N_2.- seeded discharge.

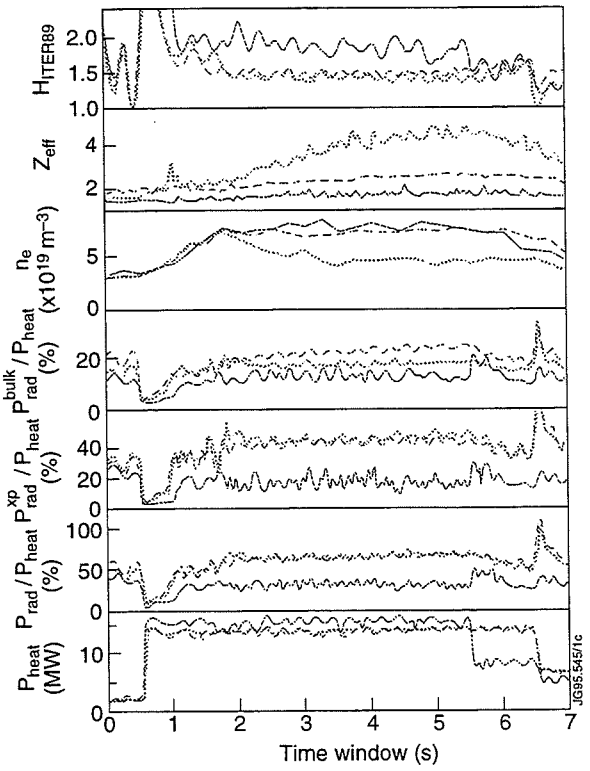

Fig. 1: *Comparison of two N_2- seeded discharges, (dotted: N_2; dashed: N_2+D_2) with the unseeded target discharge (solid). The seeding starts at about 1 s (relative time scale). The seeded discharges both have a radiation loss of about 65%. Without additional D_2- puffing, n_e drops significantly and Z_{eff} rises strongly. The energy confinement for the two seeded discharges is about the same, at $H_{ITER89P} \approx 1.5$, compared to $H_{ITER89P} \approx 2$ for the unseeded discharge.*

The high Z_{eff} of this discharge is mainly due to the drop in density. The total number of N_2 - ions is about the same, as a rough estimate on the basis of the increase of Z_{eff} implies. Figure 2 shows for the N_2 - and the N_2 + D_2 - seeded discharges the development of $\Delta Z_{eff} \cdot N_e$ (N_e = total number of bulk electrons), as a measure for the total number of impurity electrons in the bulk plasma.

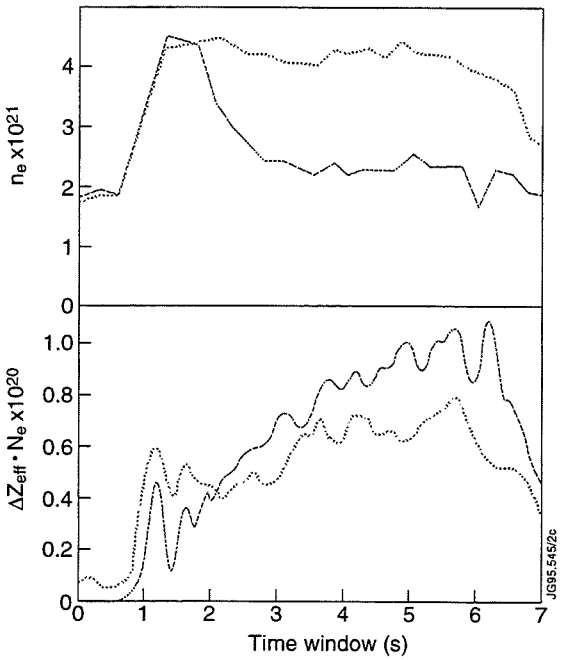

Fig. 2: *The total number of impurity electrons in the bulk plasma (bottom) is similar for the two discharges of fig. 1 (solid: N_2; dotted: N_2+D_2), although the total number of electrons in the bulk plasma differs significantly (top)*

Comparison N_2 -, Ne-, Ar-seeding

Multi-shot analysis

The conductive power, P_{targ}, dumped on the divertor target is given by

$$P_{targ} = P_{heat} - P_{rad} - P_{CX} - \dot{W} \tag{1}$$

were P_{rad} can be split into the radiation loss inside the seperatrix and in the divertor (X-point) radiation loss,

$$P_{rad} = P_{rad}^{bulk} + P_{rad}^{xp} \tag{2}$$

The impurity seeding causes an increase in P_{rad} and a reduction of P_{targ}, but has detrimental effects on the confinement and dilution of the bulk plasma, as the radiation is not purely confined in the divertor. For the different series of seeding experiments, the evolution of some essential global plasma parameter with increasing P_{rad} is portrayed in the following three figures. To account for fairly wide range of plasma parameters, mainly normalised quantities has been chosen.

The figures 3, 4 and 5 show the N_2 -, Ne- and Ar - seeding series, respectively. With increasing P_{rad}/P_{heat} not only P_{rad}^{xp} rises, but also P_{rad}^{bulk}, however, for the different impurities with different rates, growing from $N_2 \rightarrow$ Ne $\rightarrow$ Ar. At the same time the energy confinement drops. At the highest radiation levels of about 80% of P_{heat}, divertor detachment has been frequently observed, indicated by the beginning annihilation of I_{sat} of Langmuir probes, built into the divertor target.

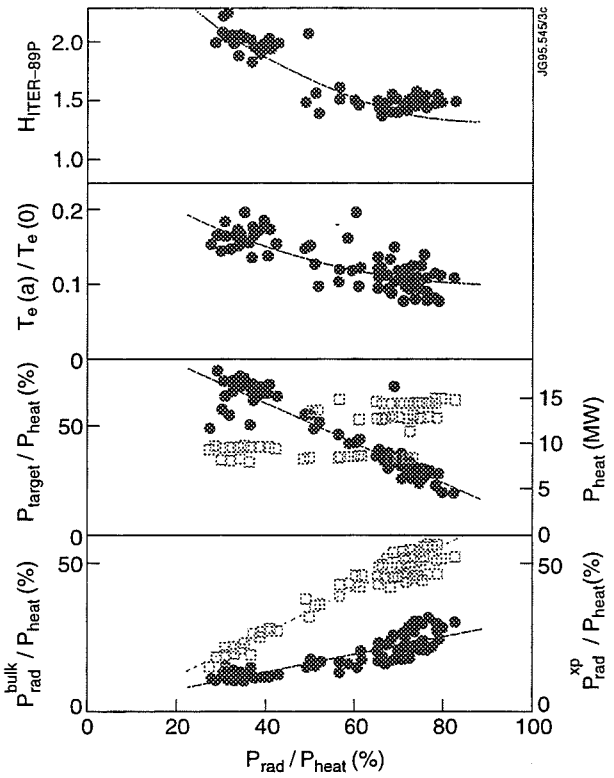

Fig. 3: *Nitrogen seeding*

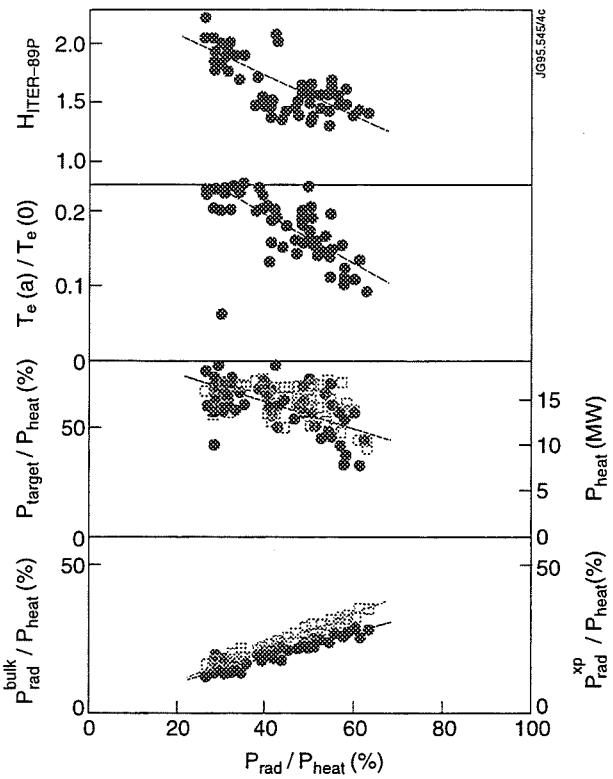

Fig. 4: *Neon seeding*

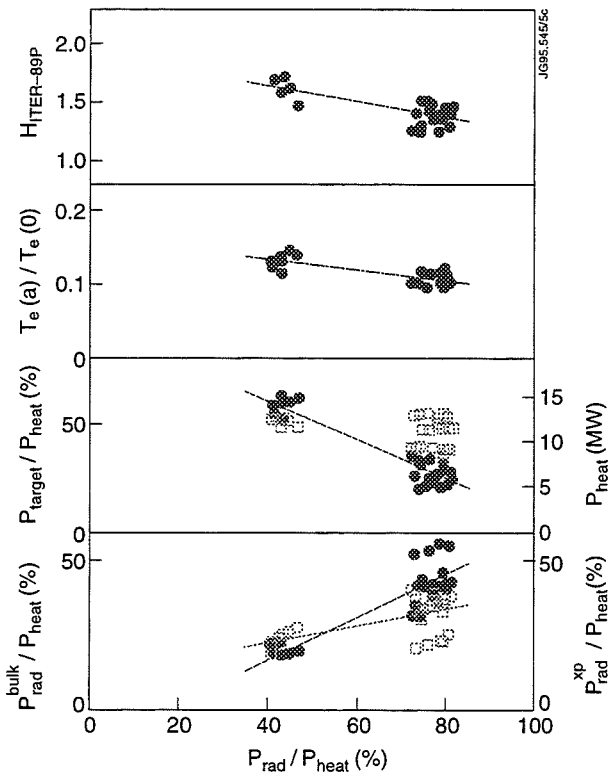

Fig. 5: *Argon seeding*

Fig. 3-5: *Effect of the impurity seeding on global plasma parameters, plotted as a function of P_{rad} /P_{heat} . Both, bulk and X-point radiation rise (bottom) and the target load is reduced at the same rate (2^{nd} box from bottom). The edge electron temperature drops as does the confinement (full symbols refer to the left scale, open ones to the right).*

The highest value of Z_{eff} is observed with the Ne-seeding, although only 60% radiation power has been achieved. Figure 6 shows, versus Z_{eff}, $P_{rad}^{bulk} / \int n_e dl$ as a measure for the cooling power per electron. Ar- as well as N_2 - seeding allow high radiation losses of about 80%, but there is no clear favourite; argon achieves a $Z_{eff} < 2$ but produces high P_{rad}^{bulk}, whereas in the case of N_2, P_{rad}^{bulk} grows just moderately, but $Z_{eff} \leq 3$.

N_2-seeding experiments were carried out with both target materials, Carbon and Beryllium. No significant difference has been observed. Figure 7 shows the evolution of the radiation losses, the target load and the confinement for two N_2 - seeding series, one carried out with CFC-target, the other with Be-target.

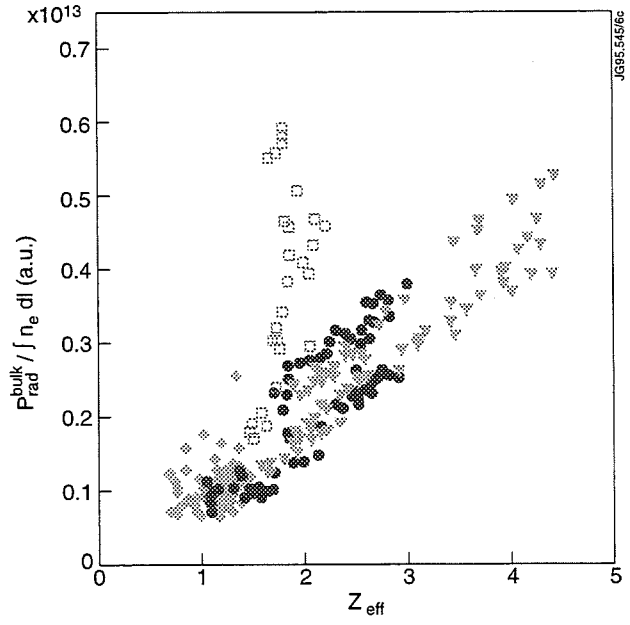

Fig. 6: Density normalised bulk radiation, as a measure for the cooling rate per electron, versus Z_{eff}. Both, Ar- (□) and N_2-seeding (●) reach 80% radiation loss, but at different Z_{eff} and bulk plasma cooling rate, respectively. Ne-seeding (▼) produces the highest Z_{eff}. For comparison: ◆= pure deuterium puffing .

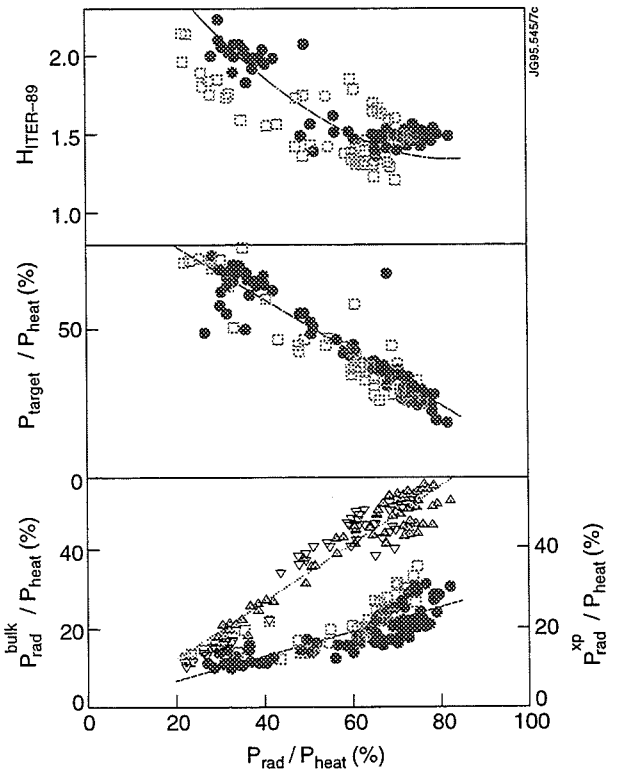

Fig. 7: Development of the bulk and X-point radiation, target load and confinement with increasing ratio of P_{heat}/P_{rad} for N_2 - seeded discharges with the CFC-target (full symbols) and the Be-target (open symbols).

Bulk plasma emissivity

Abel-inverted profiles, derived from bolometric measurements, and taken at similar electron density and temperature profiles, show radiation shells, which, for N_2 are narrow, peaking close to the seperatrix, but are wider in the case of Ne-seeding (fig. 8). No adequate data are available for Ar, where only a few discharges have been carried out.

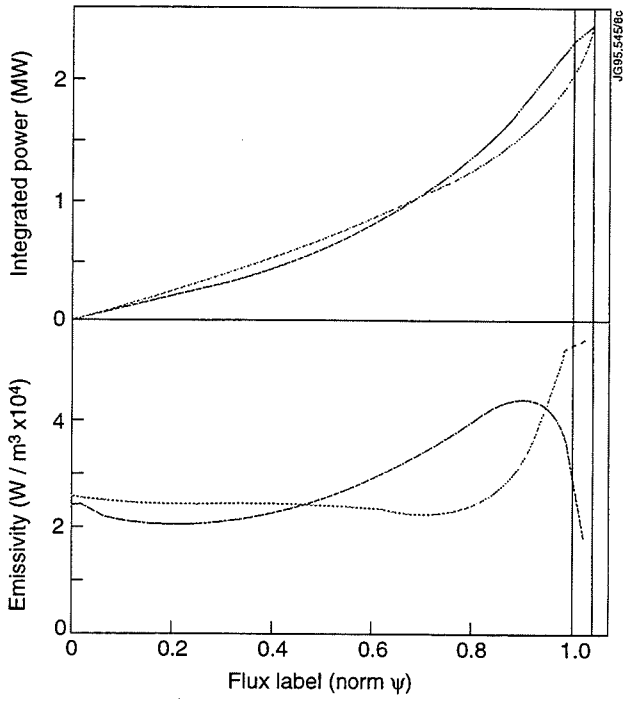

Fig. 8: *The radial emissivity profiles (bottom), derived from bolometer measurements, show a narrow radiation shell close to the separatrix (Ψ=1) for N_2 - seeding (dotted), but a much wider distribution for Ne-seeding (solid) at the same total bulk radiation (top).*

II. DEUTERIUM PUFFING

Multi-shot analysis

A series of experiments were carried out with strong D_2 - puffing only, up to $4.5 \cdot 10^{22}$ s^{-1}, with the intention to mainly increase the divertor density and hence the local radiation of the intrinsic impurities (target material: C or Be). However, even at the highest puff rate the total radiation loss did not exceed 50%, indicating, that radiation of intrinsic impurities (C, Be) play only a minor role, whereas the confinement degraded strongly (fig. 9). The gas puff was applied in the main chamber and/or in the divertor, but no essential difference for the different puffing locations is observed.

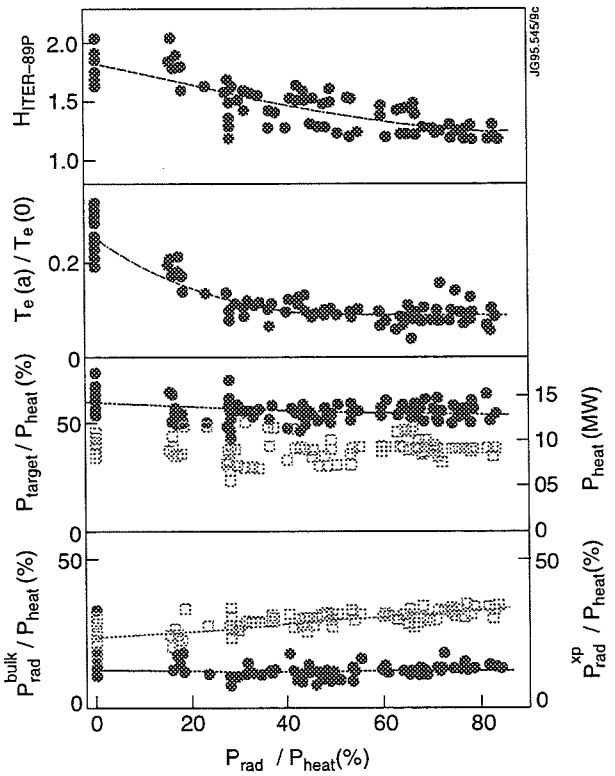

Fig. 9: *Deuterium fuelling results in a strong degradation of the confinement at higher puff rates. $H_{ITER89P}$ (top box) and the edge electron temperature (2^{nd} from top) drop strongly with increasing puff rate, while the radiation losses, P_{rad}^{bulk} and P_{rad}^{xp} (bottom), rise only marginally.*

The 'missing power'

The strong deterioration of the confinement suggests the idea, that there is an additional loss term, which is not accounted for by the bolometric measurement. This can be the CX-term in equation (1), as it is only partly measured by the bolometry, namely in regions not hidden behind plasma.

An attempt has been made to roughly estimate the CX-loss. On the basis of a 1-dimensional model, which neglects lateral heat diffusion, the target temperature can be calculated

$$T_{targ} \propto \sqrt{P'_{targ}} \tag{3}$$

P'_{targ} is the target power per unit area and is a function of the poloidal position. Using P_{targ} from the power balance of equation (1) in (3), we can calculate an average T_{targ}. Matching the peak value of this temperature with the measured one, allows to estimate the wetted area on the target. Figure 10 shows the maximum measured temperature (top, solid line) and the calculated one (top, dashed) for an unfuelled discharge.

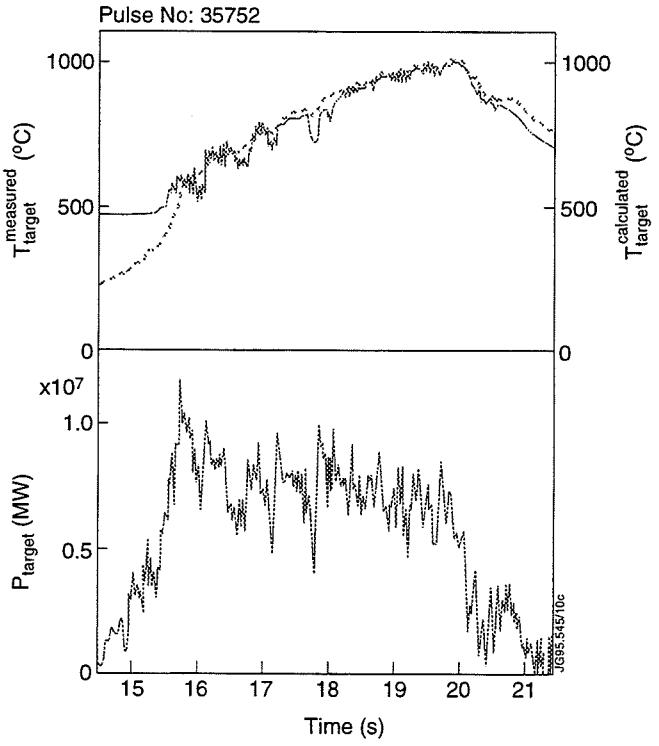

Fig. 10: *The measured target temperature (top box, solid) can be fairly well simulated with a 1-D caculation, following equation (3) with the target load of the power balance (bottom, solid) of equation (1).*

If the estimated wetted area is used to calculate T_{targ} for a similar, but fuelled discharge ($P_{heat} \approx 11$ MW; $\Gamma_D = 2.5 \times 10^{22}$ s^{-1}), the measured temperature is significantly exceeded. Figure 11 shows, that P_{targ} has to be reduced by about 3 MW to P_{targ}^{sim} (bottom), to match the measured temperature (top).

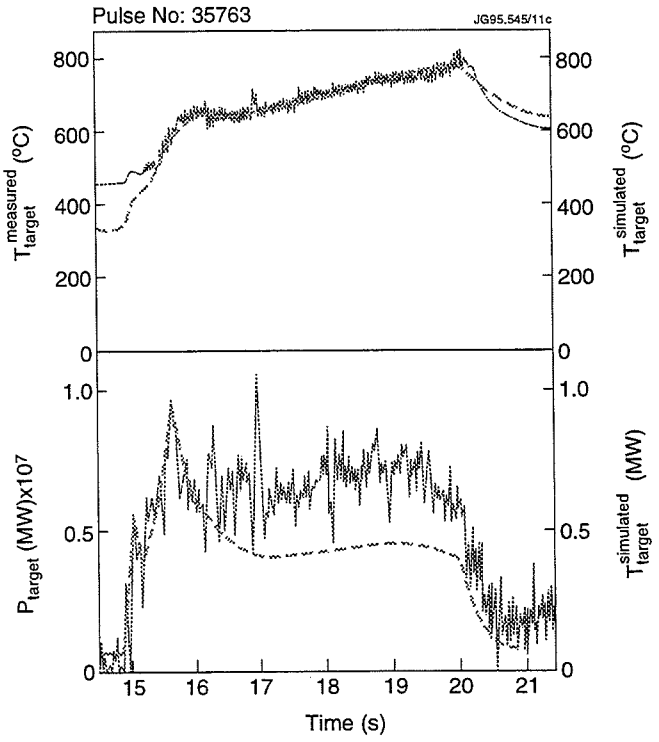

Fig. 11: *If strong deuterium fuelling is applied, the calculated target temperature exceeds the measured one (top, solid) significantly. P_{targ} (bottom, solid) has to be reduced to P_{targ}^{sim} (bottom, dashed), to match the measured temperature (b).*

The difference $P_{targ} - P_{targ}^{sim}$ might be attributed to non-measurable CX-losses. This would constitute a significant energy loss of the ions, in contrast to impurity seeding, which effects the electron energy.

The strike point positions for the two compared discharges were stationary within about 5 mm over the relevant time interval and the temperature profiles were of similar width.

CONCLUSIONS

I. Impurity seeding

- Nitrogen, neon and argon have been used as seeding impurities, in conjunction with deuterium, in discharges with up to 27 MW heating power
- Radiation losses of up to 80% of the input power have been achieved with an H-factor of $H_{ITER89P} \approx 1.5$ with combined $N_2 + D_2$ - puffing
- The energy and particle confinement decays significantly with increasing puff rate, as well as the edge electron temperature
- The ratio $P_{rad}^{bulk}/P_{rad}^{targ}$ becomes less favourable with increasing Z of the seeded gas in the sequence $N_2 \rightarrow Ne \rightarrow Ar$. However, while P_{rad}^{bulk} was lowest with N_2 - seeding, Z_{eff} was $\leq$ 3. The lowest Z_{eff} was observed with Ar ($Z_{eff} \leq 2.$), the highest with Ne ($Z_{eff} \leq 4.5.$).
- The radiation shell is narrow and close to the separatrix for N_2, wider and further inward for Ne. No clear statement can be made for Ar as yet (only few discharges carried out), because n_e- and T_e-profiles differ from the N_2 - and Ne-experiments. However, there are indications for similarities to the N_2 - case.
- No significant difference of the radiation pattern and confinement in N_2-seeding experiments is observed with the two different divertor target materials (Be / C).

II. Deuterium puffing

- The maximum applied D_2 - fuelling rate was $4.5 \cdot 10^{22}$ s^{-1}.
- The confinement degrades strongly with increasing fuelling to eventually $H_{ITER89P} \approx 1.2$
- The radiation loss increase only slightly with increasing fuelling rate, from 35% for no fuelling to about 50% of the heating power at the maximum puff rate..
- Target temperature simulations suggest sizeable CX-losses.

References

[1] B.J.D. Tubbing et al. Proc. 22th EPS Conf. Contr. Fus. & Plasma Phys., Vol. 19C/III (1995) 453

[2] D. Stork et al. Proc. 22th EPS Conf. Contr. Fus. & Plasma Phys.., Vol. 19C/II (1995) 125

[3] M. Keilhacker & JET Team (1995), to be published in Plasma Phys. and Contr. Fusion

[4] R. Reichle et al., Proc. 22th EPS Conf. Contr. Fus. & Plasma Phys., Vol.19C/III (1995) 85

[5] G.F. Matthews, J. Nucl. Mater. 220-222 (1995) 104

Optimization of Neutral Beam Deposition, Configuration and Recycling of Hot-Ion H-Modes in JET

R W T König, K D Lawson[1], K-D Zastrow, P Breger, N Deliyanakis, M G von Hellermann, A Howman, T T C Jones, P J Lomas, A C Maas, F B Marcus, R Sartori, B Schunke, P Smeulders, M F Stamp, P R Thomas

JET Joint Undertaking, Abingdon, Oxfordshire, OX14 3EA, UK.

[1] UKAEA Government Division, Fusion, Culham, Abingdon, Oxon OX14 3DB, UK (UKAEA/EURATOM Fusion Association).

INTRODUCTION

In the 1994/95 experimental campaign the performance of JET with its new Mark I pumped divertor was limited by ELMs and MHD rather than by impurity influxes as in previous operational periods. This demonstrates the good power handling capabilities of the new divertor. The frequent occurrence of ELMs however was in stark contrast to experience from previous JET operational campaigns, in which ELMs could only be induced through strong gas puffing, the use of hydrogen fuel or operation in high beta regimes. The key parameter relating to the MHD stability is believed to be the edge pressure gradient [1,2,3]. Once optimum conditions of stability have been achieved, both density and recycling determine the performance of a discharge. Figs. 1 and 2 detail the connections between the different processes involved.

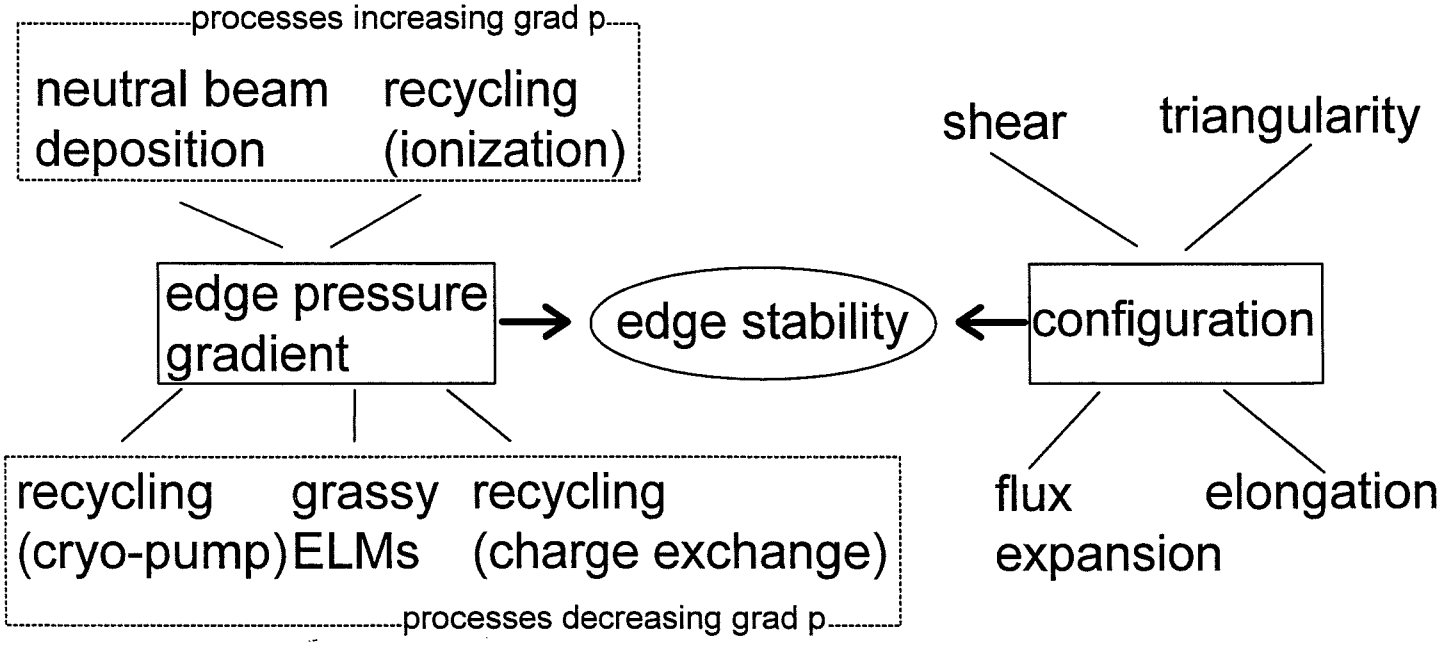

Figure 1

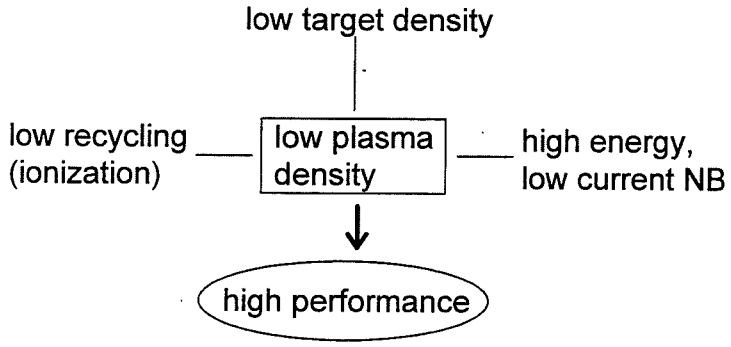

Figure 2

EDGE STABILITY

Magnetic configuration

The stability of the plasma edge against MHD/ELMs can be improved by choosing a magnetic configuration which has a high shear. This is achieved by increasing the plasma triangularity and elongation.

The original 'standard fat' configuration did not provide sufficient stability ($\tau_{ELM\text{-}free}$ < 0.5 s). A highly triangular fat configuration was developed, resulting in a clear improvement. This configuration was limited to plasma currents of 3 MA and tended to disrupt at large ELMs, causing unacceptably large forces on the inner saddle coils. Consequently, a high flux expansion configuration was developed which has a plasma behaviour and performance similar to the PTE discharges and could be used up to 4 MA. Table 1 shows typical parameters for these configurations and figs 3 to 6 show the dependence of the ELM free period on the parameters for a database, including the 30 highest performance discharges.

configuration	shear(at Ψ_{95})	triangularity	flux expansion
standard fat	3	0.17	2
fat triangular	4.5	0.45	5
high flux expansion	4	0.33	4 - 8
'old' single null (1991/2)	4.5	0.45	>10

Table 1

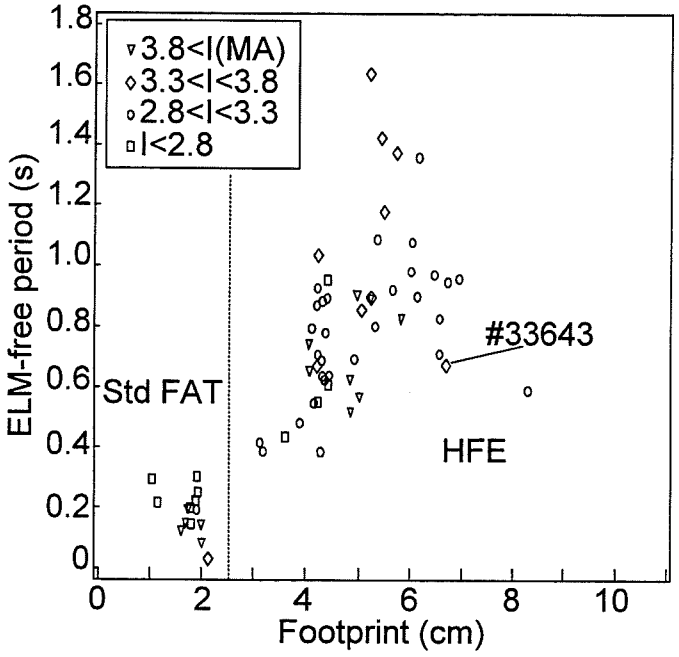

Figure 3: ELM free period vs. footprint on the divertor floor of SOL flux surface 1 cm width at the plasma midplane sorted by plasma current I (MA) (footprint for pulse 26087 ~18 cm)

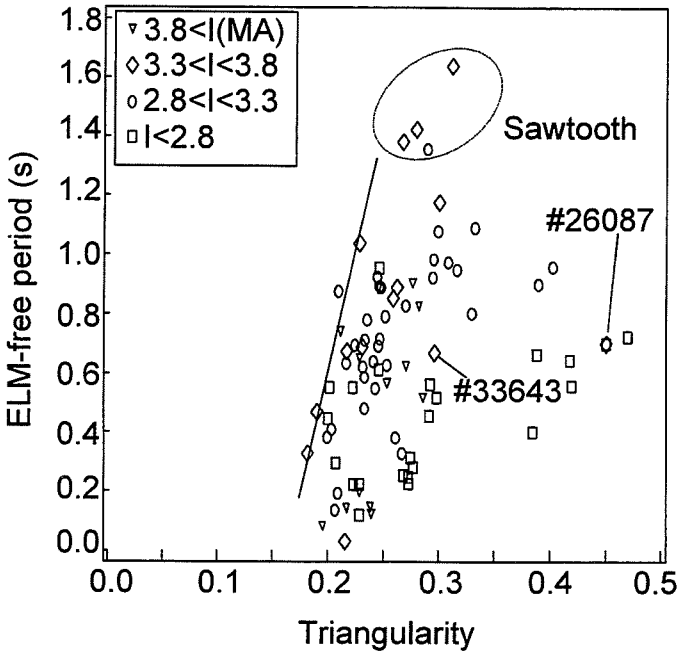

Figure 4: ELM free period vs. triangularity sorted by plasma current I (MA)

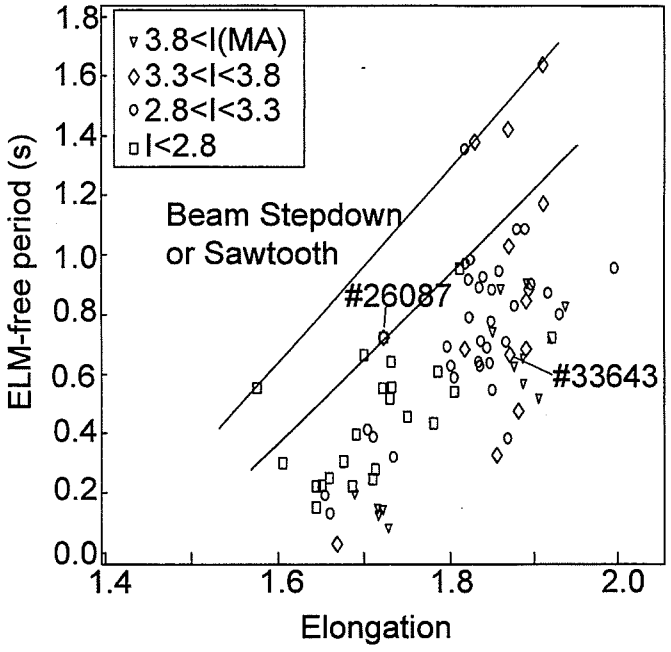

Figure 5: ELM free period vs. elongation sorted by plasma current I (MA)

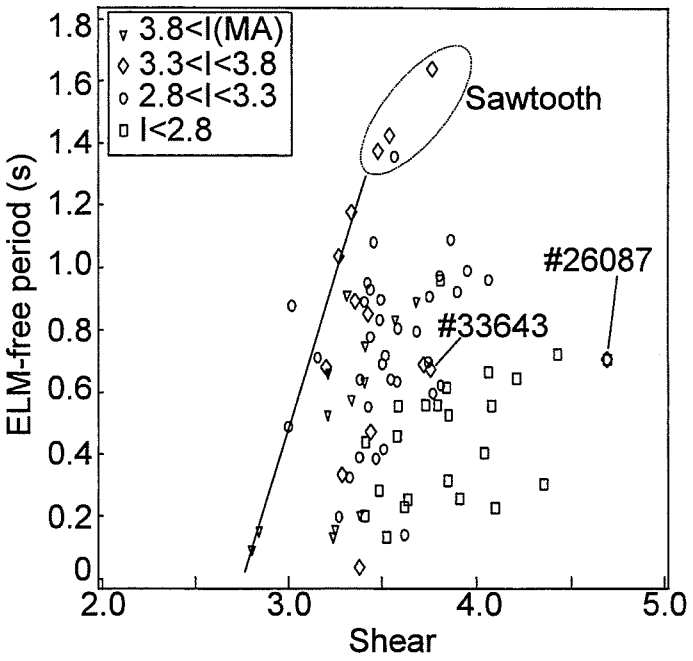

Figure 6: ELM free period vs. shear at 95% flux surface sorted by plasma current I (MA)

Experiments investigating the configuration showed:

- at low shear (S_{95} ~ 3) the plasma remains ELMy regardless of the flux expansion
- at moderate shear (S_{95} <= 4) the ELM frequency decreases with increasing flux expansion
- at high shear (S_{95} >= 4) the ELM-free period gets longer than the typical heating pulse duration
- increasing triangularity and elongation and therefore shear at a constant flux expansion raises the edge stability limit [4].

Edge Pressure Gradient

a) Neutral beam power and particle deposition

The evolution of the beam deposition and electron density profiles is illustrated in fig. 7 for the highest performance pulse (#33643) of the last experimental campaign. It is a 3.7 MA discharge, with D fuel and 18.5 MW of D NBI. An overview of the plasma parameters is given in fig. 8.

Fig. 7 shows that with increasing electron density the neutral beam particles and power are deposited progressively away from the plasma centre this leading to an increasing edge pressure. At some point the edge becomes unstable, an 8 kHz MHD mode often being observed. This causes a slow roll-over in the neutron rates, whenever the ratio of the power deposited between ρ = 0.7 and 1 to the power deposited between ρ = 0 and 0.3 reaches the values given in table 2.

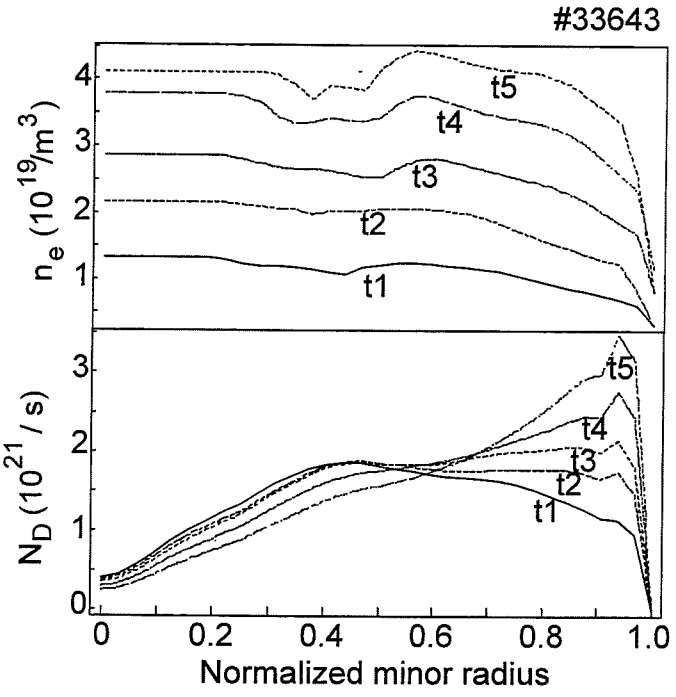

Figure 7: Electron density and calculated neutral beam particle deposition (integrated over flux surface) profile evolution vs. normalized minor radius at t1=12.0 s, t2=12.4 s, t3=12.8 s, t4=13.1 s, t5=13.3 s.

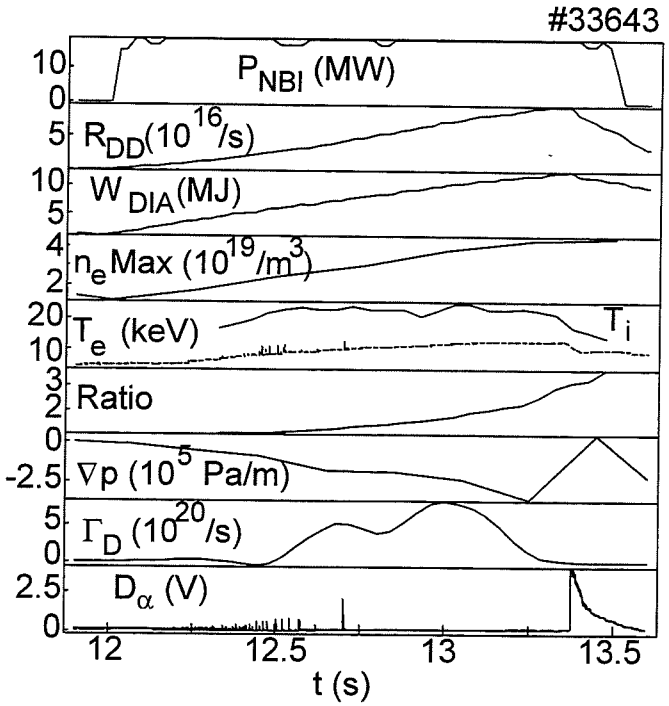

Figure 8: Overview of plasma parameters for pulse #33643, neutral beam power, DD reaction rate, total stored energy from the diamagnetic loop, maximum electron density from LIDAR, electron and ion temperature, ratio of particles deposited between normalized minor radius ρ=0.7 and ρ=1 to those deposited inside a ρ=0.3, electron + ion pressure gradient at R=3.77 m. deuterium gas influx rate. vertical Dα intensity

Ratio at slow roll-over	Configuration	I_p (MA)	Pulses averaged
2.1±0.2	HFE	3	16
2.8±0.3	HFE	3.7	8

Table 2

b) Grassy ELMs

Grassy ELMs (type III ELMs) provide a means of controlling the plasma density, since they are associated with a temporary decrease in confinement resulting in increased particle losses from the edge region ($\rho \sim 0.8 - 1.0$) [5]. This can be seen in the nearly constant ratio of central to edge neutral beam particle deposition (fig. 9, 10) while the grassy ELMs last. Their repetition frequency can be as high as 2 kHz immediately after the L-H transition, this gradually slowing until they disappear completely. The H-factor rises approximately linearly with time till after the end of the grassy ELM period. The deliberate generation and control of these type III ELMs could be a way of producing long H-modes with confinement approaching that of ELM-free discharges, i.e. with H-factors well above 2.

The crucial parameter controlling the ELM frequency is the edge T_e or ∇T_e, the increase in T_e after a sawtooth crash resulting in a decrease in the ELM frequency. This suggests that these ELMs are caused by resistive ∇p modes, the stabilizing effect of the increasing T_e being larger than the destabilizing effect of the increase in ∇p [6]. That ELMs are induced by the cooling effect of strong gas puffing, as in

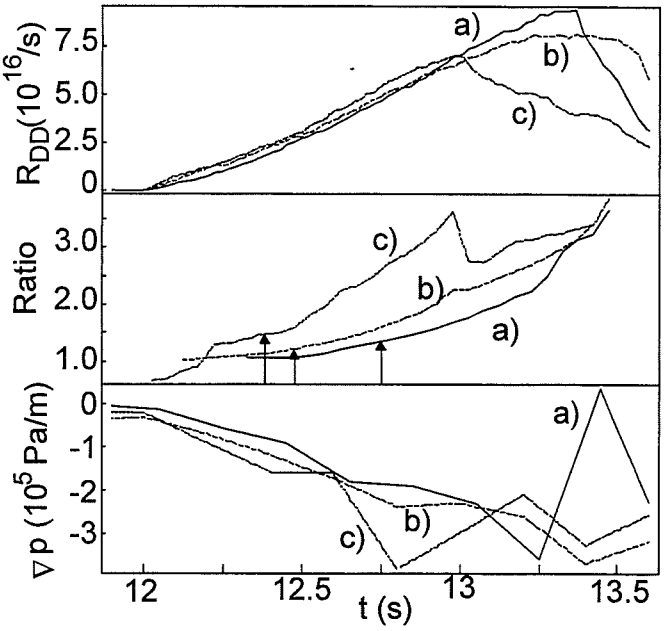

Figure 9: DD reaction rate, ratio of particles deposited as defined in fig. 8 and electron + ion pressure gradient at R=3.77 m vs. time for a) pulse 33643, b) pulse 34499, c) pulse 32925, which have different target densities. The ↑ indicates the end of the threshold ELM period.

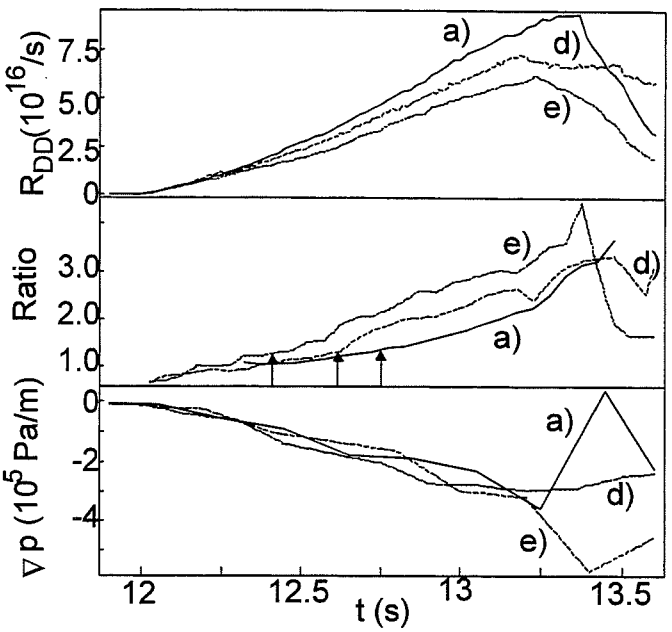

Figure 10: DD reaction rate, ratio of particles deposited as defined in fig. 8 and electron + ion pressure gradient at R=3.77 m vs. time for a) pulse 33643, d) pulse 33701, e) pulse 33680, which have the same target density. The ↑ indicates the end of the threshold ELM period.

the 1991 record shot #26087, is easily understood (fig. 11). The dependence of the threshold ELM duration on D_α (fig. 12) is supposed due to the increased recycling. This has a stabilizing effect by reducing ∇p through charge exchange processes, the effect being larger than the destabilization resulting from the reduction in conductivity due to the falling temperature.

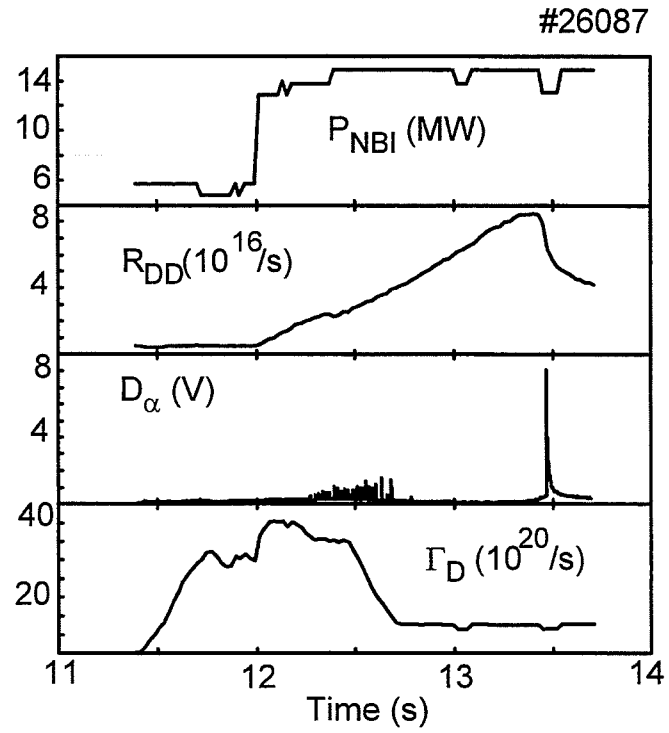

Figure 11: Beam power, neutron rate, vertical D_α intensity and deuterium gas influx rate for a high performance pulse in 'old' JET

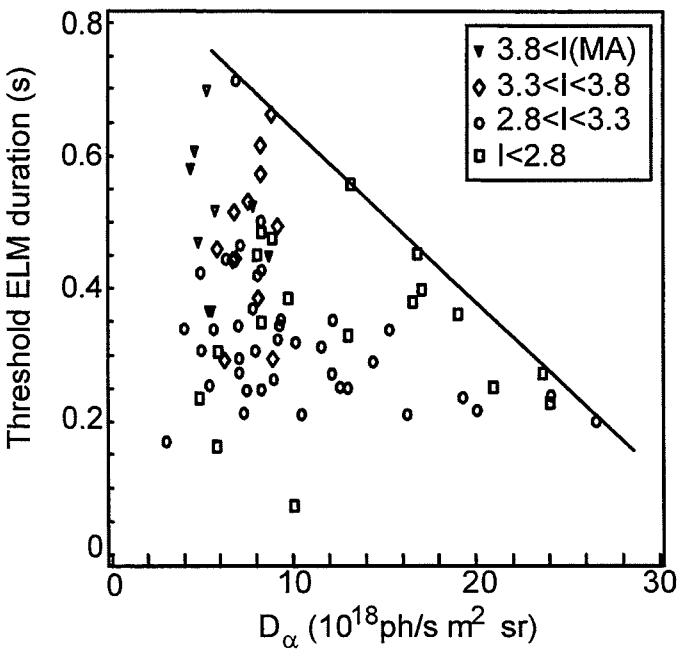

Figure 12: Threshold ELM duration versus vertical D_α intensity sorted by plasma current

c) Recycling

The influence of recycling neutrals on the edge pressure gradient is difficult to quantify. This is because the influx can be highly localized and therefore difficult to measure and because its effect on the pressure gradient can vary. When significant ionization of the neutral influx occurs just inside the seperatrix, this leads to a steepening of ∇p. On the other hand, charge exchange collisions with the higher temperature plasma ions could result in a decrease of ∇p. An additional complication is the difference in behaviour of the three plasma-facing surfaces from which recycling will occur, the carbon tiles of the divertor, the carbon tiled limiters and the metallic walls.

The initial recycling levels in the latest experimental campaign as measured by the D_α line intensity (fig. 13) were found to be high, particularly when compared with the recycling behaviour in the 'old' machine. This may be explained by the following differences between the 'old' and 'new' JET machines:

- For the present campaign, the area of the vessel walls covered with CFC tiles has been reduced. The metallic (Inconel) inner and outer walls are protected by a number of poloidal belt limiters.
- Both the baking (300 °C) and operating temperatures (250 °C) have been reduced from those used in previous campaigns (350 and 300 °C, respectively), these being limited by the risk of possible damage to the divertor coil epoxy. While an increase in the operating temperature to 320 °C improved conditioning, little difference was observed with regard to the performance.
- The divertor tiles are mounted on water cooled supports kept at 40 °C between pulses.

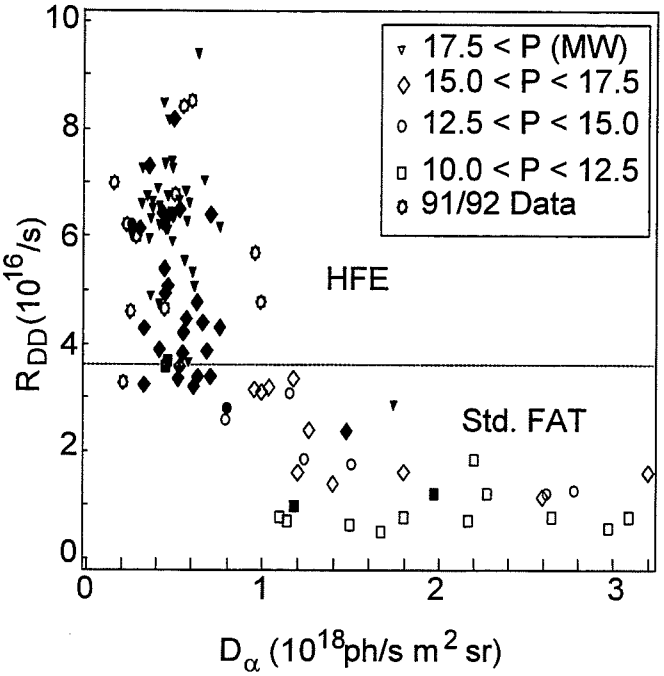

Figure 13: DD reaction rate vs. vertical Dα intensity sorted by neutral beam input power P (MW) for High Flux Expansion (HFE) and standard FAT configurations. Filled symbols refer to pulses with cryo-pump.

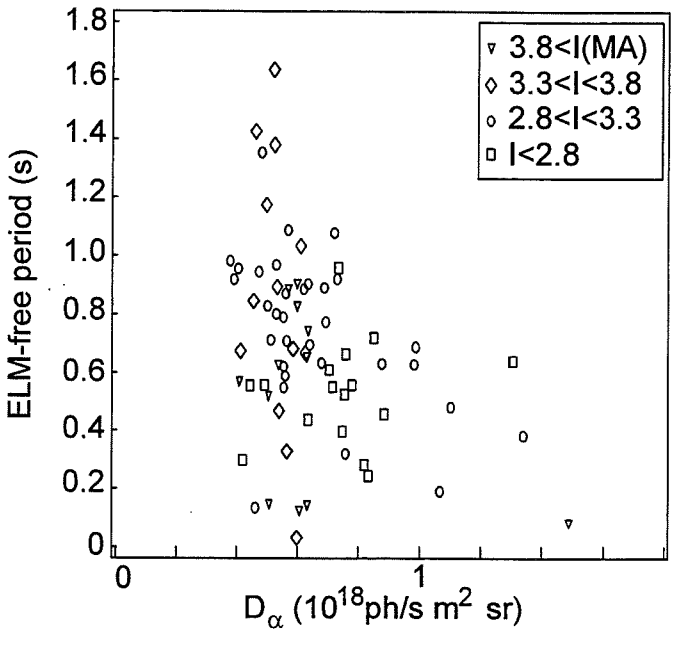

Figure 14: ELM free period vs. vertical Dα intensity sorted by plasma current I (MA)

Overnight D and He GDC and Be evaporations were used to condition the vessel, but the most significant improvement resulted from the use of the divertor cryo-pump from August 1994, when the lowest recycling conditions were achieved (fig. 13). In fig. 15 a comparison is made between two 'standard fat' discharges, #32285 being run with the cryo-pump and #32270 without. The poorer resilience of this configuration to edge instabilities compared with the HFE pulse #33643 (fig. 8) can be seen in the shorter ELM-free period and more frequent ELMs; further, the lower D_α intensity in pulse 32285 is evident, this leading to a longer threshold ELM duration and a delayed build-up in the beam deposition profile ratio. As for the HFE, the ratio reaches values of ~2-3 at the onset of the terminating ELMs. Despite the use of the cryo-pump, a difference is still seen between the pumping in the 'old' and 'new' JET. Fig. 16 compares (1 - the fuelling ratio), which represents the efficiency of wall/limiter/target tile pumping during 3 typical pulses with 16MW of NBI, a single null configuration on the C target tiles in the old machine and a HFE and fat configuration run on the same day with the cryo-pump in the new machine. A significant difference is seen between the HFE and fat pulses, but even the HFE does not achieve the pumping of the old JET.

The active pumping during the ELM-free phase is usually small compared to the beam fuelling rate, but is significant during the pressure bursts following the giant ELMs. This leads to a net depletion of the wall and divertor target plates, so that after a series of deliberately ELMy discharges one can achieve lower

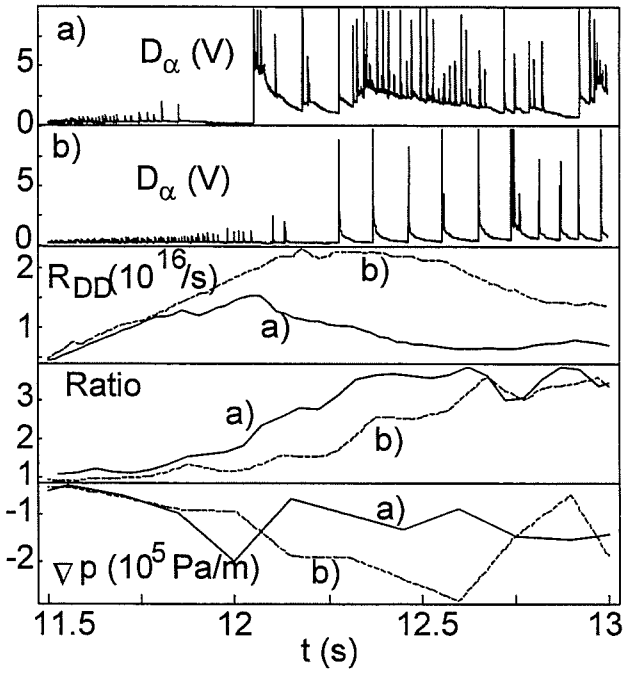

Figure 15: Comparison for standard FAT configuration pulses a) #32270 (without cryo-pump) and b) #32285 (with cryo-pump) of vertical Dα intensity, DD reaction rate, ratio of particles deposited between normalized minor radius ρ=0.7 and ρ=1 to those deposited inside ρ=0.3 and electron + ion pressure gradient at R=3.77 m.

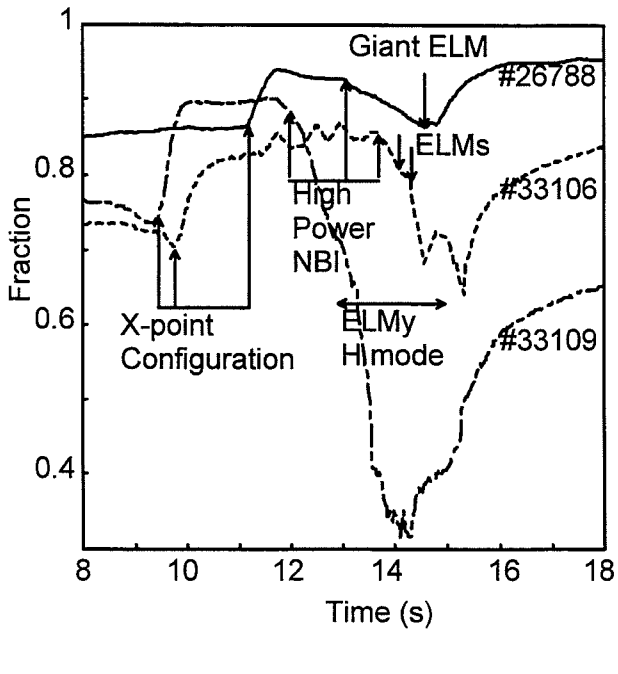

Figure 16:. Fraction of the number of particles absorbed by the walls, target tiles and cryo-pump relative to the total particle input. #26788 old JET, 33106 HFE, #33109 std. fat.

target densities and a reduced plasma fuelling excess over the beam fuelling. Both these effects result in longer ELM free periods due to the improved ratio of core to edge neutral beam fuelling and the reduced edge pressure gradients.

Despite conditioning and depletion there usually remains a net source of particles during the ELM-free phase over and above the beam + gas fuelling which is typically 30 % of the total fuelling (table 3). The sensitivity to

- the vessel temperature and to the limiter fuelling scenario might suggest that the walls and limiters are the source of these particles.
- the target tile temperature during conditioning and to the target material (C or Be) suggests that the target is the source, although the tile heating experiment showed no sign of temperature dependent outgassing during heating from ambient to 1250 °C during the pulse.

	typical 94/95 pulse	#26087	#33643
neutral beam (source)	$1.5\ 10^{21}\ s^{-1}$	$1.2\ 10^{21}\ s^{-1}$	$1.6\ 10^{21}\ s^{-1}$
gas puff (source)	none	$4\ 10^{21}\ s^{-1}$	$8\ 10^{20}\ s^{-1}$
cryo-pump (sink)	$< 5\ 10^{20}\ s^{-1}$	none	$< 5\ 10^{20}\ s^{-1}$
wall/limiter/target (source)	$\sim 4\ 10^{20}\ s^{-1}$	none	none

Table 3 Deuterium fuelling and pumping rates

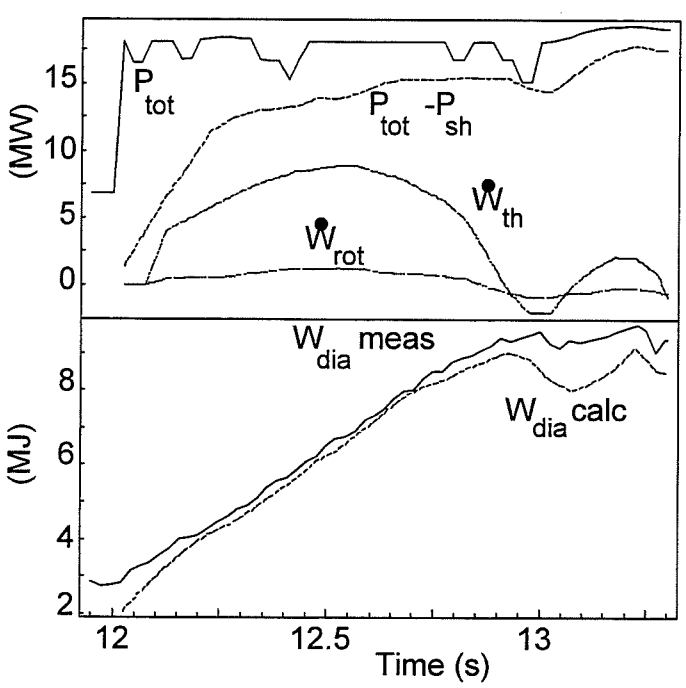

Figure 17: P_{tot}: total input power, P_{tot}-P_{sh}: P_{tot} adjusted for shine through, dW_{th}/dt, dW_{rot}/dt rate of change of thermal and rotational energy, W_{dia}:meas. measured and W_{dia} calc calculated from measured W_{th} and calculated fast particle distribution

Evidence that the recycling neutrals influence the plasma through different atomic processes at different stages of the discharge comes from the measurement of the thermal energy and toroidal angular momentum confinement times. The former for example is defined as $\tau_E = W_{th} \Big/ P - \frac{dW_{th}}{dt} - \frac{dW_{rot}}{dt}$ its components being illustrated in fig. 17. The confinement times can differ significantly, by up to a factor of 2, during the ELM free period (fig. 18). The ions carry the total toroidal angular momentum of the plasma, but only about half the total thermal energy. An imbalance can only occur through the replacement of plasma ions by recycling neutrals in charge exchange collisions. Therefore charge exchange collisions must dominate ionizations in

the earlier phase of the ELM free period[7]. The maximum imbalance between τ_L and τ_E is generally about 0.5-0.8 s after the start of NBI. As the relative importance of the charge exchange collisions decreases and loss of ion-electron pairs across the seperatrix starts to dominate, τ_E approaches τ_L, the point at which they become equal being correlated to the time of the slow roll-over in the neutron rates. For the 30 highest performance pulses of the 1994/95 campaign, the slow roll-over occurred within ±170 ms of τ_E becoming equal to τ_L. It should be noted that τ_L and τ_E are derived from averaging the time derivatives of energy and angular momentum over intervals of 150 ms. The charge exchange process is thought to be beneficial in that it reduces the edge temperature, the edge density remaining unchanged. In the record R_{DD} pulse #33643, the stabilizing effect of the charge exchange processes on the edge pressure gradient was extended through a small gas puff before the end of the threshold ELMs. Fig. 19 shows that this resulted in a nearly constant τ_L to τ_E ratio throughout much of the H-mode duration. The enhancement of the charge exchange interactions by gas-puffing was repeated in pulse 33649 with a similar τ_L to τ_E ratio.

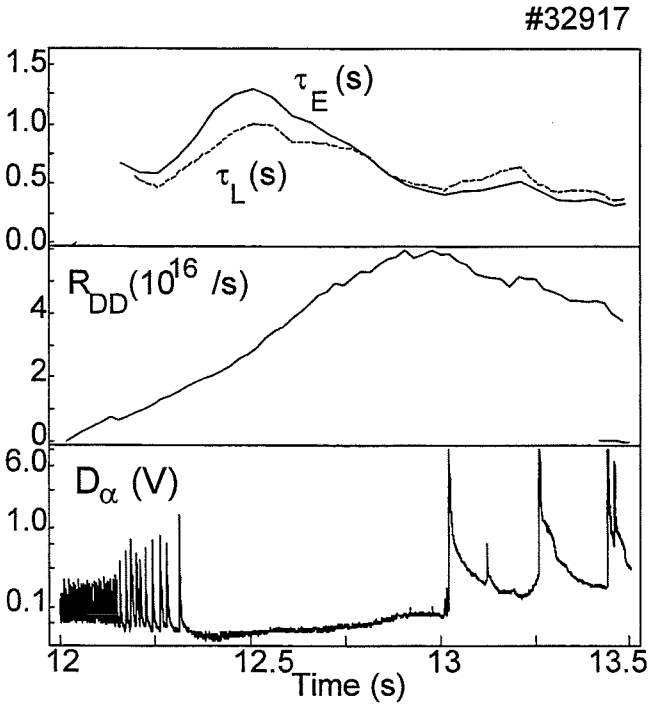

Figure 18: Imbalance between energy and toroidal momentum confinement time, DD reaction rate and vertical D_α intensity

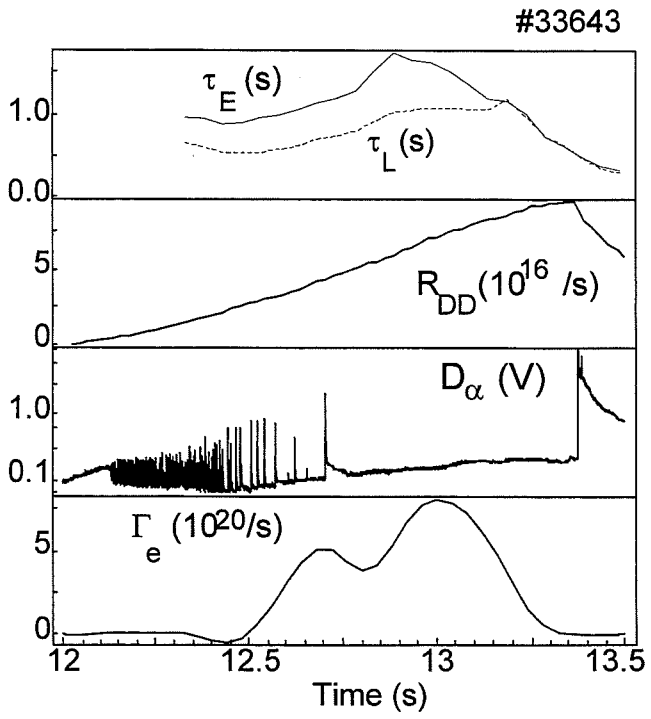

Figure 19: Imbalance between energy and toroidal momentum confinement time, DD reaction rate, vertical D_α intensity and deuterium gas influx

PERFORMANCE OPTIMIZATION

- Of crucial importance in achieving high performance in the hot-ion regime is a low target density, which in the present campaign, is limited by the maximum permitted beam shine-through. This is illustrated in figure 20, this diagram including all of the best 30 pulses of the current operations.

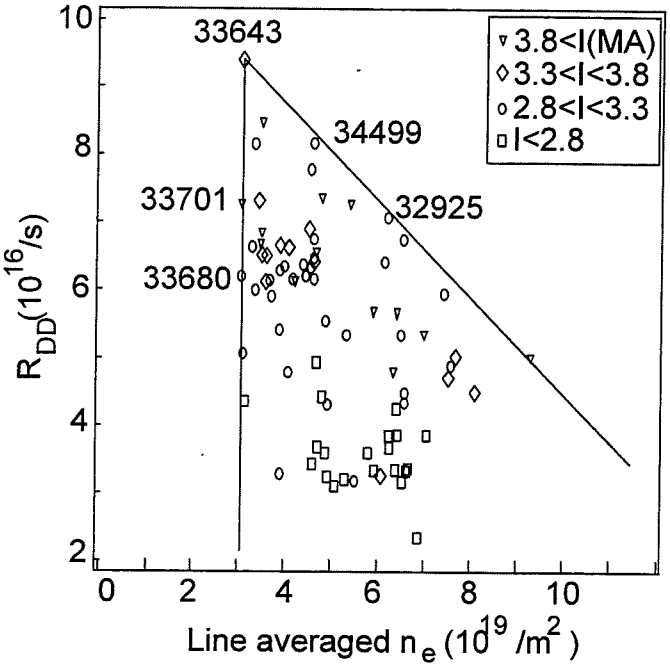

Figure 20: DD reaction rate vs. line averaged target electron density sorted by plasma current I (MA). The solid lines mark the boundary of the operational space

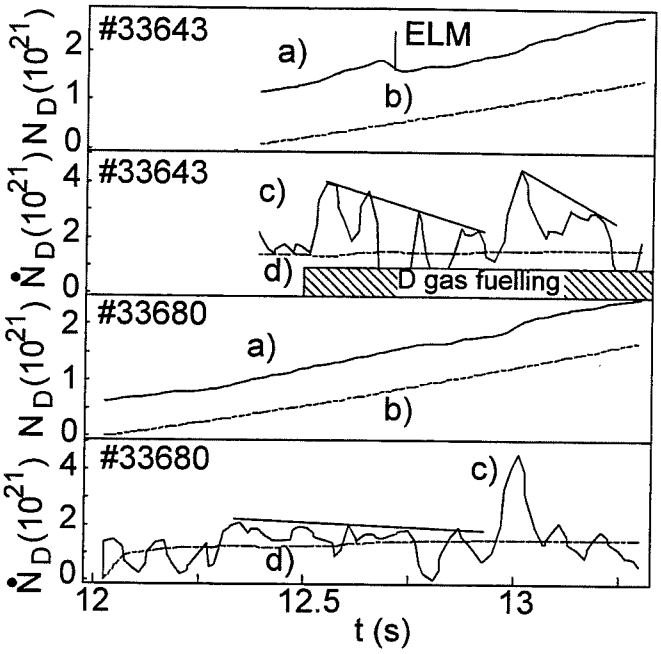

Figure 21: a) total number of deuterons in the plasma and its derivative c), b) total number of deuterons injected by NBI and its derivative d) for two low target density pulses. Pulse 33643 has gas fuelling.

- A low target density requires a sufficiently low level of recycling. In pulses having the best conditioning, the increase in the total D count corresponded to or, in one case, fell below the beam fuelling rate. Figure 21 illustrates two such low target density pulses, 33643 and 33680. In the latter the time derivative of the total deuterium content of the plasma approximately matches the beam fuelling particle flux. The highest performance pulse 33643 is the only example where the pumping is so strong that the beam fuelling is insufficient and D gas fuelling is required to maintain the plasma density. More usually in these hot-ion H-mode discharges the density rise exceeded the beam fuelling rate by ~30%.
- An extensive investigation of the effect of the particle influx on the beam deposition and n_e profiles showed no marked dependence, figure 22. This somewhat surprising result is thought to be partly due to the high probability of the inflowing neutral particles to undergo a charge exchange reaction. Those newly formed hot neutrals which do not leave the plasma can penetrate deeper into the plasma before being ionized. This process could spread the influx particle deposition over a wider range of radii which might explain why there is no change in the density profiles.
- The calculations of the centre to edge beam deposition and of the neutron emission profiles depend critically on the neutral beam deposition/attenuation profiles. Local neutral beam densities have been measured directly from the $\pi 4$ component of the Stark-split beam emission spectrum. Fig. 23 shows the good agreement between the calculated and measured values. The reduction in the neutral beam

penetration is seen to be a continuous process due to the rising plasma density. Neither slow roll-overs, nor ELMs result in a sudden, total blocking of the heating beams.

- The degradation of the energy confinement, typically starting well before any MHD instabilities are observed, is believed to be caused by continuously increasing losses due to the rising fraction of the neutral beam power (and particles) being deposited near the plasma edge (fig. 7, 9, 10). The excellent agreement between the measured diamagnetic energy and the one calculated from the measured thermal energy and calculated fast particle population indicates that the fast particle losses are small. Clearly the use of tunable energy beams, which have higher energies with their low current and better penetration towards the end of the ELM-free period, would both reduce the plasma density rise and give a more favourable edge to centre deposition ratio.

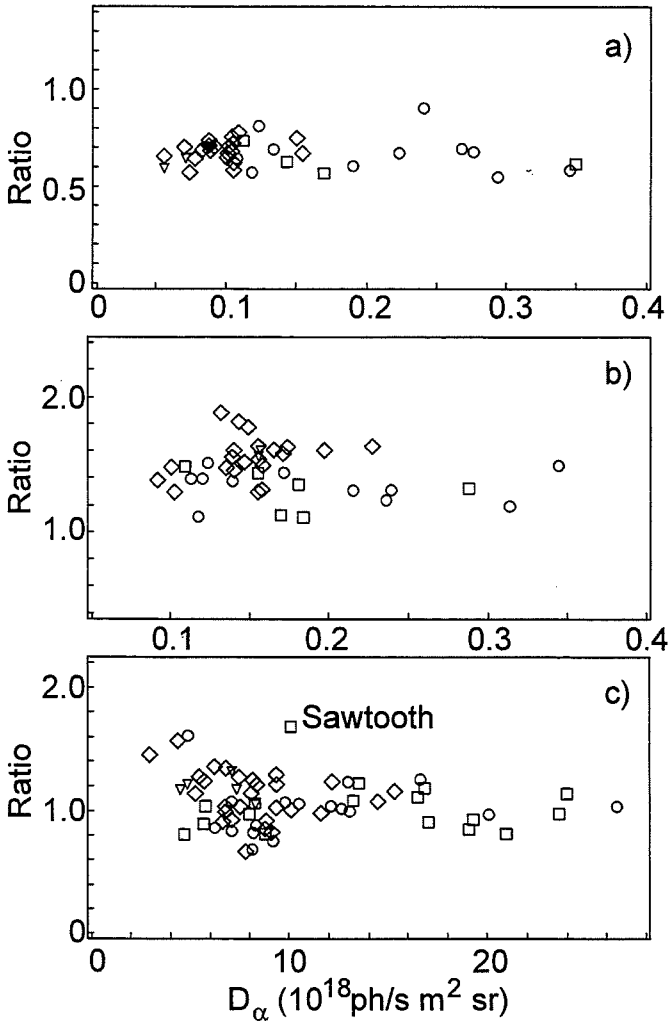

Figure 22:

a) Inverse peaking factor of beam particle deposition at start of NBI vs. horizontal D_α. The peaking factor is defined as the ratio of the number of particles deposited between a normalized minor radius of 0.0 and 0.55 to those deposited between 0.55 and 0.85.

b) Ratio of initial to final peaking factors of beam deposition vs. horizontal D_α. The initial value is taken at the start of NBI; the final value is taken at the roll-over of R_{DD}.

c) Ratio of initial to final n_e peaking factors vs. divertor D_α. The peaking factor of n_e is defined as the ratio of electron density integrated between a major radius of 3.35 m and 3.25 m to the electron density integrated between a major radius of 3.8 m and 3.65 m.

Figures sorted by peak R_{DD} , ∇ $8\times10^{16}\leq R_{DD}$, $\diamond$ $6\times10^{16}\leq R_{DD}<8\times10^{16}$, $\circ$ $4\times10^{16}\leq R_{DD}<6\times10^{16}$, $\square$ $R_{DD}<4\times10^{16}$.

- The d-d thermal fusion component significantly exceeds the beam thermal contribution (fig. 24). The shift of the neutral beam power deposition towards the edge causes a continuous broadening of the neutron emission and ion temperature profiles. (The ion temperature reaches its peak central value after only 0.5 s and then remains constant for up to ~ 1 s (fig. 8)). Surprisingly the profile evolution has little effect on the global neutron rate, which in the highest performance pulses at any particular target density (fig. 20) rises at a nearly constant rate till the slow roll-over (fig. 9).

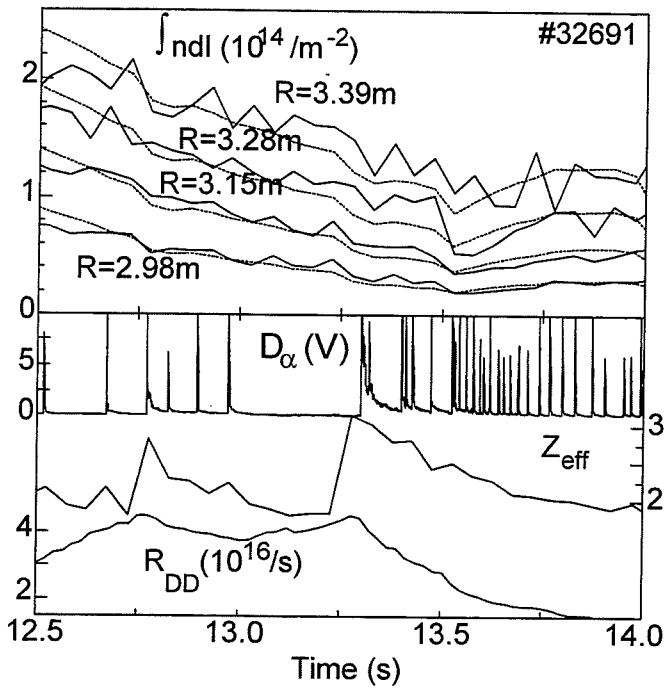

Figure 23:. Measured and calculated line of sight integrated neutral beam density, vertical D_α intensity, effective charge and DD reaction rate

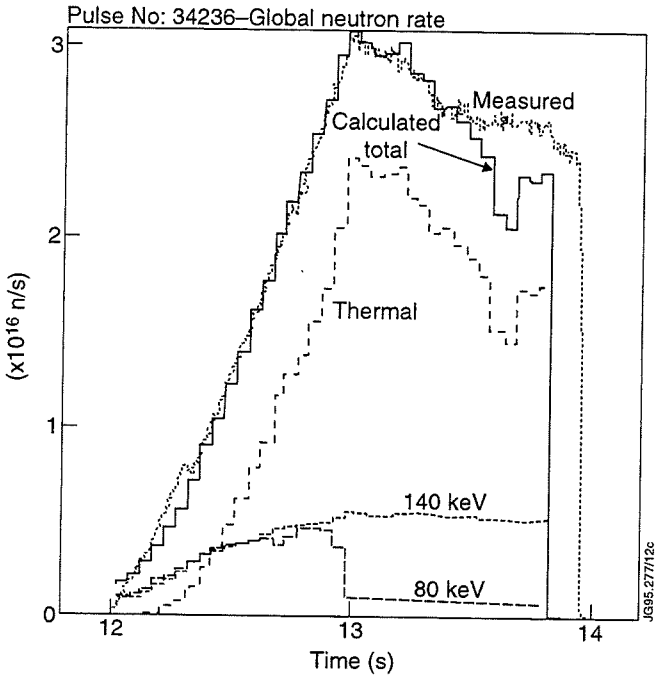

Figure 24:.Directly measured and from charge exchange measurements calculated total neutron rates

SUMMARY

The foremost problem in achieving a high fusion yield in the new JET was to design a plasma stable to pressure gradient driven instabilities. This was achieved by a number of different measures. Of importance was the development of a magnetic configuration with sufficiently high shear. Equally important are low recycling conditions, which gave access to low target densities and proved to be a means of achieving long grassy ELM periods. These were desirable since they delay the unfavourable shift of the neutral beam deposition towards the plasma edge, thereby postponing the onset of pressure gradient driven instabilities. A further process helping to stabilize the edge pressure gradient was identified as charge exchange interactions. In two pulses these were enhanced by a moderate gas-puff at the time of the threshold ELM period. Usually τ_E is found to decay well before the onset of MHD instabilities. The increased losses are thought due to the unfavourable beam deposition profiles.

[1] GTA Huysmans et al, this conference

[2] P Smeulders et al., EPS 1995, Bournemouth, UK

[3] R D Gill et al., this conference

[4] P Lomas et al., this conference

[5] P R Thomas et al., EPS 1992, Innsbruck, Austria

[6] A L Colton et al., IAEA 1994, Seville, Spain

[7] K-D Zastrow et al., to be published, 1995

High Fusion Performance Plasmas in JET

P J Lomas, S Ali-Arshad, B Alper, M Bures, B Balet, J P Christiansen, G Cordey, N Deliyanakis, H De Esch, G Fishpool, R Giannella, T Hender[1], G Huysmans, O N Jarvis, T T C Jones, R Konig, K Lawson, K McCormick[2], A Maas, F Marcus, F Nave, V Parail[3], L Porte, R Sartori, B Schunke, P Smeulders, A Taroni, K Thomsen, P R Thomas.

JET Joint Undertaking, Abingdon, Oxfordshire, OX14 3EA, UK.

[1] UKAEA, Culham Laboratory, Abingdon, Oxfordshire, OX14 3DB, UK.

[2] Max-Planck Institut für Plasmaphysik, Euratom association, 85748, Garching, Germany.

[3] Permanent address: RRC Kurchatov Institute, Moscow, Russia.

ABSTRACT

The new JET pumped divertor has been operated with diverted plasmas up to 6MA with additional heating up to 20MW NBI, 17MW ICRH and 7MW LHCD to give a total combined heating power up to 30MW in H mode. Research has concentrated on long pulse steady state ELMy H-modes, high current high power ELMy H-modes and transient ELM-free

H-modes including the hot ion regime. DD fusion performance has been demonstrated sufficient to study α particle effects in future D-T operation in JET where Q_{DT} values between 0.25 (steady state) and ~1 (transient) are expected.

ELM FREE PERIOD

The geometry of both core and diverted plasma play an important role in determining the nature of the H mode.

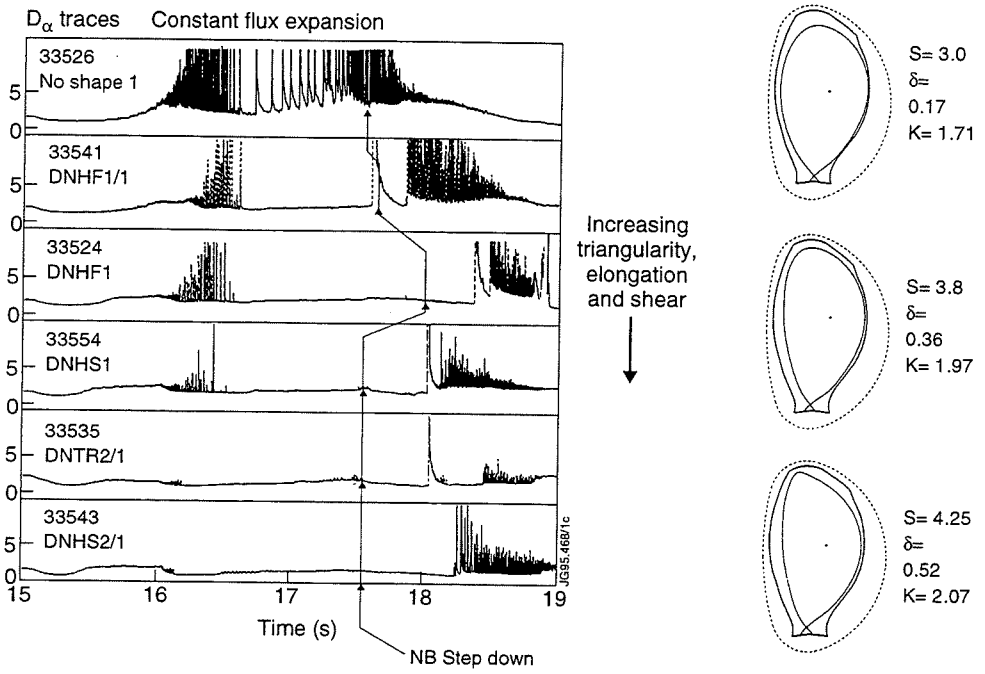

Fig.1: Behaviour of the H mode in the shear scan of constant flux expansion for 2.5MA/2.5T/10MW

Increasing core plasma shaping increases the ELM free period.

Increasing divertor flux expansion also increases ELM free period, as does a reduction in main chamber recycling.

Raised shear raises edge stability limits.

Reduced neutral leakage reduces edge gradients.

OUTER MODE STABILITY

Signature:-

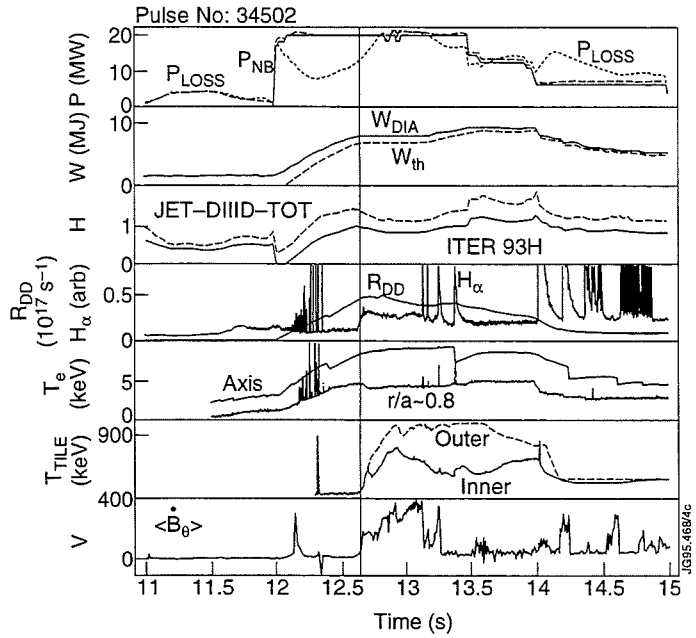

Fig.2: Typical time traces for a "slow rollover" in performance initiated with an outer mode

Nature:-

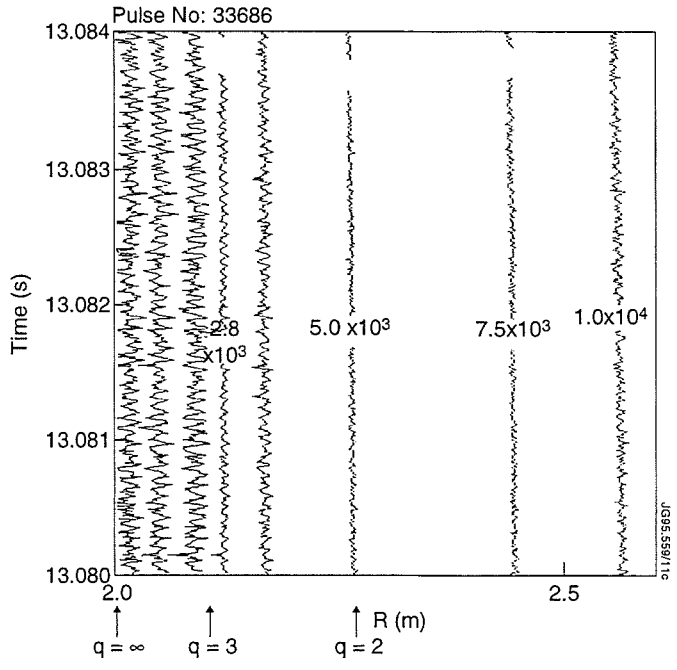

Fig.3: Illustration of outer mode

For JET-DIIID scaling, expect:

$$\beta_N^{th} = 0.89F\left(P/B^2\right)^{1/2}$$

where F is the confinement enhancement factor.

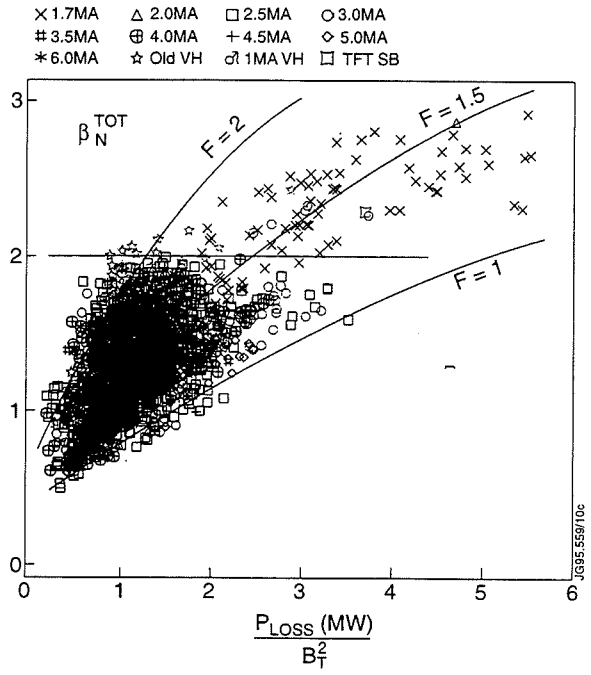

Fig 4: Normalised β_N against normalised loss power.

There is no hard β limit observed, but high confinement enhancement is only seen at $\beta_N \leq 2$. There is insufficient beam power to reach $\beta_N \leq 3$. within the ELM free phase at high current and field.

CONFINEMENT ENHANCEMENT

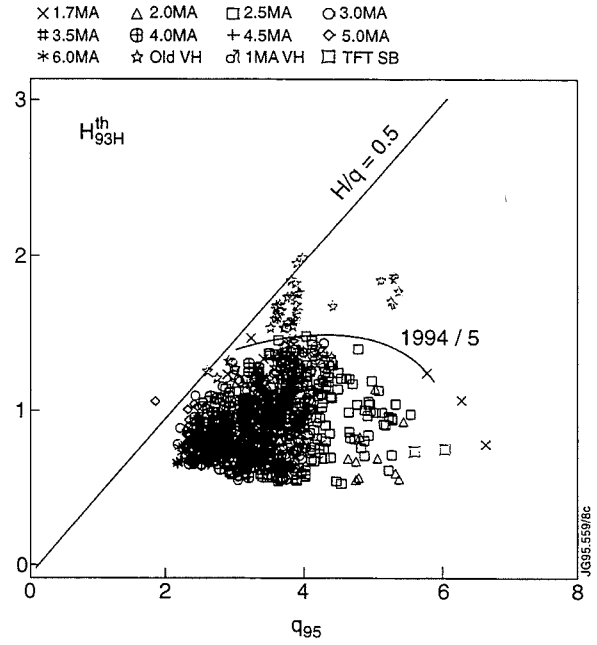

Fig.5: Thermal confinement enhancement H^{th}_{93H} over ITER-93H versus q95 for L, ELMy , and ELM free data from 1994/5 and previous high enhancement data (labelled "OLD VH").

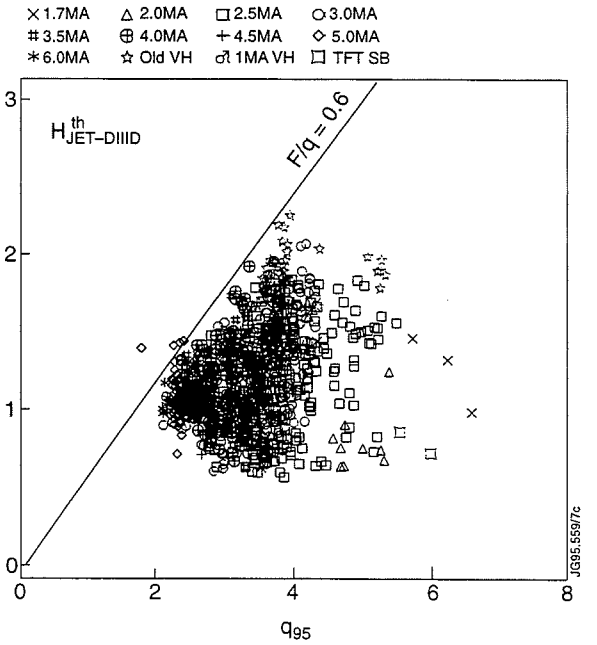

Fig.6: Thermal confinement enhancement $H^{th}_{JET-DIIID}$ over JET-DIIID versus q_{95} for the same data set.

Note the difference in scaling prediction:

$$\frac{\tau_{93H}}{\tau_{JET-DIIID}} \sim \frac{n_e^{0.17} B^{0.3} K^{0.6}}{P_{Loss}^{0.2}}$$

It is surprising that these small differences separate out old and new data.

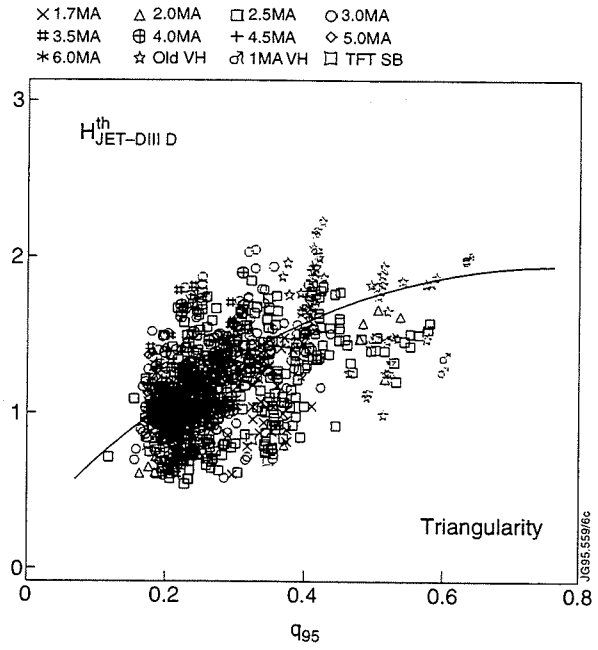

Fig.7: Thermal confinement enhancement over JET-DIIID versus triangularity (top-bottom average)

Although there is a trend of increasing confinement quality with triangularity, other factors are clearly also important.

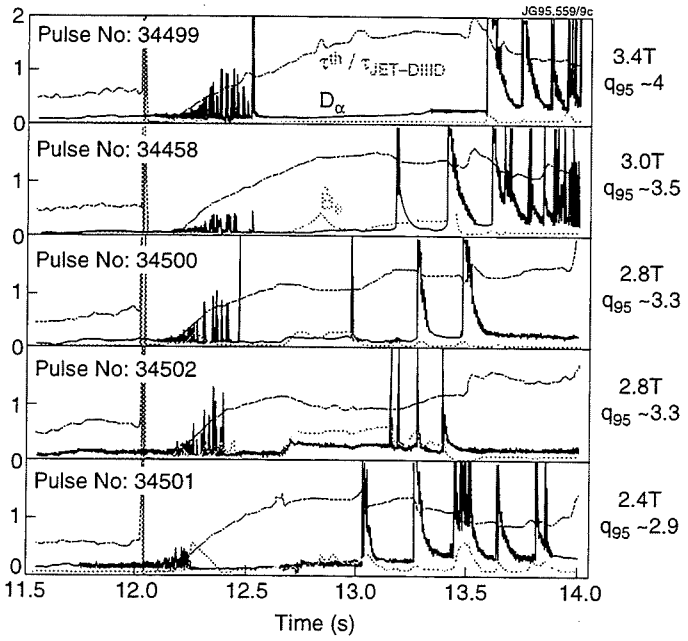

Fig.8: Time behaviour for various pulses in a q scan at 3MA. For each shot confinement enhancement, D_α and MHD amplitude are shown.

The q95 dependence of confinement enhancement appears to be associated with the appearance of various internal MHD modes including the so called OUTER MODE.

FUSION PERFORMANCE

Expect D-D rate $R_{dd} \propto \frac{w^2_{dia}}{vol}$

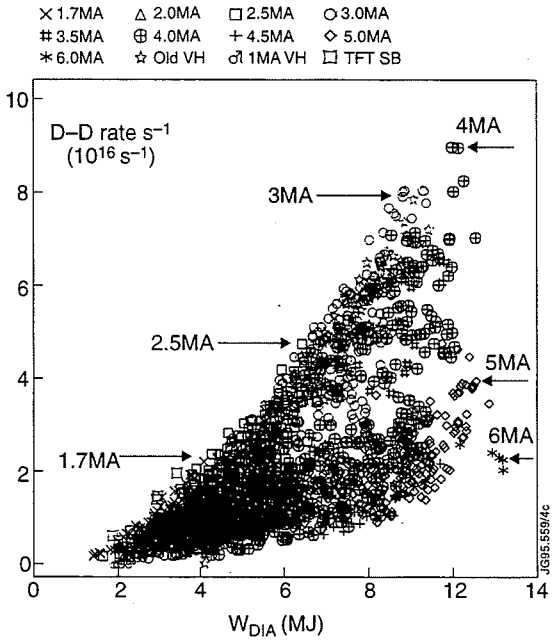

Fig.9: D-D rate R_{dd} plotted against w_{dia}. The maximum fusion performance achieved at various currents is indicated on the figure.

For a given stored energy the fusion power obtained in ELM free regimes is a factor ~ 2.5 better than ELMy regimes, as expected with $T_i >> T_e$ and more peaked profiles. The departure from W^2 appears consistent with a q dependence of profile peaking.

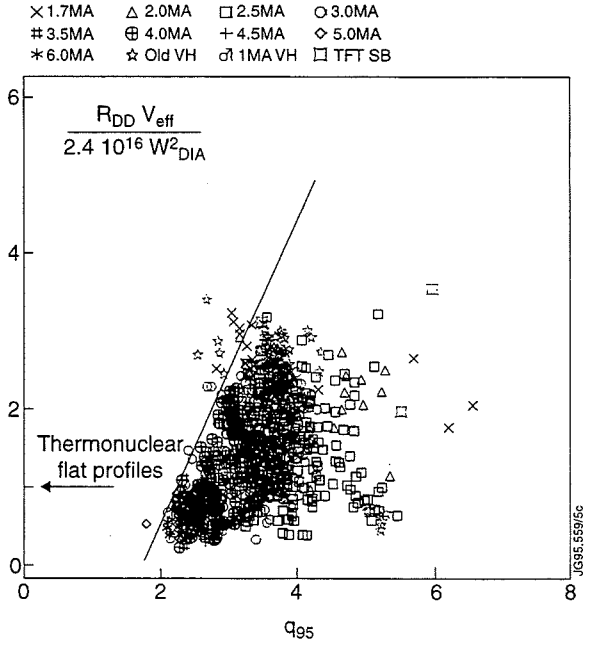

Fig.10: Normalised reactivity versus q_{95}. The constant is chosen such that a pure thermonuclear plasma (no beam reactions) with flat profiles and $T_i = T_e$ ~ 15keV would have a normalised reactivity of 1.

The figure suggests that the optimum reactivity including T_i, T_i/T_e, profiles and beam plasma contribution is obtained around $q_{95} \sim 4$.

The fusion gain:

$$Q_{|dd} \sim \left(\frac{F}{q}\right)^2 \left(\frac{I_p q}{aB}\right)^2 \left(\frac{R^2 B^2}{g(K)}\right)$$

depends upon
- T_i
- F/q
- Shape parameter $(I_p q / aB)$
- Size
- B^2
- beam-plasma reactivity
- profiles

The factor g(K) describes the variation of elongation with minor radius.

$q \sim \frac{a B_\phi}{R B_\theta}$

$\sim \frac{a^2 B}{R I}$

$\frac{q I}{a B} \sim \frac{a}{R}$

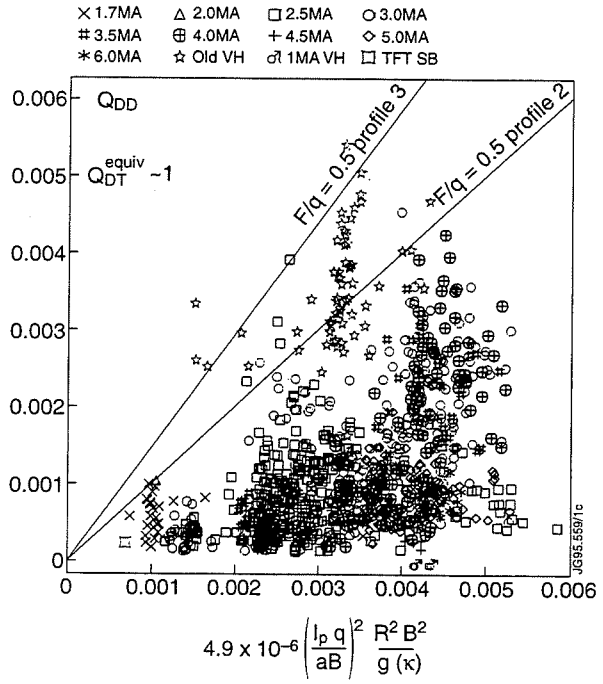

Fig 11: Measured Q_{dd} versus the prediction of the global model.

The scatter on this plot shows that such performance parameters can only serve as a guide to likely performance, but that "profile" shape optimisation is an important factor. The strong dependence upon toroidal field provides a clear motivation for increase in toroidal field on JET.

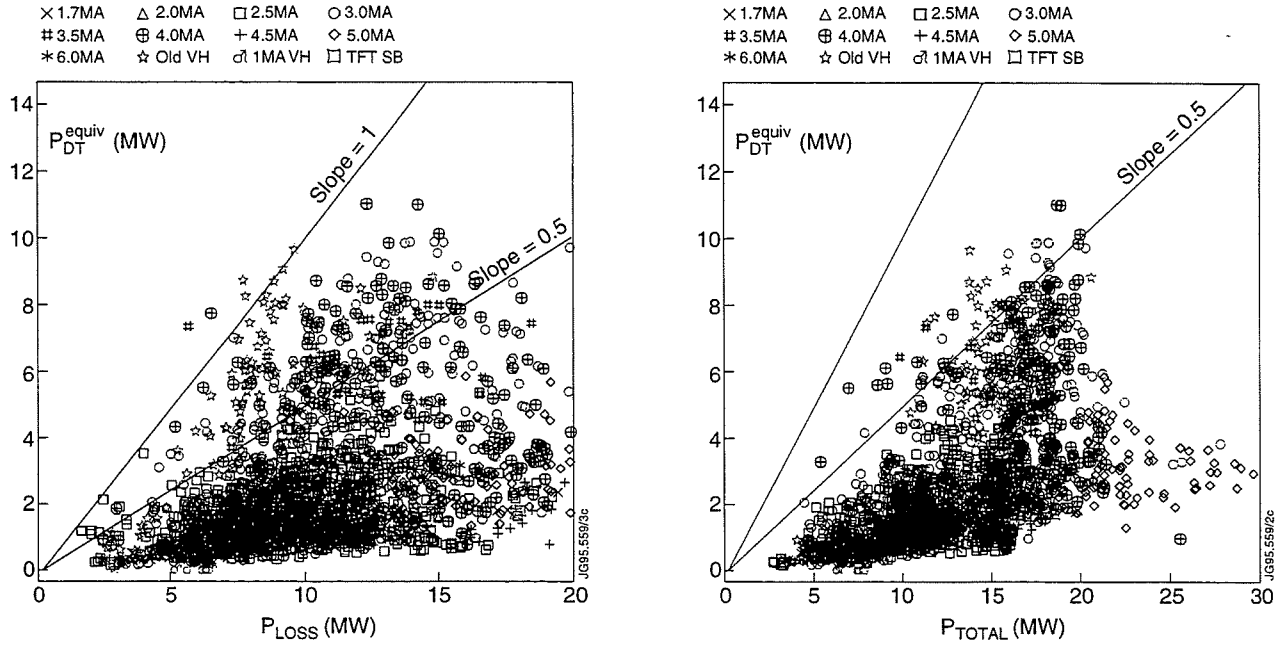

Fig 12: Expected fusion performance in DT operation plotted against (a) loss power (b) input power. The D-T power is calculated from 210 x P_{dd} which is accurate to ±5%.

CONCLUSIONS

The plasma conditions already demonstrated in the MKI pumped divertor correspond to:

- - Total fusion power

  P_{DT}^{equiv} ~ 10 MW transiently
  ~ 6MW steady for 1 sec
  ~ 5MW steady in ELMy regimes

- Fusion gain

  Q_{DT}^{equiv} ~ 1 transiently
  ~ 0.7 steady for 1 sec
  ~ 0.25 steady in ELMy regimes.

Further performance gains are expected from:

- Reduction of neutral leakage and improved pumping.
  longer ELM free phase
  more favourable profiles

- Improved stability with higher TF
  raised q_{95}

- Increased heating power
  25MW beams for D+T injection
  Application of ICRH to performance regimes

- Stabilisation of modes by current profile control LHCD

Evolution of Edge Electron Temperature and Density in JET H-Mode Plasmas

L Porte, D V Bartlett, N Deliyanakis, A Rookes[1].
JET Joint Undertaking, Abingdon, Oxfordshire, OX14 3EA, UK.
[1] Imperial College of Science, Technology and Medicine, South Kensington, London, SW7 2BZ, UK.

INTRODUCTION

- High resolution ECE and reflectometer diagnostics used to study edge T_e and n_e in JET H-mode plasmas.

- Detailed measurements of the temporal evolution of T_e, n_e, ∇T_e and ∇n_e made at the L- to H-mode transition.

- The effect of ELMs on the edge electron temperature has been measured.

- Edge MHD modes which lead to termination of many JET H-modes have been identified.

- ∇p_e is very large in JET H-modes causing large edge bootstrap current and possibly plasma instability.

THE PRINCIPAL DIAGNOSTICS

ECE Heterodyne Radiometer [1]

- A 48 channel single-side-band heterodyne radiometer which can measure either E-mode or O-mode polarisations.

- Absolute calibration obtained against independently calibrated Michelson interferometer. Uncertainty in calibration is ≈10% across the whole spectrum.

- The radiometer covers the RF frequency range $73GHz \leq f_{RF} \leq 139GHz$.

- Spectral resolution, δf_{RF}, determined by IF bandpass filters. $100MHz \leq \delta f_{RF} \leq 500MHz$. This results in effective radial spatial resolution of ≈0.01m at the plasma edge to ≈0.08m at the plasma centre.

- Temporal resolution $\delta t \geq 33\mu s$, limited by video stage low pass filters.

- Smallest measurable temperature change $\delta T_e \approx 10eV$.

O-mode Reflectometer [2]

- A 12 channel O-mode reflectometer probing the plasma at discrete frequencies $18GHz \leq f_{prob} \leq 80GHz$.

- Plasma is probed approx along the equatorial plane.

- Two modes of operation working simultaneously
  fixed frequency mode to measure local variations in electron density profile
  narrow band sweep mode to measure the electron density profile

- Temporal resolution in the two modes of operation is different
  fixed frequency mode $\delta t \approx 1\mu s$
  swept frequency mode $\delta t \approx 3ms$

THE L- TO H-MODE TRANSITION

At the L- to H-mode transition JET plasmas typically change in the following manner :

	L-MODE	H-MODE
$T_e(\rho \geq 0.97)$	$\approx$50eV	$\approx$500eV
$\nabla T_e(0.93 \leq \rho \leq 0.98)$	$\approx 6 keVm^{-1}$	up to $80 keVm^{-1}$
$n_e(\rho \approx 0.98)$	$0.5 \times 10^{19} m^{-3}$	$1.7 \times 10^{19} m^{-3}$
$\nabla n_e(\rho \geq 0.97)$	$\approx 2 \times 10^{20} m^{-4}$	$8 \times 10^{20} m^{-4}$

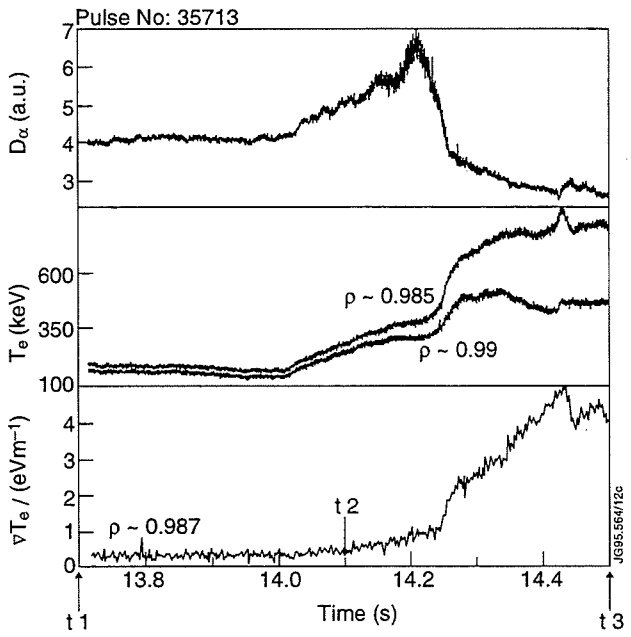

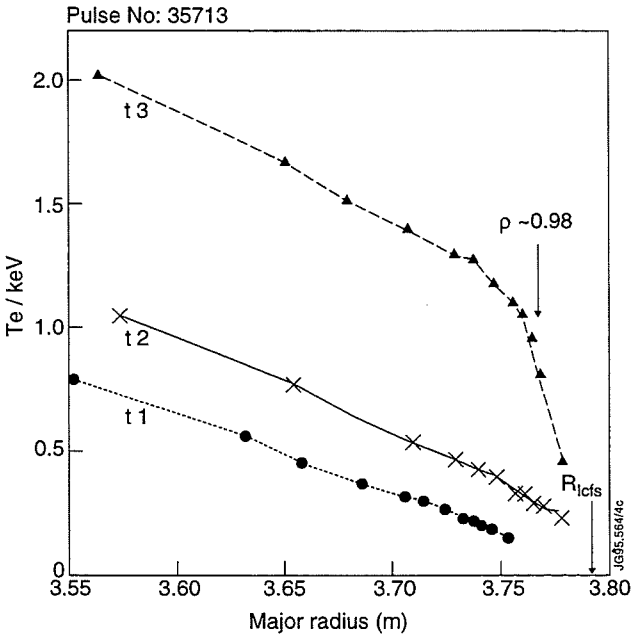

Figure 1a shows the temporal evolution of the D_α light, $T_e(\rho \approx 0.95)$ and $\nabla T_e(\rho \approx 0.987)$ for pulse 35713. The L- to H-mode transition occurs at $t \approx 14.20$sec. Figure 1b shows 3 T_e profiles at times in the ohmic phase, in the L-mode phase and in the H-mode phase.

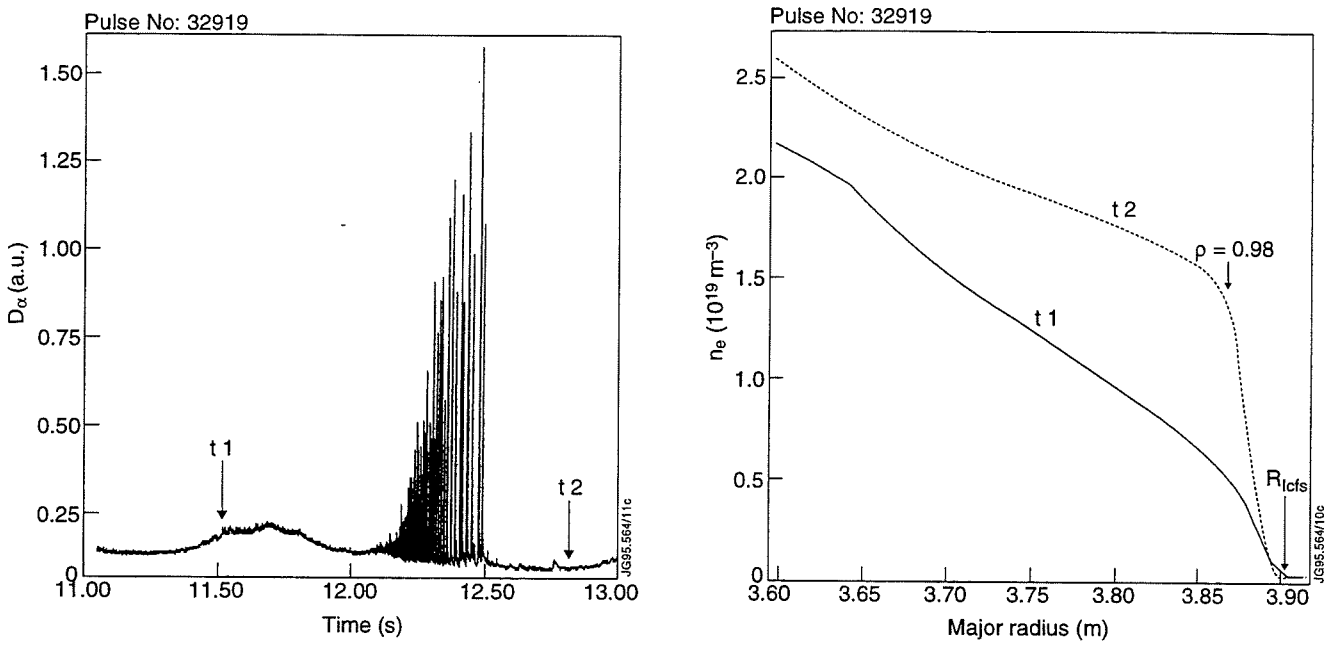

Figure 2a shows the evolution of D_α light at the L- to H-mode transition for shot 32919. Figure 2b displays two n_e profiles at times in the ohmic and H-mode phases for this shot.

- The regions of large ∇T_e and ∇n_e are limited to $\rho>0.98$. This region is ≈2cm which is of order the ion larmor radius.
- This suggests that losses from the plasma edge are dominated by orbit losses.

ELMS

Giant ELMs [3]

- Occur in Hot Ion H-mode plasmas with high power heating and low target density.
- Giant ELMs are global in character
- They cause the plasma particle and energy losses to exceed L-mode values.
- They cause T_e and ∇T_e to fall to L-mode values over most iof the plasma volume.

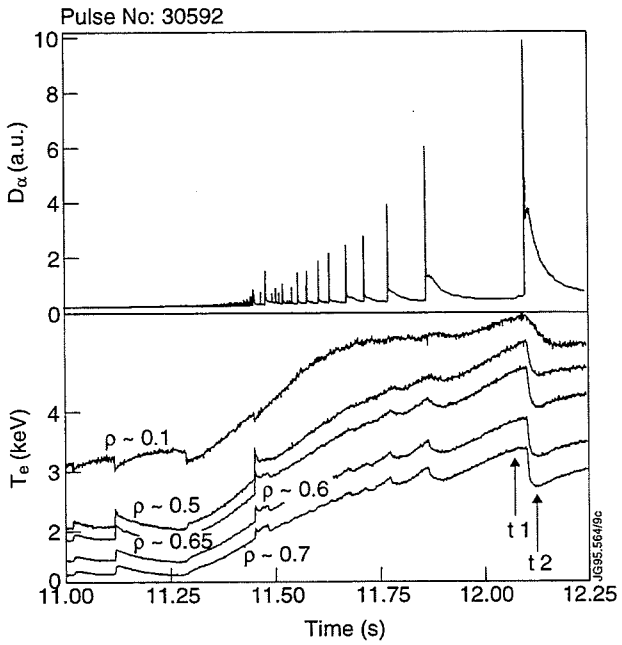

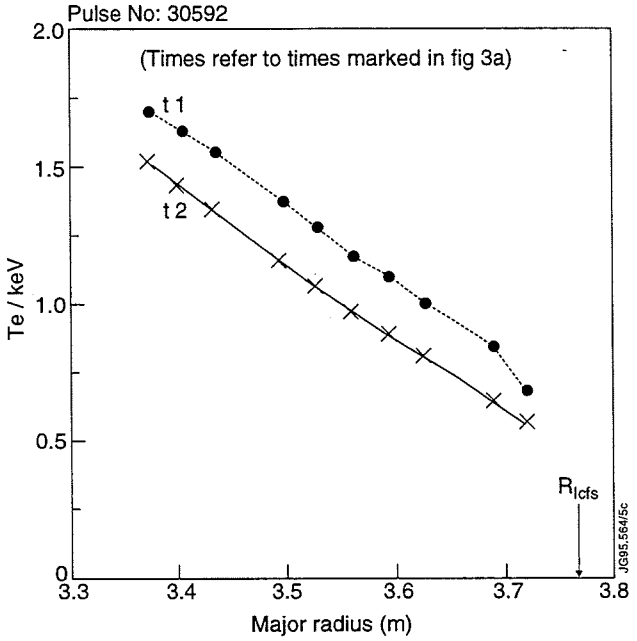

Figure 3a shows the temporal evolution of the D_α light and T_e at several radii $0.2 \leq \rho \leq 0.95$ for pulse 30592. Giant ELMs start with a T_e collapse on a time scale $\delta t < 50\mu s$ followed by a T_e recovery over a period $\delta t \approx 200ms$. Figure 3b shows the effect of the collapse on the T_e profile.

Medium ELMs

- Occur in high power, high density H-modes.
- $T_e(\rho \geq 0.5)$ falls by between ≈50eV and ≈400eV
- $T_e(\rho > 0.9)$ reduced to levels between H-mode and L-mode.

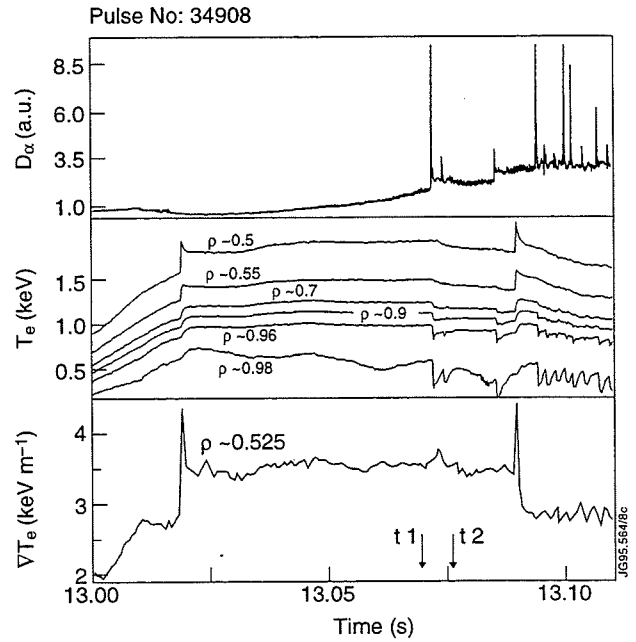

Figure 4 shows the temporal evolution of the D_α light and T_e at several radii $0.50 \leq \rho \leq .985$ and $\nabla T_e(\rho \approx 0.52)$ for pulse number 34908. The L- to H-mode transition occurs at $t \approx 14.168s$. The transition is followed by a sawtooth at $t \approx 54.185s$. With the arrival of the heat pulse $\nabla T_e(\rho \approx 0.5)$ increases from $\approx 2.7 keVm^{-1}$ to $\approx 3.5 keVm^{-1}$ which is typical behaviour in H-modes. The ELMs occur at $t \approx 14.719s$ and $t \approx 14.845s$ but do not affect $\nabla T_e(\rho \approx 0.5)$. A second sawtooth occurs at $t \approx 14.891s$ and this time $\nabla T_e(\rho \approx 0.5)$ falls from $\approx 3.7 keVm^{-1}$ to $\approx 2.9 keVm^{-1}$. This is the opposite to the behaviour in ELM free plasmas.

- Medium ELMs affect the dynamic response of the plasma to sawteeth at minor radii $\rho \geq 0.5$.

Small ELMs

- Occur in high power, high density plasmas and are associated with quasi-stationary H-modes.

- ∇T_e at the occurrence of small ELMs is smaller than for medium ELMs. ($\approx 15 keVm^{-1}$ as compared to $\approx 50 keVm^{-1}$)

- Changes in T_e occur in regions of the plasma limited to $\rho \geq 0.97$, and typically $\delta T_e \leq -70eV$.

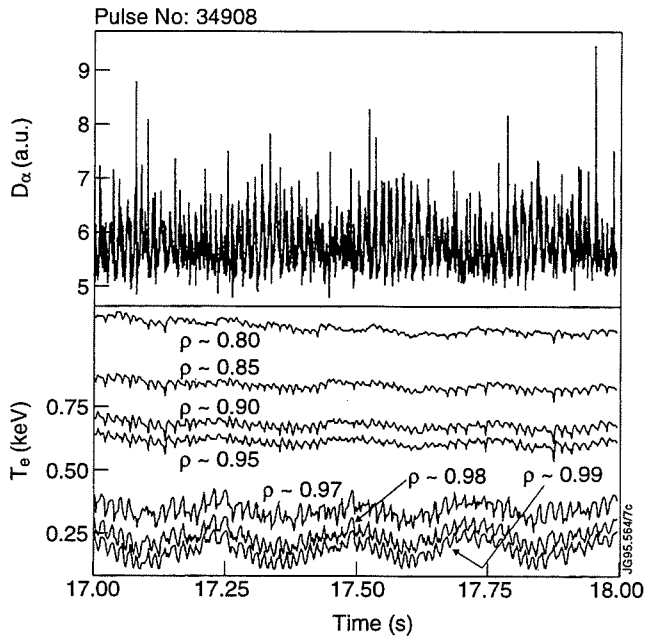

Figure 5 displays the evolution of T_e at several radii near the plasma edge and the evolution of the D_α light, again for shot 34908. There is very little effect on T_e. The volume averaged electron density has increased from $\approx 0.75 \times 10^{20} m^{-3}$, at the L- to H-mode transition, to $\approx 1.1 \times 10^{20} m^{-3}$. The 4Hz oscillations on the outermost channels are caused by divertor sweeping.

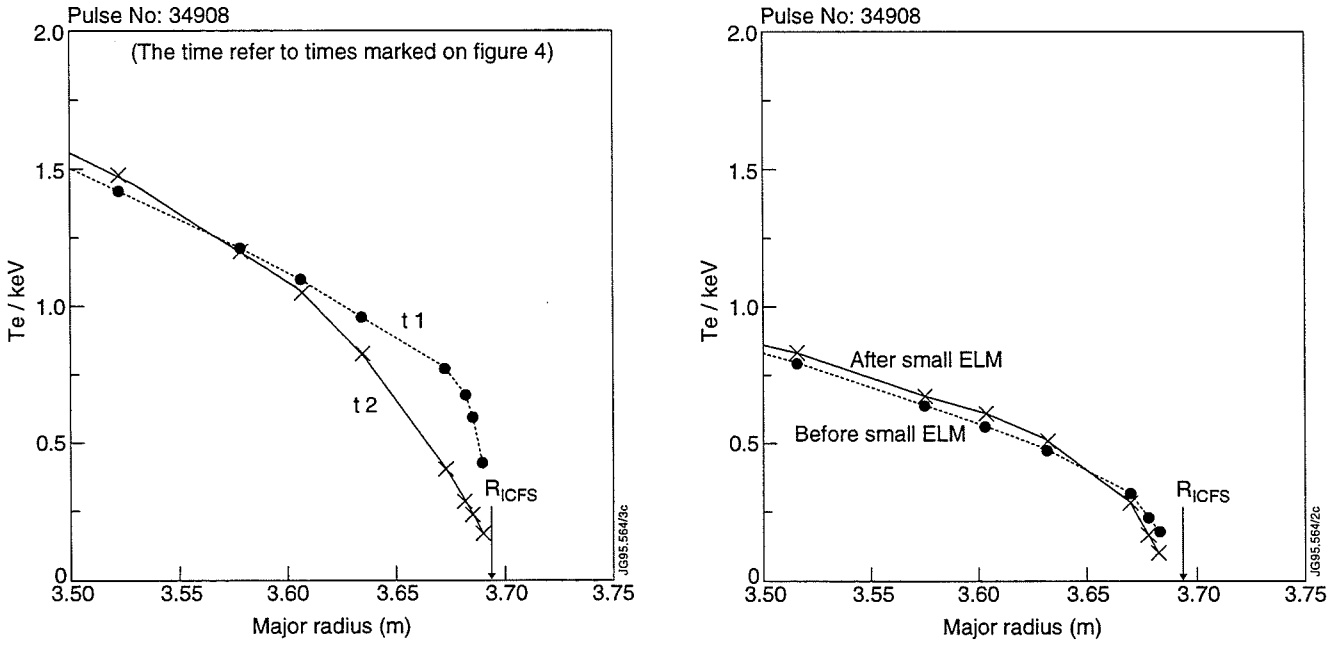

Figure 6 compares the T_e profiles before and after 2 types different ELM in the same pulse. Figure 6a displays the T_e profile before and after the medium ELM at t≈14.719 (see Figure 4). The ELM causes $\nabla T_e(\rho \geq 0.96)$ to fall from ≈53keVm^{-1} to ≈13keVm^{-1}. Figure 6b displays two T_e profiles before and after a small ELM (see figure 5). Small ELMs occur at ∇T_e≈15keVm^{-1} which and cause a very small change in edge T_e.

- Giant ELMs occur in Hot Ion H-modes when $\nabla T_e(\rho \geq 0.97)$ is large.
- Medium ELMs occur when the plasma exhibits high $\nabla T_e(\rho \geq 0.96)$.
- Small ELMs occur at high density and relatively low $\nabla T_e(\rho \geq 0.96)$.

EDGE MODES LEADING TO TERMINATION OF THE H-MODE

- A new type of phenomenon, called the 'slow roll over' has been identified [4] which limits the performance of JET H-modes on the relatively slow time scale of ≈20ms.
- The 'slow roll over' was first observed in the PTE series of experiments but was accompanied by a large impurity influx and it was impossible to distinguish cause from effect. The new JET configuration ensures that the target tiles remain sufficiently cool to prevent impurity influx.
- Recent measurements using the high resolution ECE radiometer and the O-mode reflectometer have made it clear that the degradation is driven by MHD activity.

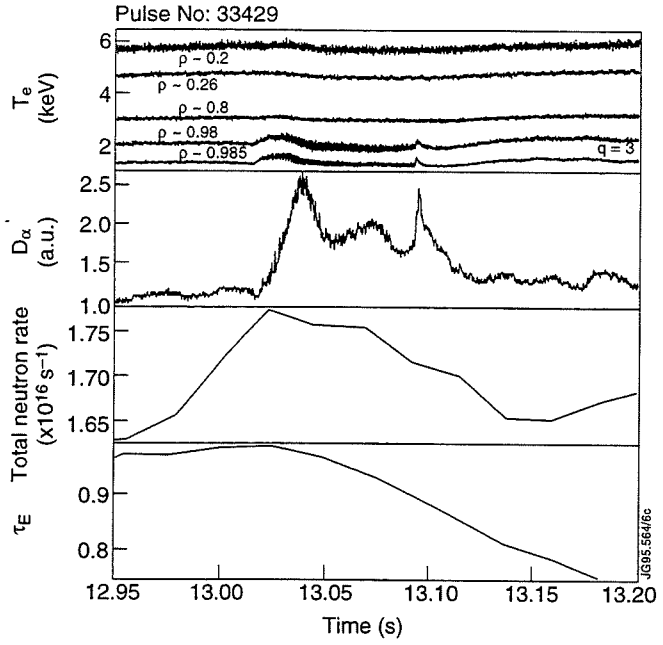

Figure 7 displays the temporal evolution of T_e at various radii, the D_α light, the total neutron emission rate and τ_E. A 10kHz mode begins to grow at t≈13.015s. At t≈13.02s the neutron rate and τ_E decline. The MHD mode localised to radii ρ≥0.98 causes a degradation of the bulk plasma parameters. The position of the q=3 surface is shown for reference.

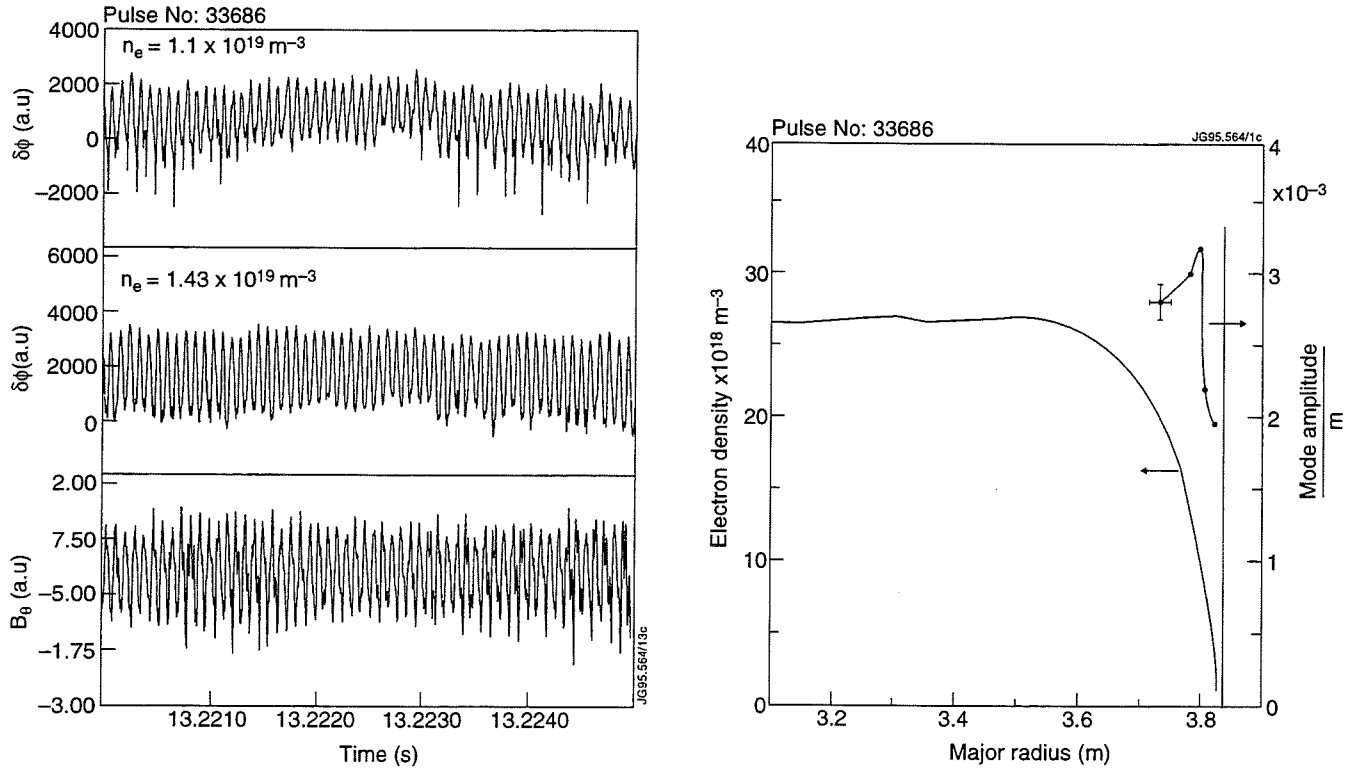

Figure 8 displays the oscillations in the density during the lifetime of the 'slow roll over' mode, the oscillations in B_θ, and shows, also, the mode amplitude as a function of major radius deduced from the oscillations in n_e.

Analysis of both the n_e and T_e fluctuations shows that the mode is localised to radii $\rho>0.97$ and that the mode causes a displacement of the plasma $\approx 0.003m \leq \delta R \leq \approx 0.01m$. Numerical simulation of these discharges [5] shows that external kink modes are marginally unstable with a dominant m=5 and smaller m=4 and m=3 components. This is in good agreement with SXR data [6] and is compatible with the ECE and density measurements.

PRESSURE GRADIENT AND BOOTSTRAP CURRENT

- In JET we measure $\nabla p_e \approx 10^6 Pam^{-1}$ in a region of the plasma $\approx 0.02m$ wide located at radii $\rho>0.97$. This will lead to bootstrap current density $\approx 1MAm^{-2}$ in JET [7].

- Such large current density may cause shear inversion which is not accounted for in equilibrium and stability calculations.

- Work is in progress to incorporate high resolution measurements in stability and equilibrium calculations.

CONCLUSIONS

- At the L- to H-mode transition Te and ne increase substantially and very large ∇T_e and ∇n_e are formed in a region of the plasma $\approx 2cm$ wide, approximately the size of the ion larmor width. This suggests the edge particle losses may be dominated by orbit losses.

- Giant ELMs are global in character and cause T_e, n_e, ∇T_e and ∇n_e to return to L-mode values.

- Medium ELMs affect the plasma to a depth $\rho \approx 0.5$ and cause the dynamic response of the plasma to sawteeth to change. They also cause ∇T_e to fall to values intermediate between L-mode and H-mode.

- Small ELMs affect the plasma at radii $\rho \geq 0.97$. Their effect on the edge T_e is very small.

- The performance of many JET H-mode discharges is limited by MHD modes localised to radii $r \geq 0.98$. Despite the localisation of these modes at the extreme plasma edge, the plasma performance is affected globally.

- ∇p_e is sufficiently large to expect modification of the q-profile and plasma stability. High resolution measurements, such as those presented here, must be incorporated in stability and equilibrium calculations.

REFERENCES

[1] L Porte et al ; 'First Results with the upgraded ECE heterodyne radiometer' Proc 18th EPS Conference on Controlled Fusion and Plasma Physics, 1992, **32**, pp.187-203

[2] ACC Sips ; `Reflectometry and Transport in Thermonuclear Plasmas in the Joint European Torus' ; PhD Thesis Technical University of Eindhoven 1991

[3] V V Parail et al ; 'Transport Analysis of Giant ELMs in JET' ; Proceedings 22nd EPS Conference on Controlled Fusion and Plasma Physics, July 1995

[4] P Smeulders et al ; 'Influence of MHD Instabilities on JET High Performance' ; ibid [3]

[5] G T A Huysmans et al ; 'Influence of Edge Currents and Pressure Gradients on the MHD Stability of Low-n External Kinks' ; ibid [3]

[6] R D Gill et al ; this conference

[7] C E Kessel ; 'Bootstrap Current in a Tokamak' ; Nuclear Fusion **34** No. 9 (1994) pp1221-1238

Plasma Performance on Solid and Molten Beryllium Divertor Targets in JET

B J D Tubbing and the JET Team.
JET Joint Undertaking, Abingdon, Oxfordshire, OX14 3EA, UK.

1. INTRODUCTION

In the final phase of the 1994/95 JET experimental campaign, the CFC divertor target was replaced by a Be target. Typical plasma facing dimensions of the target components were 30 x 80 mm. The Be surface is castellated with 6mm squares to relieve thermal stress. Most of the work on the Be target was carried out so that gross melting was avoided. Sweeping of the strike zones was used to reduce heatfluxes. This is the subject of **section 2** of the poster. In **section 3**, we discuss a specific experiment which was carried out to address the operation on Be at higher heatfluxes and with surface melting. In **section 4** the final state of the target is shown. In **section 5** the main conclusions and implications for ITER are discussed.

2. NORMAL OPERATION ON BE TARGETS AND COMPARISON WITH CFC TARGETS.

Most of the operation on the Be target was carried out so that gross melting was avoided.

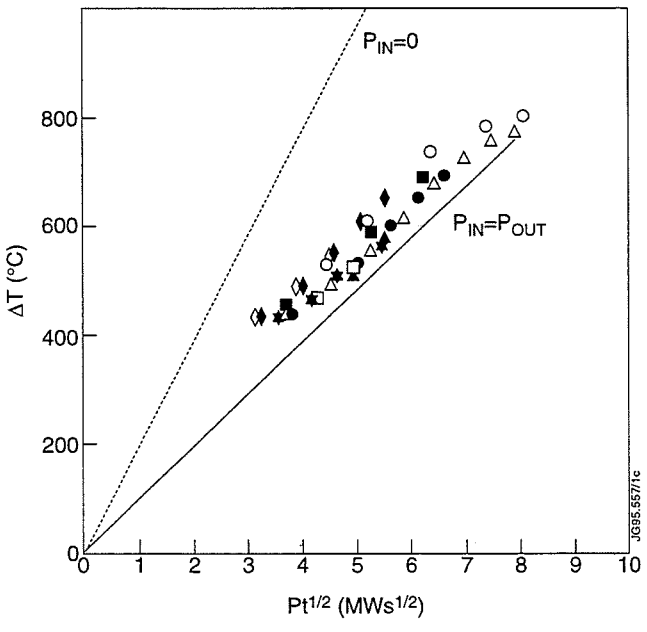

Surface temperature rise of the Be target versus expected temperature.

The basic power handling assessment was performed in L-mode discharges, without X-point sweeping, and with a SOL width of approximately 10mm.

The power handling of the Be target was as expected.

Observed temperatures agree with simple semi-infinite model predictions:
$T \propto (P_{tot} - P_{rad})^{0.5}$.

Slight melting of the Be target occurred in the assessment programme, at a $Pt^{0.5} = 11.3 MWs^{0.5}$.

Additional melt damage resulted from giant elms in high performance plasmas. No

disruption-induced melt damage has been observed.

Neither of these damages limited the subsequent operation.

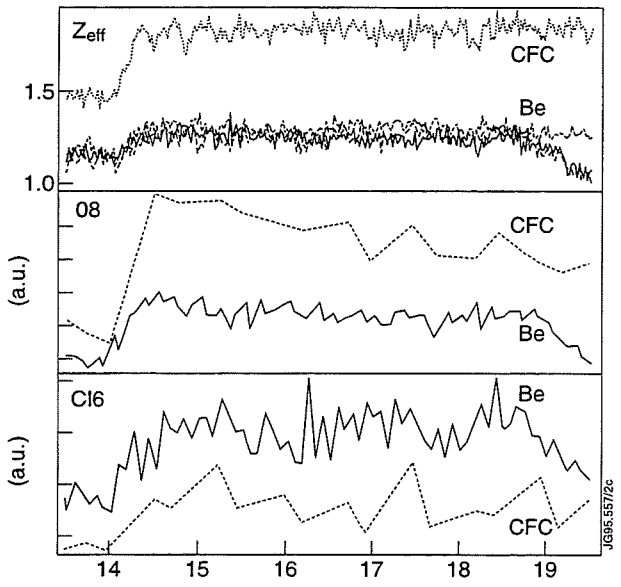

Z_{eff}, Oxygen 8 and Chlorine 6 line emission for plasmas on the Be and CFC targets.

The general behaviour of the tokamak with the Be divertor target was very similar to that with the CFC target, with the exception of some of the detailed impurity behaviour. This will be illustrated by various examples in the rest of this section.

In general, levels of Oxygen impurity are reduced on the Be target, while levels of Chlorine are increased.

There is no attributable source of the Chlorine.

Z_{eff} appears to be somewhat reduced. However, this is not substantiated by the D-D reaction rate measurements.

With the Be target, C line emission still dominates the total radiated power, particularly in medium to high density plasmas.

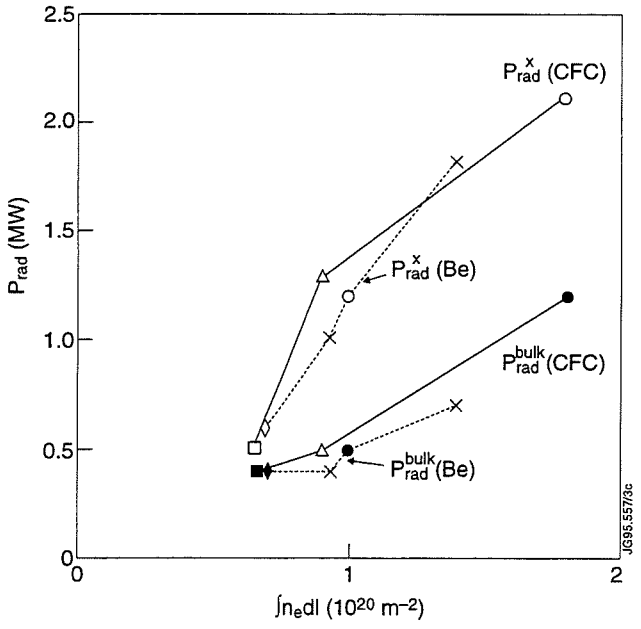

Increase of total and bulk plasma radiation as a function of density for Be and CFC targets.

A series of L-mode discharges with P_{NBI} = 5MW and varying density was performed.

The increase of total radiation and bulk plasma radiation with increasing density was the same for the CFC and Be targets.

The ratio of C_{III} to D_α emission from the divertor is reduced by an order of magnitude.

However, there is some evidence for the build up of Carbon deposits on the Be target.

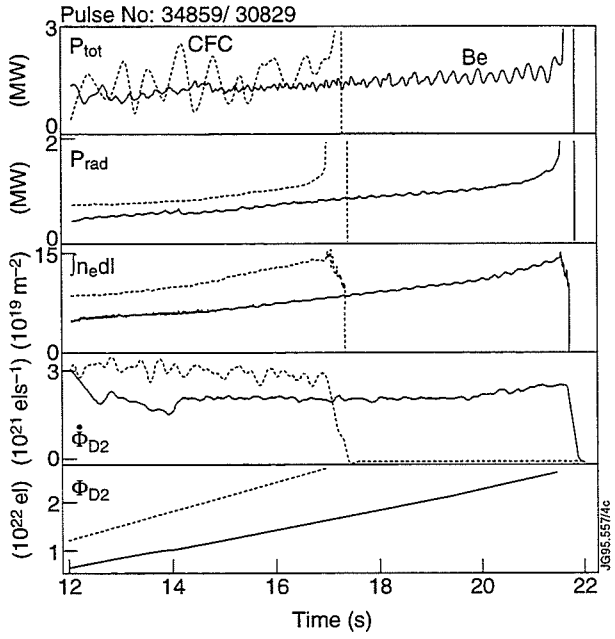

Comparison of ohmic density limit.

The density limit in ohmic and L-mode discharges is the same.

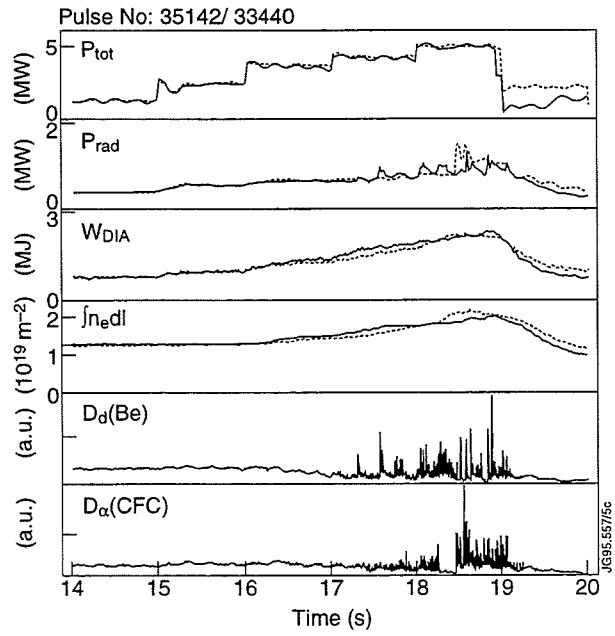

H-mode threshold comparison.

The H-mode threshold is the same for Be and CFC targets.

The H-mode threshold data obtained on Be is consistent with the threshold scaling found on CFC.

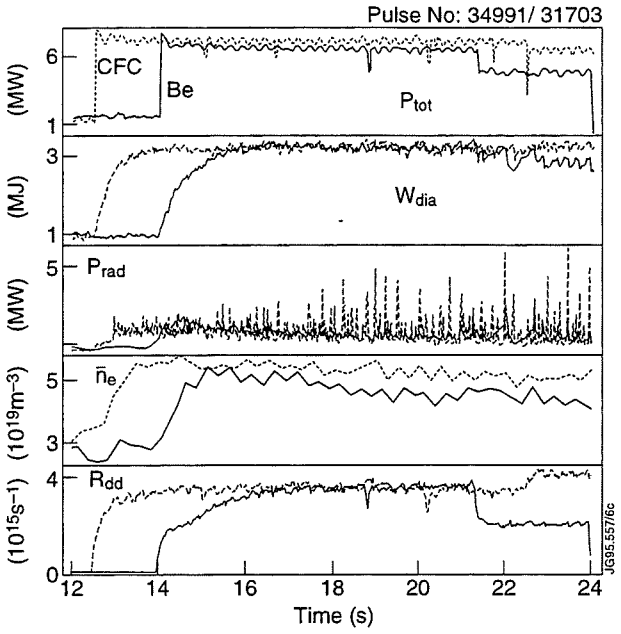

Comparison of steady-state H-modes.

Long pulse Elmy H-modes have almost identical characteristics.

Steady-state densities were found to be very similar.

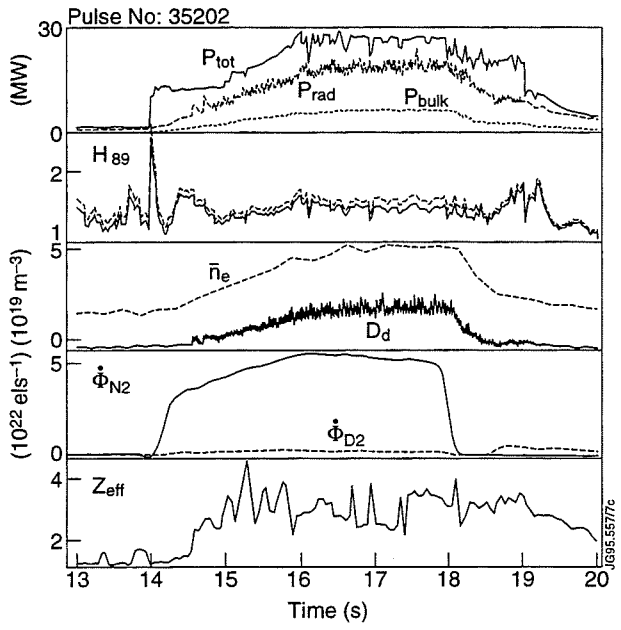

Radiative divertor with Nitrogen seeding on the Be target.

Radiative divertor operation with Nitrogen seeding has been re-established on the Be target, at power levels up to 30MW.

As in the CFC cases, an H-mode enhancement factor of about 1.5 over ITER-89 scaling is obtained.

However, contamination of the bulk plasma was severe, with Z_{eff} about 3 to 4.

3. THE BERYLLIUM MELTING EXPERIMENTS.

The **objectives** were:

1. to assess the operation on a Be target under conditions of surface melting.
2. to assess the operation on a cold, but surface-damaged, Be target.
3. to test the speculation that a Be target will 'self-protect' against excessive heatloads. Be evaporation would lead to radiative power loss and thus lower the heatflux.

The **configuration** for most of the experiment was: single-null X-point discharge at toroidal field 2.4T and plasma current 2.5MA. **Reference discharges** in the main operational regimes (ELMy H-mode with / without gas puff and Nitrogen-seeded radiative divertor) were taken before and after the melting. **Maximum heatflux to the target** was about 25MW/m^2 (derived from pre-melt temperature rise rates).

3.1 Initial melting in gas-puffed discharges

A series of discharges was run in which the heatflux to the target was gradually increased. The **gas puff rate** was 2.5 $10^{22}s^{-1}$ electrons.

The target was pre-heated by applying NBI power while sweeping the strike zones.

Then, sweeping was interrupted for a given duration to heat to the final temperature.

Be influxes are observed to increase with target temperatures above 1200°C.

The transition from 'evaporation from solid' to melting is not easy to distinguish.

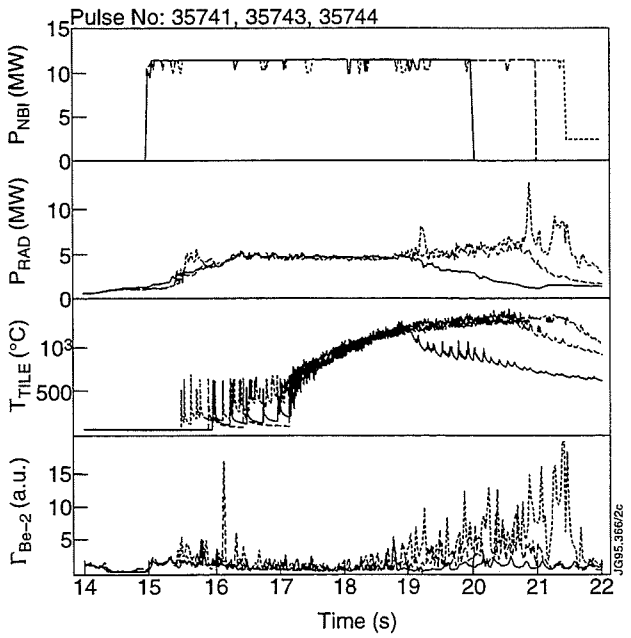

A series of discharges, in which the duration of the unswept heated phase is gradually increased. The final one leads to the first visible melting of the target. Target temperature drops when sweeping is resumed.

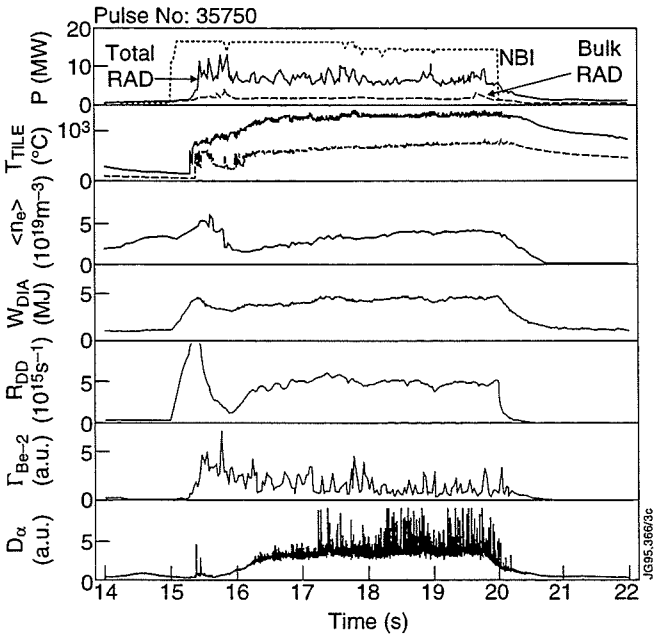

A discharge at high power, without sweeping and with gas puff.

The power and duration of the unswept phase were further increased, and significant melting of the target was observed with a CCD in-vessel viewing camera.

Nevertheless, the radiated power in the melting phases did not exceed about 50% of the input power.

ELMy H-mode operation was retained, and no degradation of confinement or D-D reaction rate with rising temperature was evident.

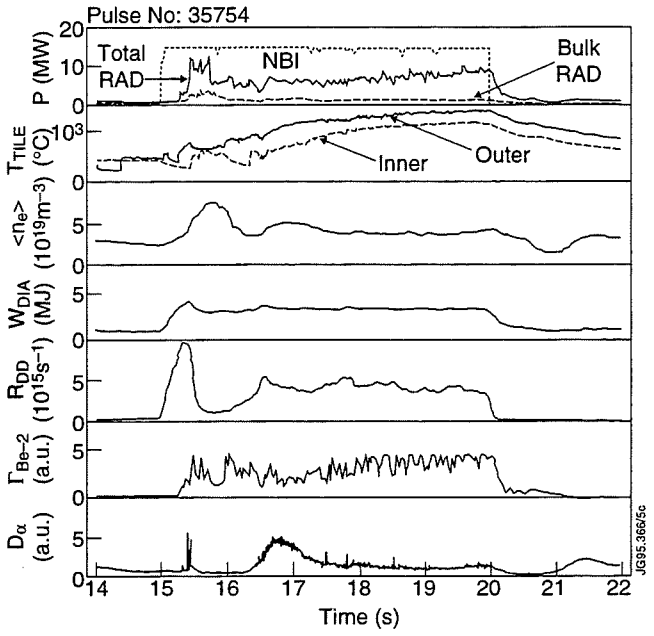

An unswept high power discharge without gas puff.

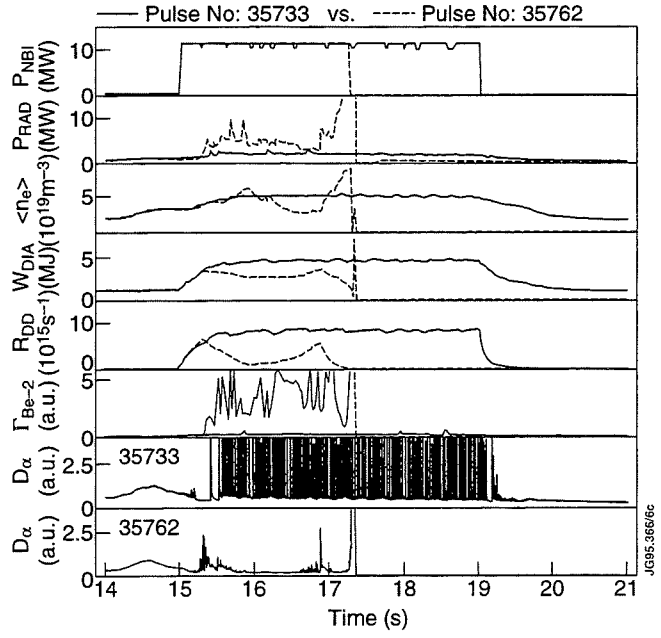

Comparison between two discharges without gas puff. The post melt discharge (dashed) is clearly degraded. H-mode is not obtained, and a disruption occurs due to Be influx.

3.2 Melting in discharges without gas puff.

A similar approach to melting was carried out in discharges without gas puff.

In these discharges high target temperatures and melting were observed also on the inner strike zone (in contrast to the gas puffed series).

The radiated power was observed to rise to about 70% ot the input power over a period of several seconds.

Further damage to the target was clearly visible.

The H-mode characted of these discharges was severely degraded.

This radiation increase is the only evidence of radiative 'self-protection' that was seen in these experiments.

3.3 Reference discharges, unswept.

Post-melt reference discharges are compared with the corresponding pre-melt ones:

1. ELMy H-mode with and without gas puff.
2. Nitrogen seeded radiative divertor plasma.

The pre-melt references are swept (to avoid melting). The post melt references are unswept, to localise the interaction on the damage.

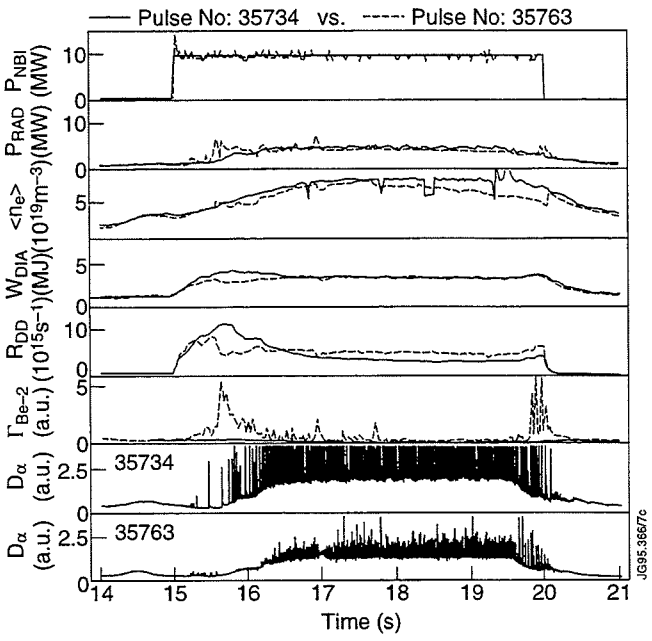

Comparison of two discharges with gas-puff (2.5$10^{22}s^{-1}$ electrons), before (solid) and after melting (dashed). After an initial transient, the overall characteristics are nearly identical.

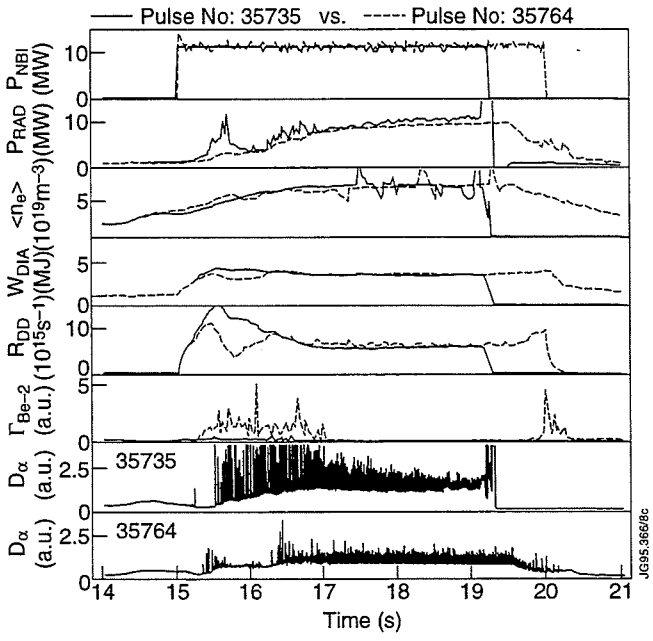

Two discharges with gas puff and Nitrogen seeding, in the radiative divertor regime, before (solid) and after (dashed) melting. After a transient phase, the overall characteristics are nearly identical.

3.4 Recovery of normal, swept operation.

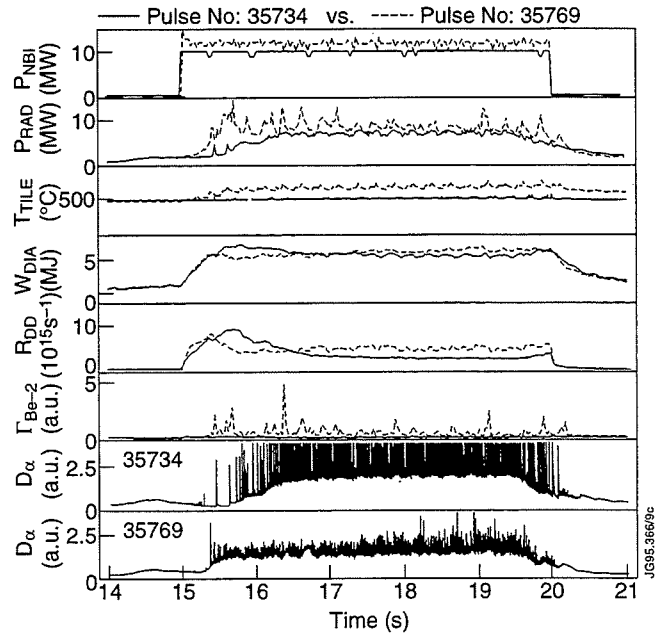

Comparison of a post-melt sweeping discharge (dashed) at gas puff rate of 2.5 10^{22} s^{-1} electrons, with a pre-melt discharge (solid). Signs of Be influx are evident, but the effect on performance is minor.

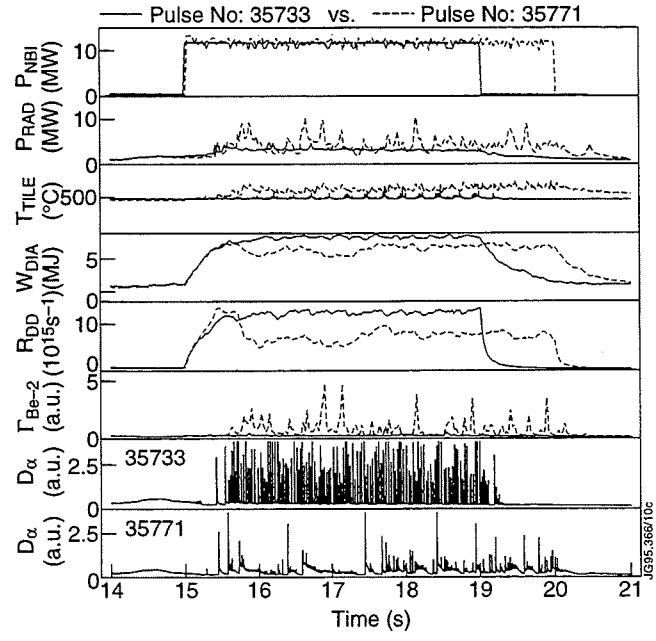

Comparison of a post melting discharge without gas puff (dashed) and a pre-melt reference (solid). ELMy H-mode operation is recovered, although the performance is still somewhat degraded.

The first discharge with X-point sweeping across the damaged zone, and no gas puff, disrupted due to a Be influx. Subsequent conditioning of the target was pbserved in a series of four discharges with progressively lower gas puff rates. A steady recovery towards normal operation was seen. The following figures show two discharges of this series.

3.5 High power swept operation on undamaged tiles.

The melt experiment was concluded with two discharges on a previously undamaged annulus of the target (toroidal field 2.8T, plasma current 3Ma). About 60mm sweeping was used. Total input energies were 120 and 180MJ respectively. 180MJ corresponds to about 100MJ m^{-2} on the target. Further damage to the tiles resulted from this operation. The total radiated power in these discharges did not exceed about 40%.

4. FINAL STATE OF THE TARGET

After the experiment, which ended the experimental campaign, there were four areas of damage. Two of these were already present prior to the melting experiment, namely the damage due to the giant ELMs, and due to the initial tile assessment.

One zone of damage is due to the melt experiments discused above. The final zone is due to the high power swept experiments (section 3.5).

The damage due to the melt experiment can be summarised as follows:

1. the damage zone is about 40mm wide.
2. the damage exhibits near perfect toroidal symmetry, showing the good quality of alignment.
3. bridges are formed across the gaps between tiles, up to about 10mm wide.
4. in the worst affected areas, erosion to a depth of about 3mm is observed.
5. there is relatively little collateral spreading of droplets.

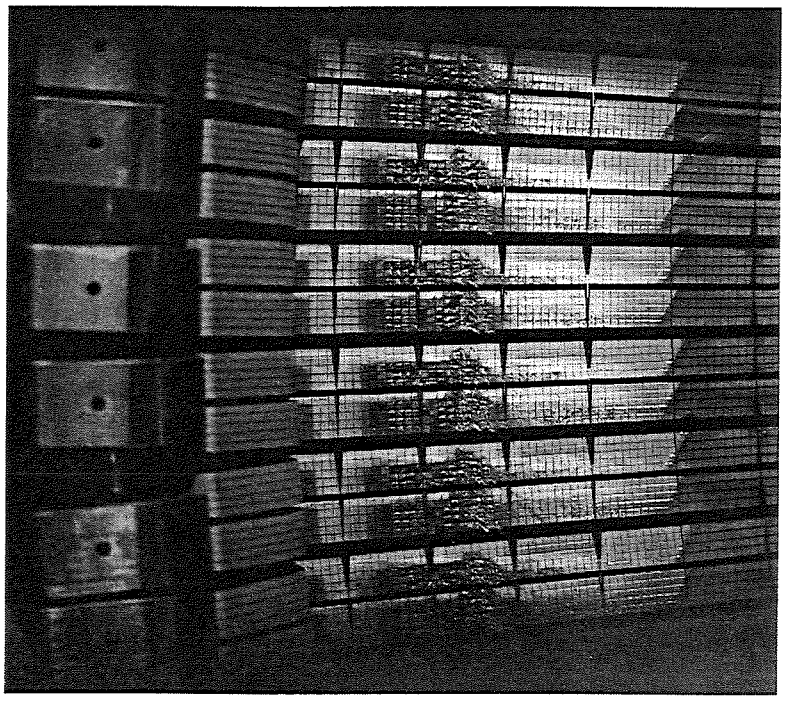

Photograph taken through vertical port after the experiment.

Photograph taken during the in-vessel survey showing the outer divertor target.

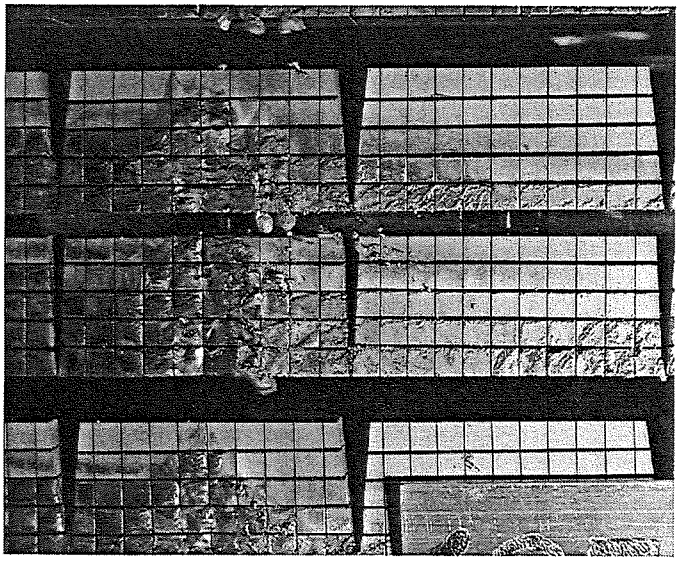

Close up of the damage.

There are clearly visible black deposits around the damage area. During the experiment, these were observed to be deposited and removed in subsequent discharges. Post mortem analysis shows that these deposits contain non-negligible amounts of carbon.

Sectioning of the tiles for microscopic inspection is in progress.

5. DISCUSSION AND IMPLICATIONS FOR ITER.

5.1 Normal operation.

The general behaviour of the plasma on a Be target was very similar to that on a CFC target. We note here that CFC protection on limiters and Inner-wall was common to both operational periods, and that Be evaporation was applied regularly in both phases. Hence, the comparison is not between 'pure' configurations.

The Carbon content of the plasma on the Be target was lower than that on CFC. However, the Carbon line radiation still exceeded the Be line radiation. Oxygen line radiation was reduced by about a factor two, but Chlorine radiation was increased by a comparable factor.

Steady-state H-modes in various conditions were found to have nearly identical characteristics. At the highest densities, plasmas returned to L-mode at about 50% of the input power radiated, well before divertor detachment occurred.

Radiative divertor operation with active impurity seeding (primarily Nitrogen) again were very similar to their counterparts on CFC.

For normal plasma operation, (in a machine with 'mixed' materials), no significant difference in behaviour was found between a CFC and a Be divertor target.

5.2 The Be melting experiment.

Heatfluxes of about 25MW/m^2 were applied to the Be divertor target, for a total duration of about 20s. The estimated heatflux is consistent with the observed tile temperature rise before the onset of melting. After melting, the interpretation of the target temperature is complicated because of emissivity changes of the material (as well as area changes and possible depositions).

The radiated power fraction in these experiments remained below 50%, except in the discharges without gas puff, where it increased to about 70% over a period of seconds. Most of the radiation is from the divertor.

The measured influxes of Be (BeII line emission) were lower by one to two orders of magnitude than those predicted from the Be evaporation rate at the melting temperature (10^{23} m^{-2} s^{-1}). This is not understood. There are two basic interpretations: either a force acts on the escaping Be neutrals to force them away from the plasma, or the evaporation / melting behaviour of the material in the divertor situation differs from the laboratory behaviour.

With heatfluxes of the order of 25Mwm^{-2}, applied for tens of seconds, severe damage was done to a Beryllium target, while only a moderate degree of 'self-protection' was evident.

Post-melt reference discharges showed that operation on the damaged Be with gas-puffing or Nitrogen impurity seeding is essentially the same as that on pristine tiles. Only discharges without gas puff were seriously degraded / disruptive. After some conditioning, normal Elmy H-mode operation, sweeping over the damaged zones, could be re-established.

This damage did not lead to an irrecoverable loss of plasma operation. However, it can be expected to lead to rapid component failure.

For ITER, it may thus be appropriate to design an active safety device for protection of the divertor against off-normal events, rather than to rely on the passive safety afforded by Beryllium radiative self-protection.

The behaviour under off-normal heatfluxes is but one element of the complex choice of a divertor target material for ITER.